

# Influence of hysteresis at magnetostructural transitions on the magnetocaloric properties of Heuslers, Antiperovskites, and Pnictides

Der Fakultät Physik  
der Universität Duisburg-Essen  
zur Erlangung des akademischen Grades  
eines Doktors der Naturwissenschaften (Dr. rer. nat.)

vorgelegte Dissertation von

**Franziska Scheibel**  
aus Neu-Ulm, Deutschland

Day of submission, Duisburg, 15.02.2018

Day of dissertation defense: 13.04.2018

1. Gutachter: Prof. Dr. Michael Farle
2. Gutachter: Prof. Dr. Oliver Gutfleisch



»What is a scientist after all?  
It is a curious man looking through a keyhole,  
the keyhole of nature, trying to know what's going on.«

**Jacques Yves Cousteau**





## Abstract

A large magnetocaloric effect can be observed in materials with first-order magnetostructural transition. Applying a magnetic field stabilizes the phase with higher magnetization and shifts the transition temperature to higher or lower temperatures. An adiabatically applied field induces a phase transformation and leads to an adiabatic temperature change. This temperature change is used in magnetocaloric refrigerators which is induced by applying a magnetic field cyclically. The material has to have a reversible adiabatic temperature change for each field-cycle to be an effective refrigeration material. The reversibility of the adiabatic temperature change depends on the hysteresis properties of the transition. A minimization of the thermal and magnetic hysteresis is important to improve the efficiency of magnetocaloric refrigerators.

The  $\text{Mn}_3\text{GaC}$  antiperovskite is a magnetocaloric material with a narrow hysteresis which shows a fully reversible first-order isostructural transformation at about 164 K from the antiferromagnetic state to the ferromagnetic state in an applied field of 2 T. The transformation is accompanied by a volume contraction of about 0.5%. The small hysteresis can be explained by the low magnetocrystalline-anisotropy-energy which was determined using a  $\text{Mn}_3\text{GaC}$  single crystal. The hysteresis properties of polycrystalline and single crystal  $\text{Mn}_3\text{GaC}$  are equivalent. However, in pulsed magnetic fields with fast field-sweep rates, the structural response of the transformation cannot follow the field change, which leads to a reduced magnetocaloric effect. This is in contrast to adiabatic magnetization measurements in pulsed fields showing a full transformation. The different time-responses of the structural and magnetic transition can be explained by the large volume change (0.5%) at the first-order transformation.

Mn-Cr-Co-Sb pnictide has a first-order isostructural transition from an antiferromagnetic state to a ferrimagnetic state and has, like  $\text{Mn}_3\text{GaC}$ , a narrow hysteresis. The transformation in Mn-Cr-Co-Sb can follow the fast field-sweep rates. This can be explained by the ten times smaller volume change during the transformation in Mn-Cr-Co-Sb compared to  $\text{Mn}_3\text{GaC}$ .

Another class of magnetocaloric materials are off-stoichiometric Ni-Mn-In Heusler alloys. However, these alloys are not stable and decompose into stoichiometric  $\text{Ni}_2\text{MnIn}$  and NiMn when annealed between 650 and 750 K. In Ni-Mn-In alloys with 5% In, annealing in a magnetic field leads to the formation of shell-ferromagnetic nanoprecipitates. The ferromagnetic hard-shell remains pinned up to fields of 5 T while the rest of the precipitate shows a soft ferromagnetic behavior. A selective formation of precipitates can be a further opportunity to tune the hysteresis in Ni-Mn-In Heusler alloys.

## Kurzfassung

Ein großer magnetokalorischer Effekt lässt sich in Materialien mit einem magnetostrukturellen Übergang erster Ordnung beobachten. Das Anlegen eines magnetischen Feldes führt zu einer Stabilisierung der magnetischen Phase, welche die größere Magnetisierung aufweist. Dies führt zu einer Verschiebung der Übergangstemperatur zu höheren oder niedrigeren Temperaturen. Das adiabatische Anlegen eines magnetischen Feldes führt zu einer Phasenumwandlung und zu einer adiabatischen Temperaturänderung. Diese Temperaturänderung wird für die magnetokalorische Kühlung verwendet und wird durch ein zyklisch angelegtes Magnetfeld induziert. Das verwendete Material ist nur dann ein effektives magnetokalorisches Material, wenn es eine reversible adiabatische Temperaturänderung für jeden Feldzyklus aufweist. Die Reversibilität der adiabatischen Temperaturänderung hängt dabei von den Eigenschaften der Hysterese des Übergangs ab. Eine Minimierung der thermischen und magnetischen Hysterese ist daher wichtig für die Optimierung der Effektivität der magnetokalorischen Kühlung.

Mn<sub>3</sub>GaC Antiperovskite sind magnetokalorische Legierungen mit einer schmalen Hysterese. Mn<sub>3</sub>GaC hat einen voll reversiblen isostrukturellen Übergang erster Ordnung bei etwa 164 K in einem angelegten Feld von 2 T. Dabei handelt es sich um einen Übergang von einer antiferromagnetischen zu einer ferromagnetischen Phase, welcher von einer Kontraktion des Volumens von etwa 0.5% begleitet wird. Die schmale Hysterese kann durch eine geringe magnetokristalline Anisotropie-Energie erklärt werden, welche mithilfe eines Mn<sub>3</sub>GaC Einkristalls bestimmt wurde. Die Eigenschaften der Hysterese sind für polykristalline und einkristalline Mn<sub>3</sub>GaC Proben äquivalent. In gepulsten Magnetfeldern ist die Feldänderung so schnell, dass die strukturelle Reaktion des Übergangs nicht folgen kann, was zu einer Verringerung des magnetokalorischen Effekts führt. Im Gegensatz dazu zeigen adiabatische Magnetisierungsmessungen in gepulsten Feldern einen vollständigen Übergang. Der Unterschied in der Reaktionszeit der strukturellen und magnetischen Umwandlung kann durch die große Volumenänderung des Phasenübergangs erster Ordnung erklärt werden.

Mn-Cr-Co-Sb Pniktide haben einen isostrukturellen Phasenübergang erster Ordnung von einer antiferromagnetischen in eine ferrimagnetischen Phase. Ähnlich wie Mn<sub>3</sub>GaC weist auch Mn-Cr-Co-Sb eine schmale Hysterese auf. Die Umwandlung in Mn-Cr-Co-Sb kann allerdings den schnellen Feldänderungsraten folgen. Dies lässt sich durch die zehnmal geringere Volumenänderung während des Phasenübergangs, im Vergleich zu Mn<sub>3</sub>GaC, erklären.

Eine weitere magnetokalorische Materialklasse sind nicht-stöchiometrische Ni-Mn-In Heusler Legierungen. Diese Legierungen sind jedoch instabil und entmischen bei einer Wärmebehandlung zwischen 650 und 750 K in eine stöchiometrische Ni<sub>2</sub>MnIn Phase und eine NiMn Phase. Ni-Mn-In Legierungen mit einem In-Anteil von 5% zeigen nach einer Wärmebehandlung in einem Magnetfeld die Entstehung von Nanometer großen Ausscheidungen mit sowohl hart wie auch weich ferromagnetischen Eigenschaften. Die

hartferromagnetische Schale ist dabei gepinnt bis zu einem externen magnetischen Feld von 5 T. Der Rest der ferromagnetischen Ausscheidung zeigt hingegen ein weichmagnetisches Verhalten. Eine gezielte Bildung solcher Ausscheidungen kann eine weitere Möglichkeit sein, um die Hysterese in Ni-Mn-In Heusler Legierungen zu variieren.

## Acronyms and Abbreviations

<b>AF</b>	antiferromagnet or antiferromagnetic
<b>bcc</b>	body center cubic
<b>CCD</b>	charge coupled device
<b>chap.</b>	chapter
<b>DOS</b>	density of states
<b>DSC</b>	differential scanning calorimetry
<b>EBS</b>	electron backscatter diffraction
<b>EDX</b>	energy dispersive X-ray spectroscopy
<b>EPM</b>	enhanced paramagnetic
<b>eq.</b>	equation
<b>ESR</b>	electron spin resonance
<b>FC</b>	field-cooled
<b>fig.</b>	figure
<b>FW</b>	field-warmed
<b>FI</b>	ferrimagnet or ferrimagnetic
<b>FM</b>	ferromagnet or ferromagnetic
<b>FMR</b>	ferromagnetic resonance
<b>HLD-EMFL</b>	Helmholtz-Zentrum Dresden-Rossendorf at the High Magnetic Field Laboratory in Dresden
<b>LLG</b>	Landau-Lifshitz-Gilbert
<b>MCAE</b>	magneto-crystalline anisotropy energy
<b>MCE</b>	magnetocaloric effect
<b>PM</b>	paramagnet or paramagnetic
<b>PPMS</b>	physical property measurement system

<b>RSO</b>	reciprocating sample option
<b>SAE</b>	shape anisotropy energy
<b>SE2</b>	secondary electron
<b>SEM</b>	scanning electron microscope
<b>SQUID</b>	superconducting quantum interference device
<b>XRD</b>	X-ray diffraction
<b>ZFC</b>	zero-field-cooled



## Symbols

$a$	lattice parameter
$\alpha$	damping-term
$\alpha_i$	direction cosine
$\mathbf{b}$	high-frequency magnetic field
$\mathbf{B}_{\text{eff}}$	effective magnetic field
$\mathbf{B}_{\text{ext}}$	external magnetic field
$\beta$	molecular field constant
$c$	lattice parameter
$c_c$	critical lattice parameter $c$
$C_p$	specific heat, heat capacity
$E_F$	Fermi energy
$F$	free energy density
$G$	Gibbs free energy
$g$	Landé $g$ -factor
$\gamma$	gyromagnetic ratio
$H$	magnetic force
$\hbar$	reduced Planck constant
$\underline{\underline{J}}_{b/m}$	Jacobian matrices
$\theta$	polar angle
$k_B$	Boltzmann constant
$K_4$	cubic anisotropy constant
$\lambda$	relaxation frequency
$\lambda_{K\alpha i}$	wavelength of copper radiation
$\mathbf{m}$	high-frequency magnetization
$\mathbf{M}$	magnetization
$\mathbf{M}_S$	saturation magnetization
$\mu_B$	Bohr magneton
$\mu_0$	permeability in vacuum
$\underline{\underline{N}}$	demagnetization-tensor
$p$	pressure
$\phi$	azimuth angle
$Q$	heat
$S$	entropy
$\Delta S$	entropy change
$t$	time
$T$	temperature
$\Delta T_{\text{ad}}$	adiabatic temperature change
$T_C$	Curie temperature
$\Delta T_{\text{hyst}}$	thermal hysteresis
$T_i$	transition temperature
$T_N$	Néel temperature
$U$	internal energy
$V$	volume
$\omega$	resonance frequency
$\chi$	susceptibility
$\underline{\underline{\chi}}$	high frequency susceptibility tensor

# Contents

<b>1</b>	<b>Introduction</b>	<b>1</b>
<b>2</b>	<b>Fundamentals</b>	<b>5</b>
2.1	Magnetocaloric effect and thermodynamics at first- and second-order transitions . . . . .	5
2.2	Magnetocaloric materials and magnetic transitions . . . . .	15
2.2.1	Transitions in Ni-Mn-based Heusler alloys . . . . .	15
2.2.2	Transitions in $\text{Mn}_3\text{GaC}$ antiperovskite . . . . .	21
2.2.3	$\text{Mn}_{2-y}\text{X}_y\text{Sb}$ pnictides (X:Ti, V, Cr, Fe) . . . . .	25
<b>3</b>	<b>Experimental methods</b>	<b>29</b>
3.1	Sample preparation . . . . .	29
3.2	Structure analysis . . . . .	31
3.2.1	Powder X-ray diffraction . . . . .	31
3.2.2	Electron microscopy . . . . .	31
3.3	Magnetic characterization . . . . .	33
3.3.1	Magnetometry . . . . .	33
3.3.2	Magnetic resonance . . . . .	35
3.4	Adiabatic magneto-calorimeter . . . . .	41
<b>4</b>	<b>Results and discussion</b>	<b>47</b>
4.1	Transition dynamics of $\text{Mn}_3\text{GaC}$ at different time-scales . . . . .	47
4.1.1	Isothermal and adiabatic magnetization . . . . .	48
4.1.2	$\Delta T_{\text{ad}}$ at slow field-sweep rate $11 \text{ mTs}^{-1}$ . . . . .	55
4.1.3	$\Delta T_{\text{ad}}$ at moderate field-sweep rate $700 \text{ mTs}^{-1}$ . . . . .	57
4.1.4	$\Delta T_{\text{ad}}$ at fast field-sweep rate $20 \text{ Ts}^{-1}$ . . . . .	60
4.1.5	$\Delta T_{\text{ad}}$ in pulsed fields up to $1 \text{ kTs}^{-1}$ . . . . .	62
4.1.6	Comparison of $\Delta T_{\text{ad}}$ at different field-sweep rates . . . . .	64
4.2	Characterization of $\text{Mn}_3\text{GaC}$ single crystal and comparison with polycrystalline sample . . . . .	67
4.2.1	Structural characterization . . . . .	67
4.2.2	Magnetic properties . . . . .	70



4.3	Transition dynamics of (Mn,Cr,Co)Sb pnictides probed at different time scales . . . . .	79
4.3.1	Isothermal magnetic transition with narrow hysteresis . . . . .	79
4.3.2	$\Delta T_{\text{ad}}$ at slow field-sweep rate $11 \text{ mTs}^{-1}$ . . . . .	82
4.3.3	$\Delta T_{\text{ad}}$ in pulsed field with up to $1 \text{ kTs}^{-1}$ field-sweep rate . . . . .	85
4.3.4	Comparison of $\Delta T_{\text{ad}}$ at different field-sweep rates . . . . .	89
4.4	Magnetic properties of ferromagnetic nano-precipitates in decomposed off-stoichiometric NiMnIn . . . . .	91
4.4.1	Field-dependent magnetization of nano-precipitates . . . . .	93
4.4.2	Magnetic resonance of nano-precipitates in the field-range up to $11.5 \text{ T}$ . . . . .	96
4.5	Conclusion . . . . .	101
	<b>Bibliography</b>	<b>107</b>
	<b>Acknowledgment</b>	<b>125</b>
	<b>List of Figures</b>	<b>127</b>
	<b>List of Publications</b>	<b>130</b>
	<b>Conference Contributions</b>	<b>132</b>
	<b>Curriculum Vitae</b>	<b>134</b>
	<b>Declaration of Authenticity</b>	<b>136</b>
	<b>List of Relevant Publications</b>	<b>137</b>



# 1 Introduction

Solid-state magnetic refrigeration is a topic which has been in focus since the last 30 years [Gut11, Gsc08]. Cooling technology based on the magnetocaloric effect (MCE) which is defined as the emission or absorption of heat when an applied magnetic field causes a substantial entropy change in a magnetocaloric material [RG13]. The effect was first observed by Weiss and Picard in 1917 in Ni [Wei17, Smi13] but was also mentioned in 1881 by Warburg [War81]. In 1933, Giauque and MacDougall used  $\text{Gd}_2(\text{SO}_4)_3$ -salt to achieve a temperature of 0.25 K by adiabatic demagnetization [Gia33]. This led to the award of the Nobel Prize in chemistry in 1949. The first magnetocaloric demonstrator was built by G. V. Brown in 1976 using Gd plates as a heat exchanger [Bro76] demonstrating the proof-of-concept for room-temperature magnetic refrigeration. In 1997, Pecharsky and Gschneidner [Pec97] observed a giant MCE in  $\text{Gd}_5(\text{Si}_2\text{Ge}_2)$  near room temperature. This was a milestone in developing and designing magnetocaloric materials and devices.

Magnetic refrigeration technology is based on the principle of a magnetic refrigeration-cycling [Teg02, Mn13, RG13]. The working-flow of a magnetocaloric cooling cycle is schematically shown in fig. 1.1. In the first step the magnetocaloric material is at the temperature  $T_1$  in state A and undergoes a magnetic field-induced adiabatic transformation from state A to state B. The change of magnetic entropy during the transformation leads to an adiabatic temperature change  $\Delta T_{\text{ad}}$ . An exchange liquid or gas transfers the heat from the material to the hot reservoir. After the heat transfer, the temperature is back at  $T_1$  and the material undergoes the reverse transformation from state B to state A by decreasing the magnetic field. The reverse adiabatic temperature change  $-\Delta T_{\text{ad}}$  is removed by a second heat transfer which leads to a temperature decrease of the cold reservoir and the refrigeration cycle resumes.

The value of  $\Delta T_{\text{ad}}$  correlates with the isothermal entropy change  $\Delta S$  of the field-induced transformation and becomes large in the vicinity of the first-order transition temperature so that the magnetocaloric refrigerator can only efficiently operate in a temperature range close to this temperature. A possibility to increase  $\Delta T_{\text{ad}}$  is to use magnetocaloric materials with first-order transition, since such a transition exhibits a larger  $\Delta S$  compared to materials with a second-order transition [RG13, Liu12a]. The disadvantage of materials with a first-order transition is the presence of transitional hysteresis leading to a reduced, reversible  $\Delta T_{\text{ad}}$  due to hysteresis losses [Tit12, Sko13, Chi16].

There are already prototype systems currently running to test the efficiency of the

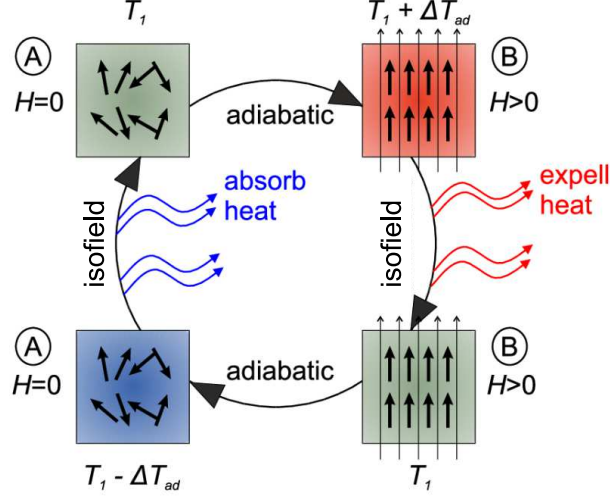


**Figure 1.1:** Schematic of a magnetocaloric cooling cycle. The material transforms adiabatically from state A to state B by increasing and decreasing an external magnetic field. Based on the MCE of the transformation, heat can be absorbed or expelled from the environment. The schematic is based on fig.1 in [Teg02] and [WWW13]

technique [Tag06, Yu10, Loz14, Sca15]. However, there are a number of challenges to be met to be able to make this technique compete with common gas-compression refrigeration [Kit10]. An effective magnetocaloric material has to undergo large  $\Delta T_{ad}$  in a magnetic field change of one to two Tesla. The limit of the field-value is given by the maximum value of commercially available permanent magnets which are used for the refrigeration. The permanent magnet is also the largest expense factor of the device [Bj016]. Additionally, the material should have a high thermal conductivity to enable efficient and fast refrigeration cycles. To minimize production costs, the material should contain no rare-earth or other expensive elements. The minimization of the thermal and magnetic hysteresis of the transition is also a key aspect for developing an efficient magnetocaloric material [Gut16, Tis14].

In recent years, a number of material families have been identified as potential candidates. Gadolinium and gadolinium alloys such as  $Gd_5(Ge, Si)_4$  exhibit large MCEs and are presently used in several prototype refrigerators [Pec97, Pec99, Tag06]. Because of the high costs of the constituent elements, a mass production for the market has not been possible. Another promising material is  $La(Fe, Si)_{13}$ , which has also a large MCE and contains only a small amount of the relatively cheaper rare-earth element La [Fuj02]. Furthermore, the composition of the alloy can be varied by substituting Fe with Co or Mn, or doping the alloy with hydrogen or carbon to vary the transition temperature over a broad range and to reduce hysteresis losses [Fuk06, Zha12, Liu12b, Kra14, Kae17].

---

Even better would be the use of materials containing no rare-earth elements such as Ni-Mn- $X$  ( $X$ :Ga, In, Sb, Sn) Heusler alloys [Kre05b, Pla07, Kre07b, Dub09], whereby the criticality of elements like Ga has to be considered. These alloys exhibit a large MCE, and the transition temperature can be tuned by varying the composition [Aks07, Kre07a, Sot08]. Due to the first-order magnetostructural transition, these alloys exhibit a thermal hysteresis [Tit12]. Therefore, understanding the origin of hysteresis is essential to reduce hysteresis losses [Gut16]. Another promising material class are Mn-based antiperovskites; a prototype being  $\text{Mn}_3\text{GaC}$  [Ç12]. The alloy exhibits a first-order isostructural transition from an antiferromagnetic (AF) to a ferromagnetic (FM) state below room temperature. The transition temperature can be tuned by replacing carbon partially by nitrogen so that such materials can be used for refrigeration applications at higher temperatures [Ç13]. The significant advantages of this class of materials is the narrow thermal hysteresis and the large significant  $\Delta T_{\text{ad}}$  of 5 K [Ç13].

Cr or Co doped  $\text{Mn}_2\text{Sb}$  pnictides are also suitable for magnetic refrigeration and exhibit a MCE close to room temperature with a narrow hysteresis [Tek17b]. The material transforms from an AF state to a ferrimagnetic (FI) state and carries no long-range ferromagnetic ordering [Swo60, Clo60, Kan84]. This property differs from other materials mentioned above having a first-order transition from an AF to a FM state.

This study focuses on the origin and the effects of transitional hysteresis, whereby, intrinsic and extrinsic origins are possible [Gut16]. A list is shown in fig. 1.2. The intrinsic origins include two subcategories; magnetism and the order of the transition. Magnetic properties such as the local magnetic moment, magnetic ordering, spin fluctuation, magnetic anisotropy or the building of domains can influence the width of the hysteresis just as the electronic structure. The study of these properties help to understand the origin of hysteresis. The width of the hysteresis depends on the order of the transition, whereby the coupling of lattice, magnetic and electronic entropies plays a crucial role. However, this coupling enables also multi external stimuli and can induce a caloric effect for example by a combination of magnetic and pressure fields [Mn10, Liu12a].

The time dependence and the microstructure are extrinsic origins of the hysteresis. The study of the transition dynamics under different magnetic field-sweep rates is important, since the time dependence of the MCE gives the limit of the operating frequency of the refrigeration cycle [Sch15, Got16c]. The width of the hysteresis is also influenced by the microstructure including, grain-size, coexisting phases, grain-boundary movements during phase transitions, the influence of interface-stress, various defects, phase impurities, or finite size effects.

Within the framework of this study, the transition dynamics and the limit of operating frequency for the different materials have been investigated with magnetization and  $\Delta T_{\text{ad}}$  measurements under different magnetic field-sweep rates. These have been undertaken for antiperovskites and pnictides. Magnetic, structural and magnetic anisotropy characterization of a  $\text{Mn}_3\text{GaC}$  single crystal were done and compared with

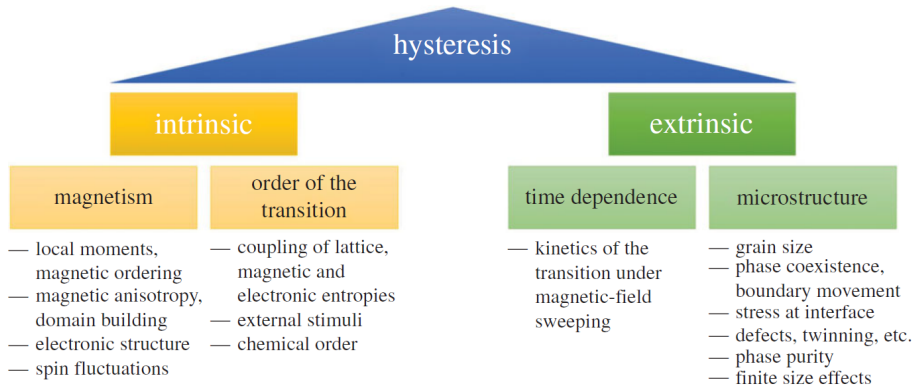


**Figure 1.2:** The origin of hysteresis can be divided into intrinsic and extrinsic origins. A detailed understanding of the hysteresis can help to master the hysteresis and to investigate materials with high reversible MCE [Gut16].

polycrystalline powder to study the effect of magnetic anisotropy and grain boundaries on the width of the hysteresis. The magnetic anisotropy is studied by ferromagnetic resonance (FMR). Furthermore, decomposition experiments of off-stoichiometric Heusler alloys are done to examine the effect of phase coexistence and the stress at the interfaces on hysteresis. These are also studied by FMR.

## 2 Fundamentals

This chapter gives an overview on the MCE and the fundamental concepts related to first- and second-order phase transitions and the effect of hysteresis at first-order transitions on the MCE. I further present three magnetocaloric material classes: Ni-Mn-based Heusler alloys,  $\text{Mn}_3\text{GaC}$  antiperovskite, and doped  $\text{Mn}_2\text{Sb}$  pnictides. I focus on magnetostructural transitions and the possibilities of tuning them.

### 2.1 Magnetocaloric effect and thermodynamics at first- and second-order transitions

This section describes the fundamentals of the MCE at first- and second-order magnetic phase transitions. An extensive description of the MCE can be found in reference [Tis03]. In addition, this section discusses the effect of the thermal hysteresis of first-order transitions on the MCE.

The MCE is defined as the emission or absorption of heat of a material when magnetized or demagnetized by an external magnetic field. The origin of the MCE lies in the change of the internal energy  $U$  due to a change in an external magnetic field.  $U$  of a system depends on its entropy  $S$ , volume  $V$ , and magnetization  $M$  or field  $H$  so that

$$U = U(S, V, H). \quad (2.1)$$

The total differential of  $U$  is,

$$\mathrm{d}U = T\mathrm{d}S - p\mathrm{d}V - M\mathrm{d}H, \quad (2.2)$$

where  $T$  is the temperature of the system, and  $p$  is the pressure. In magnetic systems at constant volume, the free energy  $F$  and its total differential are

$$F = U - TS \quad (2.3)$$

and

$$\mathrm{d}F = -S\mathrm{d}T - p\mathrm{d}V - M\mathrm{d}H. \quad (2.4)$$

The Gibbs free energy  $G$  and its total differential at constant pressure is given by

$$G = U - TS + pV - MH \quad (2.5)$$

and

$$dG = Vdp - SdT - MdH. \quad (2.6)$$

Under isobaric conditions, all terms containing  $dp$  vanish. Based on (2.4) and (2.6),  $S$  and  $M$  can be described by

$$S(T, H) = - \left( \frac{\partial G}{\partial T} \right)_H \quad (2.7)$$

and

$$M(T, H) = - \left( \frac{\partial G}{\partial H} \right)_T, \quad (2.8)$$

respectively. From equations (2.7) and (2.8), the Maxwell relation,

$$\left( \frac{\partial S}{\partial H} \right)_T = - \left( \frac{\partial M}{\partial T} \right)_H, \quad (2.9)$$

can be obtained. The total differential of  $S$  depends on  $T$ ,  $H$  and  $p$ . In the case of isobaric conditions,  $dS$  is

$$dS = \left( \frac{\partial S}{\partial T} \right)_H dT + \left( \frac{\partial S}{\partial H} \right)_T dH. \quad (2.10)$$

The isothermal ( $dT = 0$ ) entropy change  $\Delta S$  can then be calculated by integrating eq. (2.9) for a given magnetic field-range  $H_1 \leq H \leq H_2$  so that

$$\Delta S = \int_{H_1}^{H_2} \left( \frac{\partial M}{\partial T} \right)_H dH. \quad (2.11)$$

Varying the magnetic field under adiabatic conditions ( $dS = 0$ ) causes a temperature change  $\Delta T_{\text{ad}}$ , which can be calculated using the heat capacity  $C_p$  defined as

$$C_p = \left( \frac{\delta Q}{dT} \right)_p. \quad (2.12)$$

Here  $\delta Q$  is the added heat. From the second law of thermodynamics,  $dS = \delta Q/T$  so that the heat capacity can be rewritten as

$$C_p = T \left( \frac{\partial S}{\partial T} \right)_p. \quad (2.13)$$



## 2.1 Magnetocaloric effect and thermodynamics at first- and second-order transitions

The differential of the total temperature under adiabatic and isobaric conditions can then be obtained using (2.9), (2.10) and (2.13) as

$$dT_{\text{ad}} = -\frac{T}{C_{H,p}} \left( \frac{\partial M}{\partial T} \right)_H dH. \quad (2.14)$$

The finite value of  $\Delta T_{\text{ad}}$  can be calculated by the integrating (2.14) over the field-range  $H_1 \leq H \leq H_2$ , namely,

$$\Delta T_{\text{ad}} = - \int_{H_1}^{H_2} \frac{T}{C_{H,p}} \left( \frac{\partial M}{\partial T} \right)_H dH. \quad (2.15)$$

The entropy and temperature change  $\Delta S$  and  $\Delta T_{\text{ad}}$  are characteristic parameters of the MCE and are used for characterizing magnetic refrigeration materials. Both can be large when  $\partial M/\partial T$  is large as in the vicinity of a magnetic phase transition classified as first and second-order.

In the case of second-order magnetic transitions, the order parameter is the saturation magnetization  $M_S$ , and the transition is continuous. Fig. 2.1(a) shows schematically the temperature-dependent magnetization of a material which transforms from a FM to a paramagnetic (PM) phase at the Curie temperature  $T_C$ .  $M_S$  can be described by the Brillouin function [Sto06]

$$\frac{M(H, T)}{M_S} = \tanh \left( \frac{-\mu_B H}{k_B T} \right), \quad (2.16)$$

where  $\mu_B$  is the Bohr magneton and  $k_B$  is the Boltzmann constant.

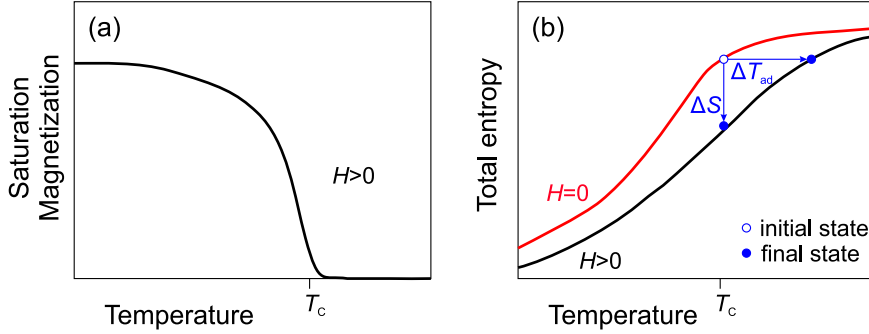


**Figure 2.1:** MCE at the second-order transition. (a) Schematic of the temperature-dependent magnetization in the vicinity of the second-order transition temperature  $T_C$  with external magnetic field. (b) Temperature dependence of the total entropy with (black) and without (red) external magnetic field. The isothermal and adiabatic processes are marked in blue.

Fig. 2.1(b) shows the temperature dependence of the total entropy for zero (red) and applied (black) magnetic field. The increase of the magnetic ordering due to an isothermally applied external field leads to a decrease in the entropy by  $\Delta S$ . An adiabatically applied field leads to a temperature increase by  $\Delta T_{\text{ad}}$ .

In the case of a first-order transition, a conventional or an inverse MCE can be observed. A material shows a conventional MCE when the increase of a magnetic field leads to an increase in the temperature. For an inverse MCE, the increase of a magnetic field leads to a decrease in the temperature.

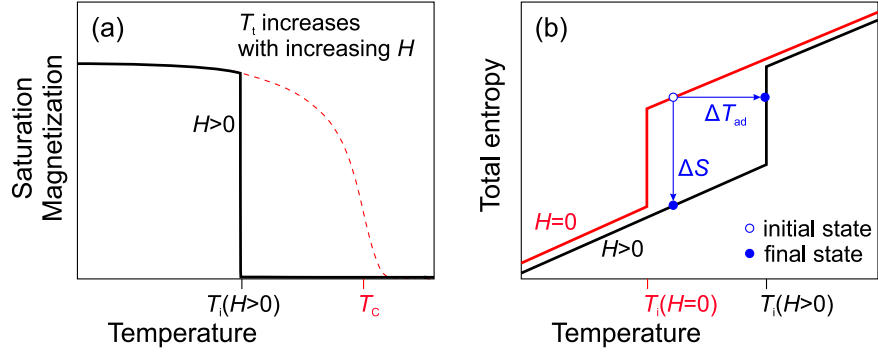


**Figure 2.2:** Schematic of the conventional MCE at the first-order transition. (a) Schematic of the temperature-dependent magnetization in the vicinity of the first- and second-order transition temperature  $T_i$  and  $T_C$  with an external magnetic field. (b) Temperature dependence of the total entropy in the region of  $T_i$  with (black) and without (red) external magnetic field. The isothermal and adiabatic processes are marked in blue.

Fig. 2.2(a) shows schematically the temperature dependence of the magnetization of a material undergoing a first-order magnetostructural transition with conventional MCE. In the low temperature-region, below the transition temperature  $T_i$ , the material behaves as a FM. However, at  $T_i$ , the magnetization drops discontinuously to a lower magnetization state due to the magnetostructural transformation. The presence of an external magnetic field furthers the stability of the low-temperature, high-magnetization state and shifts  $T_i$  to higher temperatures as the field increases. The first-order magnetostructural transition can take place not only from a magnetically ordered to a magnetically disordered state, as in a second-order transition, but also from one magnetically ordered state to another ordered state with a different magnetic configuration discontinuously. This causes a discontinuous entropy change at  $T_i$  (fig. 2.2(b)). Under applied field, the large shift of the transition temperature and the sharp drop of the entropy lead to a large MCE. In the case of first-order magnetostructural transitions  $\Delta T_{\text{ad}}$  can be estimated using the Clausius-Clapeyron equation

$$\frac{dH}{dT} = -\frac{\Delta S_M}{\Delta M}, \quad (2.17)$$

## 2.1 Magnetocaloric effect and thermodynamics at first- and second-order transitions

where  $\Delta S_M$  is the change in the entropy and  $\Delta M$  is the change in the magnetization when a field is applied. The temperature change  $\Delta T_{\text{ad}}$  can then be formulated by using eq. (2.17) and the relation  $\Delta T = -T\Delta S_M/C_H$  to give

$$\Delta T_{\text{ad}} = \frac{T}{C_H} \left( \frac{\partial H}{\partial T} \right) \Delta M. \quad (2.18)$$

The total entropy change can be described as the sum of the entropy changes of the magnetic,  $\Delta S_M$ , lattice  $\Delta S_{\text{lat}}$ , and electronic,  $\Delta S_{\text{el}}$ , subsystems, so that

$$\Delta S = \Delta S_M + \Delta S_{\text{lat}} + \Delta S_{\text{el}}. \quad (2.19)$$

All terms depend on  $H$  and  $T$ . Such a separation the subsystems is only possible when there is no phase transition. In this case, the adiabatically applied field results in a negative  $\Delta S_M$  and  $\Delta S_{\text{lat}}$  has to be positive since  $\Delta S_{\text{el}} = 0$ . A positive  $\Delta S_{\text{lat}}$  is related to an increase in the temperature so that  $\Delta T_{\text{ad}}$  is positive (see fig. 2.2(b)).

That the decoupling of entropies is not always possible becomes clear when materials showing the inverse MCE are taken into account. The inverse MCE describes the case of decreasing temperature when an external magnetic field is applied in contrast to materials showing the conventional MCE experiencing an increase in the temperature.

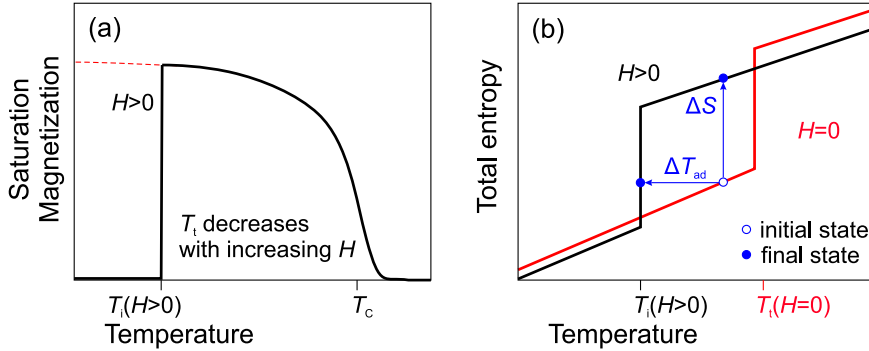


**Figure 2.3:** Schematic of the inverse MCE at the first-order transition. (a) Schematic of the temperature-dependent magnetization in the vicinity of the first- and second-order transition temperature  $T_i$  and  $T_C$  with an external magnetic field. (b) Temperature dependence of the total entropy in the vicinity of  $T_i$  with (black) and without (red) external magnetic field. The isothermal and adiabatic processes are marked in blue.

The  $M(T)$ -curve of an inverse MCE material is shown in fig. 2.3(a). Here, the high-magnetization phase is stable for  $T > T_i$ , and the low-magnetization phase for  $T < T_i$ . An external field stabilizes the high-magnetization phase causing a shift in  $T_i$  to lower temperatures. The entropy-curves for  $H = 0$  (red) and  $H > 0$  (black) are shown in fig. 2.3(b). The increasing field leads to an inverse MCE shown as an increase in  $\Delta S$

and a decrease in  $\Delta T_{\text{ad}}$ . Above  $T_i$ , the entropy in zero field is higher than the entropy with field leading to a conventional MCE for  $T > T_i$ . For the inverse MCE,  $\Delta S_M$  and  $\Delta S_{\text{lat}}$  are both negative. This makes it impossible to describe such a system by independent subsystems as in eq. (2.19). Therefore, in materials with inverse MCE, a significant change of the electronic structure must occur [Ç12, Got16b, Wol16]. A strong cooperative contribution of  $\Delta S_M$ ,  $\Delta S_{\text{lat}}$  and  $\Delta S_{\text{el}}$  to  $\Delta S$  is given in reference [Gru15]. The study shows a change of vibrational density of states at the first-order transition of  $\text{LaFe}_{13-x}\text{Si}_x$  related to magnetic disorder indicating an interconnection of magnetic, electronic and vibrational degrees of freedom.

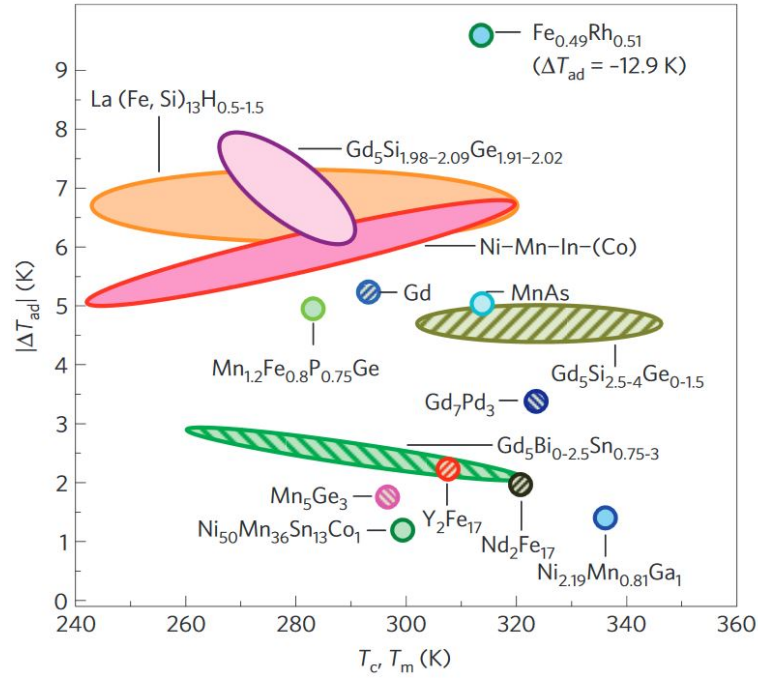


**Figure 2.4:** Overview of the adiabatic temperature change  $|\Delta T_{\text{ad}}|$  (in an external field of 2 T) of potential materials for magnetocaloric refrigeration. Materials which undergo a first-order transitions are denoted by filled ellipses and materials which undergo a second-order transition are marked with striped filling. [Liu12a]

For the performance of a magnetocaloric refrigerator, materials with conventional or inverse MCEs can be used.  $|\Delta S|$  and  $|\Delta T_{\text{ad}}|$  can be compared for potential magnetocaloric materials. Fig. 2.4 gives an overview of  $|\Delta T_{\text{ad}}|$  of different materials which can be interesting for magnetocaloric applications near room temperature. Materials exhibiting a first-order transition are denoted by filled areas, and materials with second-order transition are marked with striped areas. This figure shows that the use

of materials with a first-order transition can improve the performance of magnetic cooling devices due to their larger  $\Delta T_{\text{ad}}$ .

Gadolinium is known as a magnetocaloric material (see fig. 2.4) showing a FM/PM second-order phase transition at  $T_C = 292$  K. Differential scanning calorimetry (DSC) measurements on Gd show, however, an anomaly of the specific heat in the vicinity of  $T_C$  [Gri54] at which a strong spontaneous magnetostriction also occurs [Bir60]. The latent heat (transitional enthalpy) is required for the spontaneous magnetization, whereas the second-order transitional enthalpy is spread over the range from lowest temperatures to  $T_C$ . Thermal expansion measurements show further a volume change at  $T_C$  [Bir60]. Similar behavior in the specific heat and spontaneous magnetostriction at  $T_C$  can also be observed in  $\alpha$ -Fe [Pep01]. From an experimental point of view, this raises the question whether the magnetic transition in these materials can be described by a classical second-order transition (no volume change); at least at the transition temperature  $T_C$ .

To compare  $\Delta T_{\text{ad}}$  of materials with a first-order transition, the hysteresis of the transition has to be taken into account.  $\Delta T_{\text{ad}}$  in fig. 2.4 considers only  $\Delta T_{\text{ad}}$  for the first application of the external field and does not take into account the effect of hysteresis losses on cycling the field affecting the reversibility of  $\Delta T_{\text{ad}}$ . The hysteresis of the first-order transition is related to the presence of energy-barriers which have to be overcome for the nucleation of the new phase. The volume-difference of the two phases and the distortion energy at the phase boundary determines the energy-barrier landscape [Mey73]. The width of the hysteresis is governed by the driving force of the transformation which is the difference of the Gibbs free energy  $\Delta G = G_A - G_B$  in the super-cooled or super-heated state (A and B) [Hor92].  $G$  includes parameters such as the crystal structure, chemical order and elastic and inelastic distortion.

Fig. 2.5(a) shows schematically the temperature dependence of the Gibbs free energies of the two magnetic phases  $G_A$  (red) and  $G_B$  (black) in the vicinity of a first-order transition with equilibrium transition temperature  $T_0$ . Fig. 2.5(b) shows the temperature dependence of the magnetization. Phase A is thermodynamically stable for  $T \leq T_0$  while B is stable for  $T \geq T_0$ . At  $T_0$   $G_A = G_B$ . However, the transformation from A to B does not start at  $T_0$  but at a higher temperature  $T_{B1}$ . The super-heating corresponding to a temperature difference  $T_{B1} - T_0$  which is required to overcome the nucleation energy.

The transformation from the low-magnetization phase A to the high-magnetization phase B leads to an increase of the magnetization  $M(T)$  with increasing amount of phase B. (fig. 2.5(b)). The transformation is complete at  $T_{B2}$  and no further increase of the magnetization can be observed. The finite slope of the hysteresis is related to the elastic distortion energy. The reverse transformation from phase B to A also requires nucleation energy which leads in this case to super-cooling  $T_{A1} - T_0$ . The transformation finishes at  $T_{A2}$ . The temperature difference between the forward and reverse transformation branches is defined as the thermal hysteresis  $\Delta T_{\text{hyst}}$ . Depending on the material,  $\Delta T_{\text{hyst}}$

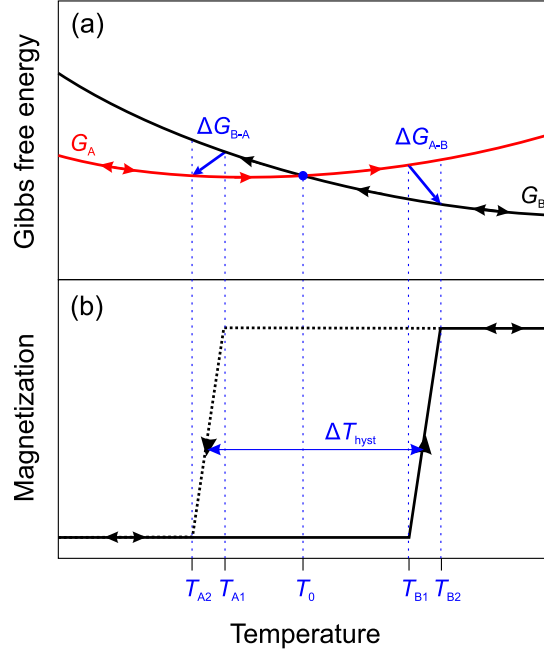


**Figure 2.5:** Schematic of the temperature-dependent Gibbs free energy (a) and magnetization (b) in the vicinity of a first-order phase transition  $T_0$ .

can range from a few Kelvin [Ç12, Tit12] up to several 100 Ks [Hor92].

The performance of a reversible transformation cycle requires, therefore, an external magnetic-field which is able to overcome the hysteresis. A fully reversible transformation cycle leads to a fully reversible  $\Delta T_{\text{ad}}$ . In case of a partial transformation, the reversibility of  $\Delta T_{\text{ad}}$  is reduced [Tit12, Sko13, Chi16].

A large and reversible  $\Delta T_{\text{ad}}$  in oscillating magnetic fields is an essential requirement for a refrigerant-material. Fig. 2.6 shows schematically the transition cycles of the total entropy of an inverse magnetocaloric material as a function of temperature. The material transforms from a low temperature low-magnetization state (B) to a high temperature high-magnetization state (A). The hysteresis is equivalent to the gap between the forward (dashed line) and the reverse (solid line) transformation paths. The red curve shows  $S(T)$  before and the black curve shows  $S(T)$  after the field change. The initial state is shown with open circles and the final state is shown with filled circles. Fig. 2.6(a) shows the transition when a field  $H_1$  is applied adiabatically ( $S_0$  is constant). The initial state in zero field lies along the reverse transformation path. When  $H_1$  is applied, the material follows the reverse transformation path from B to A and the transformation ends at the final state. Due to adiabatic conditions, the increase of the field (from zero to  $H_1$ ) leads to a decrease of the temperature from  $T_1$  to  $T_2$ . When the field is turned off, the hysteresis has to be overcome before the material

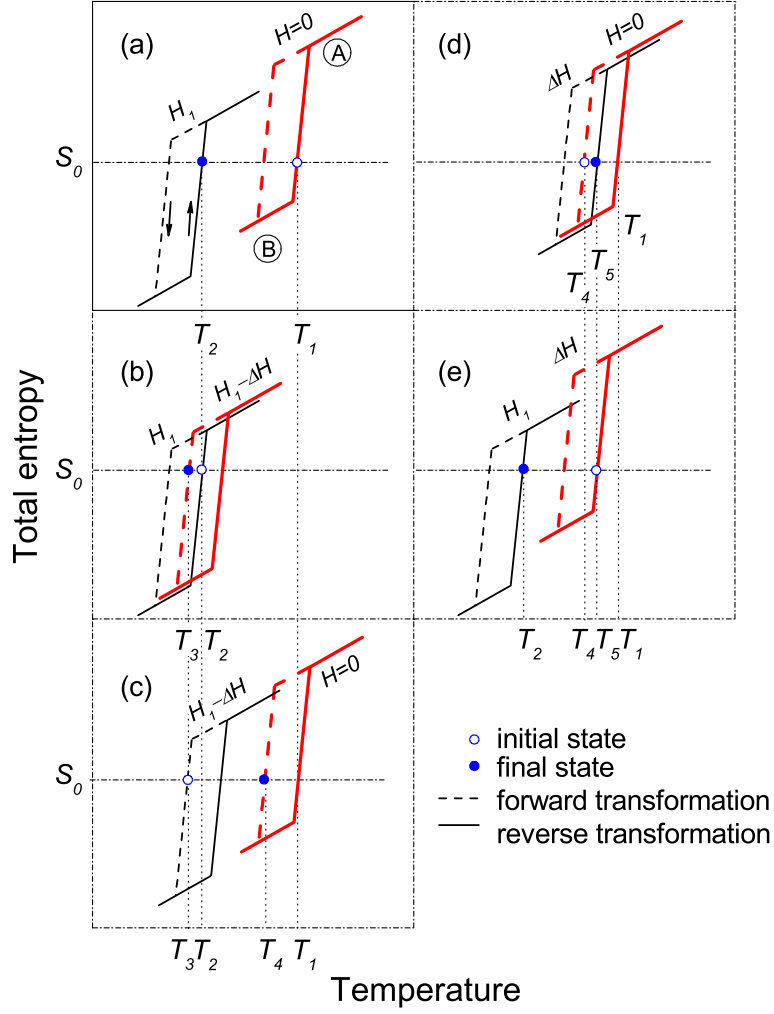


**Figure 2.6:** Schematic sequence of the temperature change of a material with inverse MCE. Sequence (a)-(e) show the temperature dependence of the total entropy for a cycled magnetic field. A detailed description of the sequence is given in the text. [Sch15]

can transform back to phase B. Fig. 2.6(b) shows that the hysteresis is overcome after the field is decreased by  $\Delta H$  reaching the forward transformation path. During the field change of  $\Delta H$ , the temperature of the sample increases from  $T_2$  to  $T_3$  due to the conventional MCE since the state of the system now does not change. The phase-fraction A/B remains constant during this process. The further decrease of the field (fig. 2.6(c), red curve) leads to a reverse transformation from A to B and to a decrease in  $T$  from  $T_3$  to  $T_4$ , related to the inverse MCE. This is now possible since the state of the material can change along the forward transformation path. The magnetic field can now be applied again, but it has to be considered that the initial state (fig. 2.6(d)) of the material is now different from that of the virgin state (fig. 2.6(a)). In fig. 2.6(d), the initial state lies on the forward transformation path, and the hysteresis has to be overcome again by increasing the field by  $\Delta H$  to start again the phase transition. On applying  $\Delta H$ , the temperature increases from  $T_4$  to  $T_5$  due to the conventional MCE, since the phase-fraction is again constant. A further increase of  $H$  leads then to the transformation and to a drop of  $T$  to  $T_2$  (see fig. 2.6(e)). Due to hysteresis, the initial temperature change  $\Delta T = T_1 - T_3$  is larger than the reversible change  $\Delta T = T_5 - T_3$ . Narrowing the hysteresis reduces  $T_2 - T_3$  and  $T_5 - T_4$ , and therefore, increases the reversible temperature change. Since a magnetocaloric refrigerator operates with an oscillating magnetic field, the effect of hysteresis plays an important role on the efficiency of the device.



## 2.2 Magnetocaloric materials and magnetic transitions

Many materials are candidates for magnetocaloric cooling [Liu12a, Fae12]. However, these should not contain harmful elements or expensive rare-earths. In this thesis three material classes are investigated: Ni-Mn-based Heusler alloys, antiperovskites and pnictides, all undergoing first-order transitions with a narrow transitional hysteresis of less than 15 K. This section gives an overview on the structural and magnetic properties and possibilities to tune the MCE and transition of such materials.

### 2.2.1 Transitions in Ni-Mn-based Heusler alloys

Ni-Mn-X Heusler alloys with main group elements X as Ga, In, Sn and Sb are interesting as magnetic refrigeration materials due to the presence of a first-order magnetostructural transition [Pla09, Sut04, Liu12a]. The alloys transform from a low-temperature martensitic phase with low magnetization to a high-temperature austenitic phase with larger magnetization [Ace11, Kre05a, Kre06a, Moy06]. The transformation can be induced by applying a magnetic field, causing a large change in the magnetization and leading to a large MCE [Kre05b, Kre07b, Liu12a]. Due to the magnetostructural transition, the transformation can also be induced by applying elastic, or pressure fields [Mn10]. I present in this section an overview on Ni-Mn-X Heusler alloys and discuss how MCEs can be improved. I also review the decomposition in off-stoichiometric Heusler alloys and its consequences on the MCE.

2-1-1 stoichiometric  $\text{Ni}_2\text{MnX}$  full Heusler alloys have an  $L2_1$  structure in the austenite state conforming with a  $Fm\bar{3}m$  space group [Web69]. The crystal structure is schematically shown in fig. 2.7(a). The Mn and X atoms are located in the center of a body centered cubic (bcc) cell with Ni atoms located at the corners. The  $L2_1$  structure builds a regular array of alternating bcc cells of Ni-Mn and Ni-X. In the case of chemical disorder among the Mn and X atoms, the structure becomes  $B2$  as shown in fig. 2.7(b). The acquired structure at room temperature depends on the thermal treatment during preparation. The  $L2_1$ - $B2$  order-disorder transition is located in the range  $900 \leq T \leq 1080$  K depending on the chemical composition [Ove99, Xu16]

With decreasing temperature, off-stoichiometric Ni-Mn-X compounds (as well as stoichiometric in the case of X as Ga) undergo a martensitic transformation. The martensite state can be tetragonal  $L1_0$  or modulated  $5M$  ( $10M$ ),  $7M$  ( $14M$ ) or  $4O$  [Ace11, Lar11, Kau11, Ç14a]. The transition is diffusionless but in most cases involves a volume change, which can be large as in Ni-Mn-Sn or nearly vanishing as in Ni-Mn-Ga. In both cases, different martensite variants are formed to reduce the elastic energy generated by the lattice mismatch at the martensite and austenite phase boundary (habit plane) [Kau11, Fae12, Nie12]. The transition from austenite to martensite starts with the formation of internally twinned martensite nuclei having a

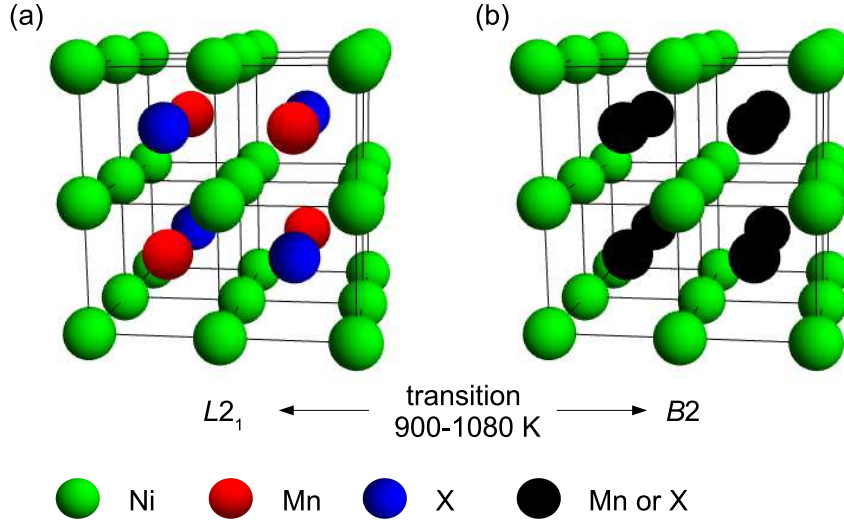


**Figure 2.7:** (a)  $L2_1$  structure of stoichiometric  $Ni_2Mn_1X_1$  full Heusler alloys. (b) Chemical disordered  $B2$  structure of the Heusler alloy where Mn and X are randomly distributed in their sublattices.

diamond-like shape [Nie17]. The energy for the formation of twin boundaries in the diamond-shape nuclei is lower than the elastic energy for the formation of a single martensite variant. The transformation progresses by the growth of two martensite variants of the diamond-shaped nuclei leading to the complex hierarchical morphology in the martensitic state.

The magnetic moment is in most Mn-based  $L2_1$  Heusler alloys related to the Mn atoms having a moment of about  $4\mu_B$  [Web67, Web69]. The exchange coupling of neighboring Mn atoms depend on their inter-atomic distance [Pep01]. In the case of elementary Mn, the coupling is AF. However, in Ni-Mn-X alloys, the Mn inter-atomic distance is larger than in elementary Mn leading to a FM exchange coupling [Sut04, Kre05a, Kre06b, Aks07]. The following parameter have influence on the interatomic distance in Ni-Mn-X and leading therefore to a change in the magnetic behavior: chemical ordering [Ito08], Mn-concentration, pressure, and temperature. The magnetization can drastically change at the martensitic to austenitic transformation temperature. The martensitic transformation temperature  $M_S$  depends linearly on the number of valence electrons in Ni-Mn-X [Kre07c].

Fig. 2.8 shows the magnetic and structural phase diagram of (a) Ni-Mn-Sn, (b) Ni-Mn-In and (c) Ni-Mn-Ga as a function of the valence electron concentration,  $e/a$ , calculated as the average of the  $s$  and  $d$ , and  $s$  and  $p$  valence electrons of the different elements weighted to the concentration [Pla09]. The regions with different structure are separated by dashed lines, whereby the cubic structure relates to the  $L2_1$  and

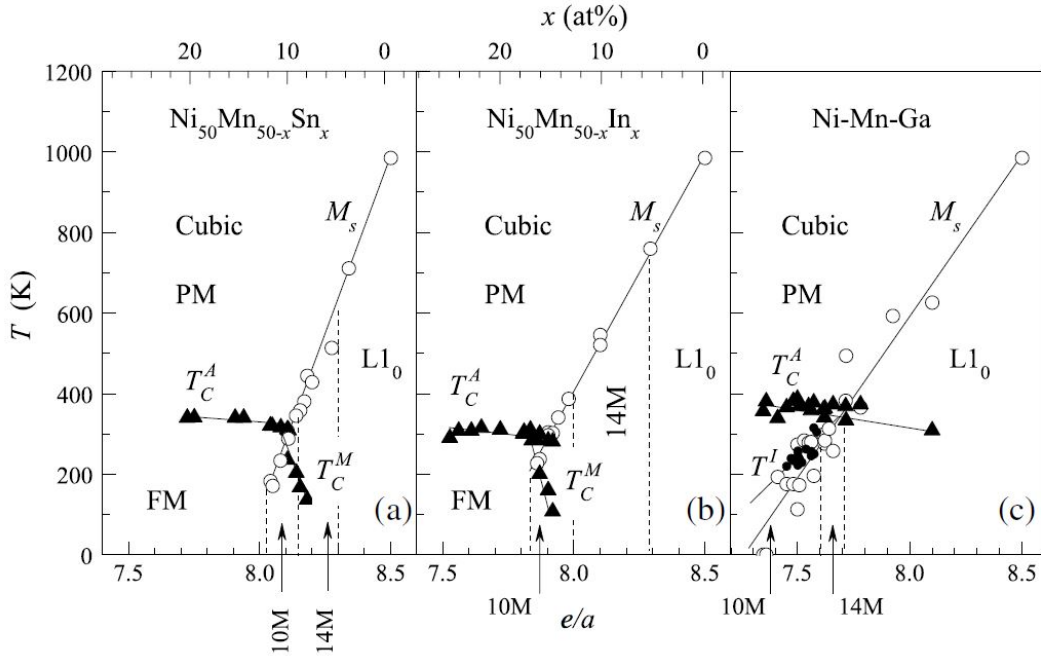


**Figure 2.8:** Magnetic and structural phase diagram of (a) Ni-Mn-Sn, (b) Ni-Mn-In and (c) Ni-Mn-Ga, reference [Pla09] fig.4. Isostructural regions are separated by dashed lines. Magnetic transitions are indicated by triangles. Martensitic transformations are shown by circles.

$B2$  structures. The Curie temperature of the austenite ( $T_C^A$ ) and martensite ( $T_C^M$ ) states are shown with triangles. The martensitic transformation  $M_S$  is shown with circles. The alloys can exhibit a  $5M$ ,  $7M$  and  $L1_0$  structure at low temperatures, which varies systematically with increasing  $e/a$ . The further decrease of the temperature leads also to inter-martensitic transformations whereby the  $L1_0$  structure is the ground state [Ç15a, Dut16]. The composition  $\text{Ni}_{50}\text{Mn}_{50}$  exhibits an  $L1_0$  structure and is AF with a very high Néel temperature  $T_N$  of about 1100 K [Kas59]. In general, an increase of  $M_S$  is observed with increasing  $e/a$ .  $T_C^A$  slightly decreases with increasing  $e/a$  and Mn content. This relates to the weakening of the FM coupling due to the increase in the number of Mn-Mn nearest neighbors, which leads to a strengthening of AF-exchange.  $T_C^M$  drops rapidly with increasing  $e/a$ , except for Ni-Mn-Ga. This is related to the increase of AF exchange, the FM exchange is expected to vanish when the stoichiometry reaches  $\text{Ni}_{50}\text{Mn}_{50}$ . However, no measurements have been carried out to determine  $T_N$  temperature in this composition-range.

### Tuning of the MCE in Heusler alloys

It can be seen in fig. 2.8 that varying the Mn content in Ni-Mn-X enables tuning the magnetic and structural transformation temperatures and thereby influencing the MCE. However, there are also further possibilities to tune the transition temperature and the MCE, which will be discussed in the following.

The field-induced martensitic transition in Ni-Mn-X leads to a MCE with an entropy change between  $9 \text{ J kg}^{-1} \text{ K}^{-1}$  and  $27 \text{ J kg}^{-1} \text{ K}^{-1}$  [Kre05b, Aks07, Kre07b, Bho07, Dub09, Got16b]. The martensitic transformation can be varied over a broad temperature-range by adjusting the X-element content. A further method to tune the martensite temperature is to dope Ni-Mn-X with a fourth element by substituting Ni, Mn, or X by Fe, Co or Cu, as in most common cases [Kre07a, Dub09, Got16b, Liu12a]. The doping can increase or decrease the entropy change at the transition.

Further optimization of the MCE can be attained by heat treatment influencing the chemical order, which has a large effect on the first-order transition [Ito08, Miy11]. For example, annealing of  $\text{Ni}_{50}\text{Mn}_{39}\text{Sn}_{11}$  above the  $B2/L1_0$  transition improves the chemical homogeneity, and the extension of the annealing-duration increases the intensity and sharpness of the martensite transformation and thereby the MCE [Sch08]. Direct  $\Delta T_{\text{ad}}$  measurements of doped and undoped Ni-Mn-X report values from 2 to 6 K [Aks07, Tit12, Liu12a].

A high  $\Delta T_{\text{ad}}$  is essential for magnetocaloric refrigeration, but it also has to be reversible. As mentioned previously, the width of the thermal hysteresis limits the reversibility of  $\Delta T_{\text{ad}}$  (chap. 2.1), especially when the applied field is not large enough to overcome the hysteresis. This was shown by  $\Delta T_{\text{ad}}$  measurements on  $\text{Ni}_{50}\text{Mn}_{35}\text{Sn}_{15}$  and  $\text{Ni}_{50}\text{Mn}_{35}\text{In}_{15}$  [Tit12].  $\text{Ni}_{50}\text{Mn}_{35}\text{Sn}_{15}$  exhibits a  $\Delta T_{\text{ad}}$  of  $-2.5 \text{ K}$  at the martensitic transition while  $\text{Ni}_{50}\text{Mn}_{35}\text{In}_{15}$  exhibits a  $\Delta T_{\text{ad}}$  of only  $-1.4 \text{ K}$ . The values are measured

in an applied field of 5 T. However, the martensitic transition in  $\text{Ni}_{50}\text{Mn}_{35}\text{Sn}_{15}$  has a thermal hysteresis of 30 K, while in  $\text{Ni}_{50}\text{Mn}_{35}\text{In}_{15}$  the hysteresis is only 16 K.  $\Delta T_{\text{ad}}$  measurements under field-cycling show that a reversal of the transformation cannot be achieved in  $\text{Ni}_{50}\text{Mn}_{35}\text{Sn}_{15}$ , since the hysteresis cannot be overcome by a field of 5 T. This leads to zero  $\Delta T_{\text{ad}}$  after the first application of the field. In contrast, a reversible  $\Delta T_{\text{ad}}$  of 0.7 K is observed in  $\text{Ni}_{50}\text{Mn}_{35}\text{In}_{15}$ . Here the field of 5 T is able to overcome the hysteresis (16 K), and a reverse transformation can be induced.

In reference [Nie16], it is demonstrated that the martensitic transformation can locally be promoted by artificial defects. Therefore, nano-indentations are inserted in a Ni-Mn-Ga epitaxial film. The plastic deformation in the vicinity of the indentation acts as an elastic stray field. This leads to a change in the nucleation barrier and decreases the hysteresis. Therefore a selective insert of defects can be used to tune the martensitic transition and the MCE.

### Decomposition of off-stoichiometric Heusler alloys

Annealing Heusler alloys above the  $B_2/L_{21}$  transition can increase atomic ordering. As opposed to this, heat treatment at about 150 K below the  $B_2/L_{21}$  transition leads to phase decomposition [Yuh09]. It turns out that off-stoichiometric  $\text{Ni}_{50}\text{Mn}_{25-y}\text{X}_y$  (X as Sn, In, Ga)  $0 < y < 25$  alloys decompose into stoichiometric, FM,  $L_{21}$   $\text{Ni}_{50}\text{Mn}_{25}\text{X}_{25}$  and AF,  $L_{10}$   $\text{Ni}_{50}\text{Mn}_{50}$  when annealed in the range  $600 \leq T \leq 750$  K [Cak16, Sch08, Kre16, Ç17a]. The decomposition leads to a change of the Mn content of the initial alloy shifting the martensitic transformation temperature to higher temperatures. In the case of  $\text{Ni}_{50}\text{Mn}_{37}\text{Sn}_{13}$  and  $\text{Ni}_{50}\text{Mn}_{35}\text{Sn}_{15}$ , a decrease in the transition temperature is observed after the decomposition [Yuh10].

A rather interesting effect can be observed in AF  $\text{Ni}_{50}\text{Mn}_{45}\text{In}_5$  and  $\text{Ni}_{50}\text{Mn}_{45}\text{Ga}_5$  Heusler alloys annealed at 650 K in a magnetic field. The decomposition leads in this case to the formation of FM  $\text{Ni}_{50}\text{Mn}_{25}\text{X}_{25}$  precipitates of nanometer dimensions which can be detected by X-ray diffraction [Din18]. Magnetization measurements indicate a strong pinning of the moment of the interface between the AF matrix and the FM precipitate along the field direction leading to the shell-FM effect [Cak16]. The effect is shown and described in a video [You16]. The pinned shell of the nano-precipitates cannot be rotated in external fields up to 5 T, whereas the FM  $\text{Ni}_{50}\text{Mn}_{25}\text{X}_{25}$  core is free to rotate. This leads to vertically shifted  $M(H)$ -curves [Cak16, Kre16, Ç17a]. The remanent magnetization of the FM precipitates is always positive or negative, depending on the direction of the applied field during annealing [Ç17b].

The vertically shifted  $M(H)$ -curves can only be observed when the precipitates have nanometer dimensions, since the effect is related to the surface-to-volume-ratio of the precipitates. The effect is masked when Ni-Mn-In is annealed at 750 K due to the larger precipitate-volume [Ç17b]. First studies on the size-determination are done on  $\text{Ni}_{50}\text{Mn}_{45}\text{In}_5$  as a function of annealing-temperature and time, by Scherrer

analysis [Din18]. This shows a systematic increase of the precipitate-size depending on annealing-temperature and time. It is shown that the alloys annealed at 650 K exhibit a precipitate-size of about 3 to 5 nm. Furthermore, the growth stops at this size and a longer annealing time leads only to an increase in the number of precipitates. The locking of the growth process can only be observed at 650 K while an increase of the precipitate-size is present for the annealing-temperatures 700 and 750 K.

The decomposition of Ni-Mn-X below the  $B_2/L2_1$  transition shows that the cooling procedure of the preparation has to be fast to ensure a homogeneous alloy. The quenching of the alloy leads instead to stress and strain in the sample which can be reduced by subsequent annealing at  $650 \leq T \leq 750$  K. However, this range corresponds to temperatures where decomposition takes place. A selective decomposition of Ni-Mn-X can therefore be a possibility to tune the magnetic properties and the hysteresis at first-order transitions. Due to this, further studies on the microstructure and interface-coupling between the AF matrix and the FM precipitates are necessary to understand this effect in more detail.

### 2.2.2 Transitions in $\text{Mn}_3\text{GaC}$ antiperovskite

$\text{Mn}_3\text{GaC}$  exhibits two transitions: A first-order transition at  $T_i = 164\text{ K}$  from a low-temperature AF state to a high-temperature FM state and a second-order transition at the Curie temperature  $T_C = 248\text{ K}$  from the FM state to the PM state [Bou66, Kan87a]. The magnetic transition from the AF to the FM state is accompanied by a decrease in the volume of the unit cell, while the structure of the alloy remains cubic. The transition can be regarded as a first-order magnetostructural transition, which is verified by the rapid change of the heat capacity of  $\text{Mn}_3\text{GaC}$  at  $T_i$  [Bou66, Gar83].

$\text{Mn}_3\text{GaC}$  shows an inverse MCE with a  $\Delta T_{ad}$  of about 5 K in a field change of 2 T [Toh03, Sch15]. The narrow thermal hysteresis of 4 K in combination with a large shift of  $T_i$  with a rate of  $-5\text{ K T}^{-1}$  leads to a fully reversible transition in fields up to 2 T. These field-values can be supplied by a permanent magnet making  $\text{Mn}_3\text{GaC}$  an interesting material for magnetocaloric refrigeration [Bou66, Toh03, Ç12, Sch15].

The structural and magnetic properties of  $\text{Mn}_3\text{GaC}$  were firstly studied by L. Howe and H.P. Myers [How57]. Later, D. Fruchart et al. studied the structural and magnetic properties in more detail [Fru70, Fru78]. The alloy has an antiperovskite or metallic perovskite structure with  $Pm-3m$  symmetry. Fig. 2.9(a) shows the unit cell of  $\text{Mn}_3\text{GaC}$ . The carbon atom is located at the  $(\frac{1}{2}, \frac{1}{2}, \frac{1}{2})$  position in the center of an octahedron of Mn atoms, and the Ga atoms are located at  $(0, 0, 0)$  [Fru70]. The cubic cell has a lattice constant of 0.896 nm [Bou66, Fru70, Kan87b, Toh03, Ç14b].

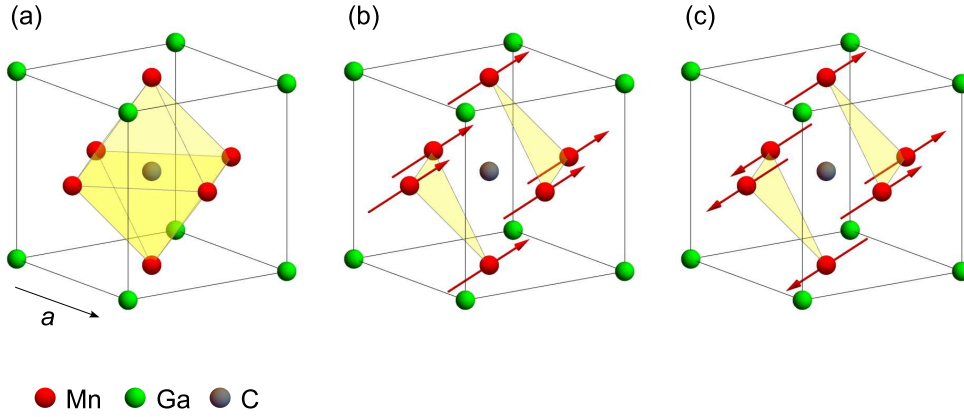


**Figure 2.9:** (a) Antiperovskite  $\text{Mn}_3\text{GaC}$   $Pm-3m$  structure. Ferromagnetic (b) and antiferromagnetic (c) structure of  $\text{Mn}_3\text{GaC}$ . This graphic is partly based on fig.5 in [Fru78, Gar83]

The magnetic structure of the high-temperature FM state is shown in fig. 2.9(b). The magnetic moments of the Mn atoms ( $1.2\mu_B$ ) point along the  $[1,1,1]$  direction so that it is the easy axis of the magnetization [Fru78, Gar83]. In the low-temperature AF state, the Mn atoms have a magnetic moment of  $1.8\mu_B$  [Fru70, Fru78, Ç14b], and



point along the [1,1,1] direction (see fig. 2.9(c)); with the magnetization in alternating planes aligning antiferromagnetically.

The first-order AF/FM transition at 164 K is an isostructural transition, which is accompanied by a volume decrease of 0.5% in the FM state. The magnetic moment likewise decreases from  $1.8\mu_B$ (FM) to  $1.2\mu_B$ (AF) [Fru78, Mot88, Ç14b]. Therefore, the transition can be either induced by an increase of the temperature, by applying hydrostatic pressure, or by applying a magnetic field. In all cases the transition temperature shifts to lower values [Bou66, Toh03, Kan87b, Ç14b]. Neutron diffraction studies carried out under magnetic field show that both phases are present at the transition [Ç14b]. However, the FM state is progressively stabilized with increasing field. The studies show further that the lattice parameters, the magnetic moments, and the vibrational properties in the range of phase-coexistence deviate from the values in pure AF and FM states. This can be explained by local strains and crystallographic disorder which also lead to the hysteresis of the transition.

Isothermal field-dependent magnetization measurements in the vicinity of  $T_i$  give an entropy change of  $\Delta S = 15 \text{ Jkg}^{-1}\text{K}^{-1}$  in a field of 1 T [Toh03]. A  $\Delta T_{ad}$  of  $-5.4 \text{ K}$  is calculated by eq.(2.9) and (2.15) using  $\Delta S$  and the heat capacity [Gar83]. Direct measurements of  $\Delta T_{ad}$  show an inverse MCE with a  $\Delta T_{ad}$  between  $-3.2 \text{ K}$  and  $-4.7 \text{ K}$  [Ç12, Sch15].

### Tuning of the transition of $\text{Mn}_3\text{GaC}$ by doping

$\text{Mn}_3\text{GaC}$  offers many possibilities for doping with various elements. This section presents an overview on the effect of doping  $\text{Mn}_3\text{GaC}$  on the transition temperatures and the structure.

Mn can be substituted by other transition metals as example Fe, Ni, Co and Cr [Wan10, Toh04, Har93]. The substitution of Mn with Co in  $\text{Mn}_{3-x}\text{Co}_x\text{GaC}$  ( $0 \leq x \leq 0.05$ ) [Toh04] leads to a decrease of  $T_i$  down to 100 K with increasing  $x$ . The substitution also increases the shift of  $T_i$  with applied field from a rate of  $-5 \text{ K T}^{-1}$  ( $x = 0$ ) to  $-9 \text{ K T}^{-1}$  ( $x = 0.05$ ).  $\Delta S$  of about  $15 \text{ Jkg}^{-1}\text{K}^{-1}$  is not effected by the increase of Co content.  $\text{Mn}_{3-x}\text{Co}_x\text{GaC}$  shows a MCE in a large temperature-range between 50 and 160 K which makes these alloys interesting for low temperature magnetic refrigeration.

Doping with Ni leads in  $\text{Mn}_{3-x}\text{Ni}_x\text{GaC}$  ( $0 \leq x \leq 0.1$ ) to a decrease in the lattice parameter  $a$  with increasing Ni content [Wan10]. Furthermore, a intermediate canted FM state is observed between the AF and the FM state. The transition temperature from the FM state to intermediate FM state decreases with increasing  $x$ . The same behavior is observed in the transition temperature from the intermediate FM to the AF state. On the other hand,  $T_C$  from the FM to the PM state increases with increasing Ni content while the saturation magnetization also increases. Ni has three more valence electrons than Mn and can therefore influence the density of states (DOS) near the Fermi energy  $E_F$  which is otherwise controlled by the Mn 3d-electrons [Mot88, Shi02].



An intermediate FM state is also observed in  $\text{Mn}_3\text{GaC}$  when the alloy is compressed at  $p > 3$  kbar [Kan87b, Kam98]. The substitution of Mn by Ni acts as a chemical pressure effect enhancing the FM interactions. The shift of transition temperature towards lower temperatures can therefore be explained as a combination of a chemical pressure effect and a correlating electronic band filling effect due to the substitution of Mn with Ni. The substitution of Mn with Fe also has a similar effect as the substitution of Mn with Ni. Studies on  $\text{Mn}_{2.95}\text{Fe}_{0.05}\text{GaC}$  show a decrease of  $a$  and  $T_i$  compared to non-doped  $\text{Mn}_3\text{GaC}$  [Har93]. Furthermore, an intermediate FM state between the AF phase and the FM phase is also observed in this alloy.

The substitution of Mn with Cr leads in  $\text{Mn}_{3-x}\text{Cr}_x\text{GaC}$  ( $0 \leq x \leq 0.05$ ) to an increase of  $T_i$  and an increase of the lattice constant  $a$  with increasing  $x$  [Har93]. The alloy shows no presence of an intermediate FM state. In fact, the FM state is completely suppressed for  $x > 0.15$ , and the alloys transforms directly from the AF phase to the PM phase. Parallel to this,  $T_C$  decreases with increasing amount  $x$ . Cr has one electron less than Mn while Ni, Fe, and Co have more electrons. The difference in the number of electrons can also be the reason why Cr-doped  $\text{Mn}_3\text{GaC}$  show an increase in  $T_i$  and a decrease in  $a$  while Ni, Fe, and Co-doped  $\text{Mn}_3\text{GaC}$  show a decrease in  $T_i$  and an increase in  $a$  compared to non-doped  $\text{Mn}_3\text{GaC}$ .

Another option to manipulate the magnetic transition in  $\text{Mn}_3\text{GaC}$  is to substitute Ga by Al or Sn, whereby Al has the same number of valence electrons as Ga and doping with Sn increases the number of electrons [Koy04, Wan09, Wan11].

The substitution of Mn with Al in  $\text{Mn}_3\text{Ga}_{1-x}\text{Al}_x\text{C}$  ( $0 \leq x \leq 0.15$ ) shows that the lattice parameter  $a$  decreases linearly with increasing Al concentration  $x$  [Koy04, Wan11]. The results of magnetization measurements suggest the presence of an AF state at low temperature, an intermediate phase, a FM phase, and a PM phase at high temperatures. The transition temperature from the AF phase to the intermediate phase decreases with increasing Al content, while the transition temperature from intermediate to FM phase remains constant. On the other hand,  $T_C$  increases. The smaller Al atom can act as a positive chemical pressure on  $\text{Mn}_3\text{Ga}_{1-x}\text{Al}_x\text{C}$  resulting in a decrease in  $a$  since the FM phase has a smaller volume than the AF phase, the FM phase is further stabilized.

The  $\text{Mn}_3\text{SnC}$  alloy has in comparison to  $\text{Mn}_3\text{GaC}$  no sharp transformation between a AF and a FM phase but exhibits a FI state [Wan09]. The alloy undergoes a first-order transition to the PM phase at  $T_C \sim 279$  K with a narrow thermal hysteresis of  $\sim 2.5$  K. The entropy change  $-\Delta S$  at this transition is comparable to the one of  $\text{Mn}_3\text{GaC}$  which makes this alloy also interesting for magnetocaloric application.

A further possibility of shifting  $T_i$  to higher temperatures is by the substitution of carbon with nitrogen. Reference [l'H79a] and [l'H79b] show that an increase of the nitrogen content  $x$  in  $\text{Mn}_3\text{GaC}_{1-x}\text{N}_x$  leads to an increase of  $T_i$  while  $T_C$  decreases rapidly. Already, for  $x > 0.2$ , the FM phase is completely suppressed. These can be used to suppress also the transitional hysteresis and will be discussed in the next section.

The transition temperatures  $T_i$  and  $T_C$  are also strongly correlated to carbon de-

iciencies in  $\text{Mn}_3\text{GaC}$ . An decrease of the carbon content leads to a decrease of  $T_i$  and an increase of  $T_C$  [Lew06, Dia14]. A carbon deficiency of about 4% is sufficient to destabilize the AF state completely [Fru78]. In  $\text{Mn}_3\text{GaC}$  the magnetic moment is located at the Mn atom, so that direct Mn-Mn and indirect Mn-C-Mn interactions have to be taken into account to describe the magnetic transitions. In the case of  $\text{Mn}_3\text{GaC}$ , the superexchange Mn-C-Mn interaction is strongly AF while the Mn-Mn interaction is weak FM [Goo63]. In alloys with carbon deficiency, the AF interactions are weakened and the FM interaction becomes dominant shifting  $T_i$  to lower temperatures.

The sharp change in the magnetization with a simultaneous change of the cell-volume is a characteristic of Mn-based  $\text{Mn}_3\text{AC}$  (A as Ga, Sn and Al) antiperovskites. The DOS at  $E_F$  of  $\text{Mn}_3\text{GaC}$  and  $\text{Mn}_3\text{SnC}$  show that the Mn 3d-electrons are dominant in the band at  $E_F$  [Mot88].

The sharp first-order transition and the multiple methods to tune the transition temperature and the electronic configuration makes  $\text{Mn}_3\text{GaC}$  interesting for magnetocaloric applications.

### Influence of long-range FM ordering on hysteresis and kinetic arrest

The partial substitution of carbon with nitrogen in  $\text{Mn}_3\text{GaC}$  shifts  $T_i$  to higher temperatures by enhancing AF exchange. In the case of a  $\text{Mn}_3\text{GaC}_{0.85}\text{N}_{0.15}$ ,  $T_i$  and  $T_C$  approach each other [Ç13]. The coincidence of the two transition temperatures leads to an enhanced paramagnetic (EPM) state without long-range FM order. Neutron polarization and depolarization experiments on  $\text{Mn}_3\text{GaC}$  and  $\text{Mn}_3\text{GaC}_{0.85}\text{N}_{0.15}$  show that in  $\text{Mn}_3\text{GaC}_{0.85}\text{N}_{0.15}$  no long-range ferromagnetism occurs and no FM domains are formed [Ç16]. The temperature-dependent magnetization of  $\text{Mn}_3\text{GaC}_{0.85}\text{N}_{0.15}$  shows a decrease of the transition temperature with increasing applied field by a rate of  $-2.5 \text{ K T}^{-1}$  [Ç13]. The study shows further that the transition exhibits no thermal or magnetic hysteresis.  $\Delta T_{\text{ad}}$  measurements show a fully reversible inverse MCE with  $\Delta T_{\text{ad}}$  of 3.2 K in an applied field of 3 T. The absence of hysteresis enables a full reversible MCE in small fields which makes these alloy interesting as a magnetocaloric refrigerant and raises also the question whether long-range FM ordering has an influence on the hysteresis at first-order transitions. For this reason an investigation of the MCE at first-order transitions from the AF to the FI state is worthwhile for searching materials with narrow or no thermal hysteresis.

Another effect which influences the properties of the first-order transition is the kinetic arrest. This effect was found in carbon deficient  $\text{Mn}_3\text{GaC}$  [Ç15b]. Magnetization studies on  $\text{Mn}_3\text{GaC}_{0.9}$  show besides the shift of  $T_i$  and  $T_C$  (mentioned above) also a thermal broadening of the first-order transition. The effect can be explained by the enhancement of FM exchange in the AF phase due to carbon deficiency. The inhomogeneous magnetism in the ground state leads to effects of kinetic arrest which can also effect the MCE at the first-order transition.

### 2.2.3 $\text{Mn}_{2-y}\text{X}_y\text{Sb}$ pnictides (X:Ti, V, Cr, Fe)

A further interesting material class for magnetocaloric applications are the  $d$ -metal pnictides  $\text{MM}'\text{A}$ , where M and M' are transition metals and A is P, As or Sb [Fru05]. In this thesis I focus on the  $\text{Mn}_2\text{Sb}$ -based pnictides due to their broad spectrum of magnetic transitions depending on the doping element and composition.  $\text{Mn}_2\text{Sb}$  is a FI with a Néel temperature of  $T_N = 550$  K [Hea55, Wil57]. Fig. 2.10(a) shows the  $\text{Mn}_2\text{Sb}$  unit cell, with tetragonal  $P4/nmm$  symmetry and lattice constants  $a = 0.408$  nm and  $c = 0.656$  nm. The Mn atoms are located at two different sites Mn(I) and Mn(II). Mn(I) occupies the 2a positions  $(0, 0, 0)$  and  $(\frac{1}{2}, \frac{1}{2}, 0)$ , while Mn(II) is located at the 2c positions  $(\frac{1}{2}, 0, z_1)$  and  $(0, \frac{1}{2}, \bar{z}_1)$ . Sb occupies  $(\frac{1}{2}, 0, z_2)$  and  $(0, \frac{1}{2}, \bar{z}_2)$  positions, where  $z_1 = 0.295$  and  $z_2 = -0.280$  [Hea55, Alp63]. Due to the different electronic states of Mn(I) (mix of  $3d^5 4s^2$  and  $3d^7$ ) and Mn(II) ( $3d^5 4s^2$ ), the magnetization in the atomic planes of the two Mn sites align antiparallel.

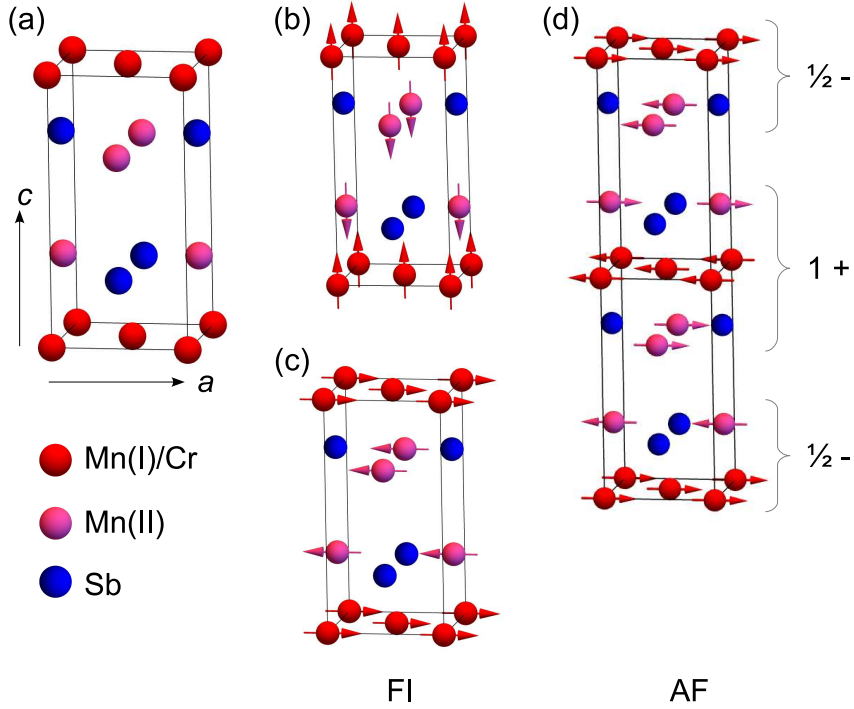


**Figure 2.10:** (a) Crystal structure of  $\text{Mn}_2\text{Sb}$ . FI structure above (b) and below (c) 240 K. In the case of Cr doping,  $\text{Mn}_{2-y}\text{X}_y\text{Sb}$  exhibits a low temperature AF structure (d). The figures are partially based on fig. 1 in [Kan84, Clo61].

Two different magnetic structures were observed for the FI state [Wil57]. Fig. 2.10(b) shows the magnetic structures above 240 K, whereby the magnetization easy-axis is along the  $c$ -axis. Fig. 2.10(c) shows the structure below 240 K. In this case, the magnetization easy-axis is rotated by  $90^\circ$  and is along the  $a$ -axis. The total saturation magnetization at room temperature is  $1.18\mu_B$ , where Mn(I) has a moment of  $-1.48 \pm 0.15\mu_B$  and Mn(II) a moment of  $2.66 \pm 0.15\mu_B$  [Alp63].

The substitution of Mn in  $\text{Mn}_{2-y}\text{X}_y\text{Sb}$  with a third element X as Ti, V, Cr, Fe or Co, can change the magnetic transition behavior. Substituting Cr, V or Co leads to a first-order transition from a low-temperature AF state to a high-temperature FI state [Swo60, Bit62, Kan84]. The magnetic AF/FI transition is accompanied by a contraction in the lattice parameter  $c$  for the FI state and a change in the resistivity [Jar61]. The increase of the Cr or Co amount  $y$  leads to an increase of the transition temperature  $T_i$ .  $T_i$  can also be shifted to lower temperatures by applying pressure or magnetic field [Tek15, Bar04].

In contrast to doping with Cr, V and Co, substituting Mn with Ti leads to an extension of  $c$ . These different behaviors are related to the different occupation of the Mn sites. In case of Cr, V, and Co, the doping-element occupies the Mn(I) sites, while Ti occupies the Mn(II) sites [Aus63, Bla78, Kan84]. This suppresses the AF phase.

The contraction of the lattice parameter  $c$ , ( $\Delta c$ ), depends on the doping-element and its amount. However, studies on concentration on a series of Cr-doped  $\text{Mn}_{2-y}\text{Cr}_y\text{Sb}$  ( $0 \leq y \leq 0.16$ ) compounds show that the AF/FI transition always appears when  $c$  falls below a critical value of about 0.653 nm [Swo60, Bie62, Dar63]. This behavior of the transition can be described by Kittel's model of exchange-inversion [Kit60]. The model describes the occurrence of a first-order magnetic transformation when the net exchange interaction, which is coupled with the elastic strain of the lattice, changes sign. The model assumes a magnetic structure with two exchange coupled lattices, whereby the interlattice exchange energy  $E_{\text{ILEE}}$  can be described as

$$E_{\text{ILEE}} = -\rho(c - c_c)V\mathbf{M}_A \cdot \mathbf{M}_B, \quad (2.20)$$

$\rho$  denotes  $\partial\beta/\partial c$ , where  $\beta$  is the molecular field constant connecting the magnetization  $\mathbf{M}_A$  and  $\mathbf{M}_B$  of the two sublattices,  $V$  is the lattice volume, and  $c_c$  is the critical lattice parameter at which the interlattice exchange interactions changes sign. At a first-order magnetic transition, the elastic energy of the lattice also has to change. In this case, the contraction of the lattice ( $\Delta c$ ) is proportional to the square of the magnetization  $M^2$  which is also confirmed for Cr-doped  $\text{Mn}_2\text{Sb}$  [Clo61].

Neutron diffraction studies on Cr-doped  $\text{Mn}_{2-y}\text{Cr}_y\text{Sb}$  exhibit a FI phase above  $T_i$  similar to that in  $\text{Mn}_2\text{Sb}$  (fig. 2.10(b)) and an AF phase below  $T_i$  as shown in fig. 2.10(d) [Clo60]. Compared to the low-temperature FI structure of  $\text{Mn}_2\text{Sb}$  (fig. 2.10(c)), AF  $\text{Mn}_{2-y}\text{Cr}_y\text{Sb}$  (fig. 2.10(d)) has antiparallel ordering of the Mn(I) layers as well as antiparallel ordering of the Mn(II) layers having no Mn(I) layer inbetween. The

magnetic moment in  $\text{Mn}_{2-y}\text{Cr}_y\text{Sb}$  rotates at the AF/FI transition by  $90^\circ$  into the  $c$ -plane. The rotation of the easy-axis of magnetization through the exchange inversion contributes to the energy of Bloch domain-walls which lowers the energy and also reduces the dimension of the wall [Kit60]. The low domain-wall energy makes it easier to induce the first-order AF/FI transition and could explain the low magnetic hysteresis in this alloy, which makes it interesting for magnetocaloric cooling.

First studies on the entropy and adiabatic temperature change at the first-order transition on Cr-doped  $\text{Mn}_{2-y}\text{Cr}_y\text{Sb}$  ( $0 \leq y \leq 0.12$ ) display a  $\Delta S$  between  $7.5 \text{ Jkg}^{-1}\text{K}^{-1}$  and  $5.5 \text{ Jkg}^{-1}\text{K}^{-1}$  depending on the Cr content [Car13]. Temperature and field-dependent magnetization measurements show also a decrease of  $T_i$  with increasing field at a rate of  $-3 \text{ K T}^{-1}$ . Furthermore, a narrow thermal hysteresis of 2 K has been observed independent of the Cr concentration. The substantial  $\Delta S$ , the large shift of  $T_i$ , and the narrow thermal hysteresis make this alloy an interesting material for magnetocaloric refrigeration.

Several studies on Cr-doped  $\text{Mn}_{2-y}\text{Cr}_y\text{Sb}$  show, however, a residual magnetization in the AF phase that reduces the MCE at the first-order transition [Dar63, Car13, Tek15, Tek17b]. X-ray diffraction studies show the presence of a FM MnSb phase with  $T_C = 585 \text{ K}$ , explaining the residual magnetization [Oki68]. The presence of MnSb cannot be prevented and is independent of the Cr content. The amount of MnSb impurity-phase, however, can be largely suppressed by substituting Sb with Ga or In [Tek15, Tek17b]. The suppression of the MnSb phase reduces the FM background and increases the entropy change at the AF/FI transition. Direct adiabatic temperature change measurements show a fully reversible  $\Delta T_{ad}$  of 0.7 K to 1.7 K depending on the Cr content.

Studies on  $\text{Mn}_{1.82}\text{Co}_{0.18}\text{Sb}_{0.95}\text{In}_{0.05}$  show, however, that adding In leads to a broadening of the thermal hysteresis [Tek17a]. In also stabilizes the FI state and shifts the transition temperature to lower values. The study shows furthermore the presence of kinetic arrest in  $\text{Mn}_{1.82}\text{Co}_{0.18}\text{Sb}_{0.95}\text{In}_{0.05}$  and  $\text{Mn}_{1.82}\text{Co}_{0.18}\text{Sb}$ , whereby the effect increases in the case of In-doping. These effects are similar to the behavior in carbon deficient  $\text{Mn}_3\text{GaC}$  [Ç15b]. They lead to hysteresis broadening and need to be avoided to improve the reversibility of the MCE.



## 3 Experimental methods

This chapter provides an overview of the experimental techniques that were used for the synthesis and the characterization of the samples. The first part discusses sample-synthesis. The characterization techniques are divided into the sections structural analysis, magnetic characterization, and adiabatic magneto-calorimetry.

### 3.1 Sample preparation

Two different sample-preparation techniques are used in this thesis: arc-melting and solid state reaction. These are discussed individually below.

#### **Arc melting:**

The arc-melting sample-preparation method was used for preparing Ni-Mn-based Heusler alloys and  $\text{Mn}_2\text{Sb}$ -based pnictides. In case of the arc-melted samples, pure elements were used to obtain an ingot of 4 g. The purity of the elements is 99.95 % or better. To reduce MnO contamination, the raw, oxidized Mn was cleaned by arc-melting under argon atmosphere. Subsequently, all constituent elements were molten together. To achieve homogeneity, the ingot is turned, and the melting process is repeated five times. Due to the high vapor pressure of Mn, the final composition contains less Mn than the aimed concentration. To compensate the evaporation losses, either 3 % Mn is given as excess, or the concentration is balanced after obtaining the 4 g sample. To improve the chemical order, the sample is annealed under argon atmosphere in a quartz tube. The annealing takes place at 1073 K for 5 days. Subsequently, the quartz tube is quenched in ice water. For energy dispersive X-ray spectroscopy (EDX), the ingot is polished with 1200-grit SiC abrasive paper. The structural and magnetic characterization by X-ray diffraction (XRD) and superconducting quantum interference device (SQUID) are done on powder samples prepared by grinding a part of the ingot. To release the stress after grinding, the powder is again encapsulated in a quartz tube under argon atmosphere and annealed at 1073 K for 1 day and quenched in ice water.

The annealing studies in Ni-Mn-based Heusler alloys in presence of a magnetic field are performed in a furnace which is incorporated in the SQUID magnetometer. The furnace operates in the temperature-range of  $300 \leq T \leq 800$  K and the field can be varied between 0 and 5 T.

#### Solid state reaction:

The solid state reaction preparation technique is used to synthesize  $\text{Mn}_3\text{GaC}$ -based antiperovskites. Powder and small pieces of the constituent elements are mixed in proportion to obtain a 4 g sample. Firstly, the powder-mixture is encapsulate in a quartz tube under argon atmosphere and annealed at 1073 K for 5 days. Afterwards, the sintered powder is ground. The powder is then pressed at a pressure of  $6.3 \times 10^{10} \text{ Nm}^{-2}$  to a pellet. The sample is then again encapsulated in quartz under argon atmosphere and annealed at 1073 K for another 5 days. For better homogeneity, the pellet is again ground and pressed and annealed for a second time. For characterization methods requiring powder samples, a small part of the final pellet is scraped off.

#### Growth of $\text{Mn}_3\text{GaC}$ single crystals by solid state reaction:

$\text{Mn}_3\text{GaC}$  single crystals grow as a by-product of a solid state reaction of off-stoichiometric  $\text{Mn}_x\text{Ga}_y\text{C}$  ( $x = 4, 5$  and  $y = 2, 3$ ). However here, after the annealing step, phase-separation is observed. Fig. 3.1(a) shows a pellet of a decomposed  $\text{Mn}_4\text{Ga}_2\text{C}$  with a precipitate on top. Fig. 3.1(b) is a scanning electron microscope (SEM) image of the surface of this precipitate containing cubic  $\text{Mn}_3\text{GaC}$  crystals highlighted in red. The faceting suggests the single crystallinity of the crystals. The crystals can be separated by grinding the sample and subsequently screening the granular powder.

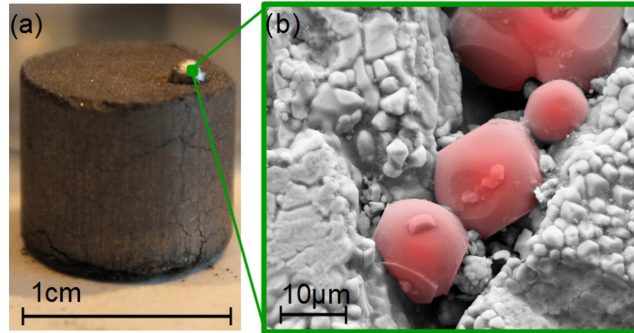


**Figure 3.1:** (a) Off-stoichiometric  $\text{Mn}_4\text{Ga}_2\text{C}$  pellet with segregation on top. (b) SEM image of the surface of the segregation, cubical faceting  $\text{Mn}_3\text{GaC}$  single crystals are highlighted in red.



## 3.2 Structure analysis

This section discusses X-ray diffraction and electron microscopic methods for structural characterization.

### 3.2.1 Powder X-ray diffraction

The crystal structure of the sample is analyzed by XRD. A PANalytical X-Pert PRO diffractometer is used for measurements at room temperature, and a Philips PW1729 is used for temperature-dependent structure analysis. Both instrument were used in the Bragg-Brentano geometry with continuous  $\theta$ - $2\theta$  scan with step size of  $0.01^\circ$  and a scanning speed of  $0.001^\circ\text{s}^{-1}$ . Copper radiation with wavelength  $\lambda_{K_{\alpha 1}} = 0.15405\text{ nm}$  and  $\lambda_{K_{\alpha 2}} = 0.15443\text{ nm}$  is implemented in both diffractometers. The powder is spread on a zero-background holder for the X-Pert Pro instrument.

In the case of PW1729, the powder is fixed with Apiezon grease on a aluminium holder. The sample holder is fully covered with powder to avoid diffraction from the holder. The sample stage is cooled by evaporated liquid nitrogen with constant gas-flow. Temperatures in the range  $120 < T < 400\text{ K}$  can be controlled. The diffractogram were analyzed by *FullProf Suite* software to determine the crystal structure and the lattice constants [RC93].

### 3.2.2 Electron microscopy

The microstructure of the surface of the bulk sample is analyzed by a Zeiss LEO 1530 SEM. The SEM includes an in-lens and a secondary electron (SE2) detector.

The chemical composition of the sample is determined by an Oxford Instruments XMAX 80 mm<sup>2</sup> EDX detector, and the spectra are analyzed using INCA 4.14 software (Oxford Instruments). The EDX-spectra are calibrated by a Cu-reference before each analysis. Additionally, an Oxford Instruments Nordlys electron backscatter diffraction (EBSD) detector is adapted to the SEM which enables a microstructural-crystallographic characterization of the surface of the sample. The EBSD technique is capable of identifying the texture, defects, and the grain morphology of the surface, which is used in this thesis to verify the single crystallinity of the Mn<sub>3</sub>GaC crystal. The electron backscatter pattern, or the Kikuchi-pattern, is generated by the wide-angle inelastic scattering of the primary electron beam and the atoms. A part of the incoming electrons interfere at the lattice-planes and produce the electron backscatter pattern which is then detected by a charge coupled device (CCD) camera. The spatial resolution of the EBSD depends on the spot size of the electron beam.

The patterns are processed by Flamenco software by CHANNEL 5, and the structure can be identified using a corresponding database. Since the database did not contain the Mn<sub>3</sub>GaC crystal structure, the electron backscatter pattern was simulated using

$Pm - 3m$  symmetry and a lattice constant of 0.88 nm for  $Mn_3GaC$ . Fig. 3.2(a) shows an example of an electron backscatter pattern of the  $Mn_3GaC$  crystal (see chap. 4.2). As the next step (fig. 3.2(b)), the band edges in the pattern are detected which are then compared with the simulated pattern (fig. 3.2(c)). The crystallographic orientation of the sample surface is indexed in fig. 3.2(d).

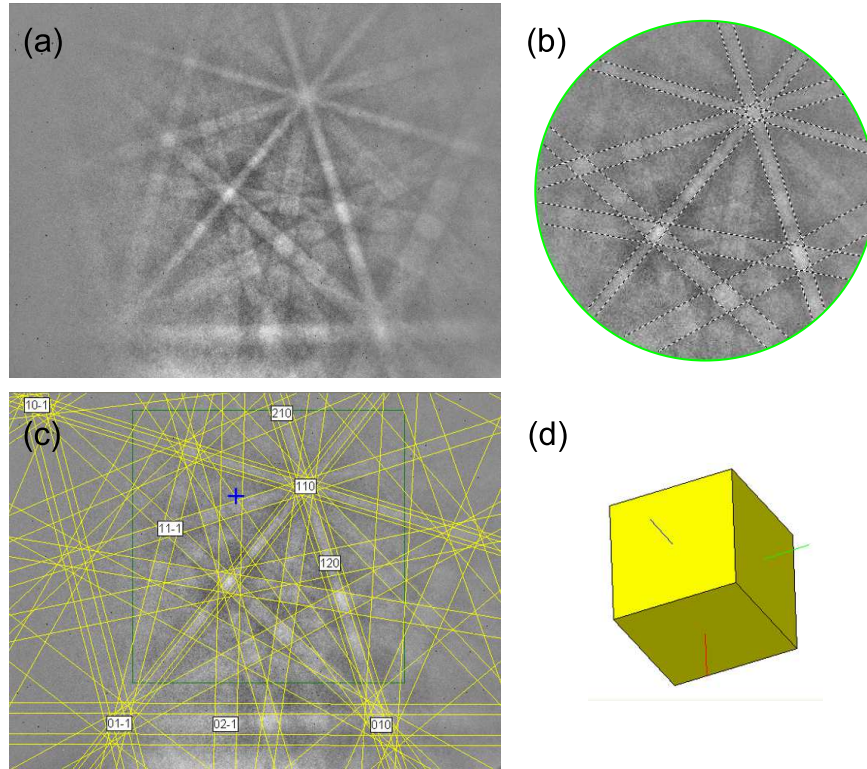


**Figure 3.2:** (a) Electron backscatter pattern of the  $Mn_3GaC$  crystal. (b) Area of band detection with highlighted band edges. (c) Electron backscatter pattern with concurrent simulation of  $Mn_3GaC$  crystal structure indexing the crystal orientation (d).

### 3.3 Magnetic characterization

A thorough knowledge of the magnetic properties of a material is essential for understanding the MCE at first and second-order magnetic transitions. This section gives an overview on the devices and techniques which are used for magnetic characterization.

In chap. 2.1, we show that the field-induced phase transition can occur under isothermal or adiabatic conditions leading either to a change in entropy or to a change in sample temperature. A magnetic characterization under isothermal and adiabatic conditions is performed to compare both transformation paths. The setups used are described in the following sections.

The last section of this chapter describes FMR and electron spin resonance (ESR) techniques. These techniques were employed to study magnetic anisotropy.

#### 3.3.1 Magnetometry

A SQUID and a PPMS-14 (physical property measurement system) are used for magnetization studies under isothermal conditions. Both devices measure the magnetization as a function of temperature  $M(T)$  and magnetic field  $M(B)$ . The SQUID magnetometer (Quantum Design MPMS XL) reaches a maximum field of 5 T and has a standard temperature range of  $5 \leq T \leq 400$  K. The temperature range can be extended to  $300 \leq T \leq 800$  K by a furnace which can be inserted into the cryostat of the magnetometer. The magnetization measurements can be performed in two different scan modes depending on the magnetic signal. Samples with large magnetic moment  $300$  to  $10^{-8}$  Am<sup>2</sup> are linearly moved through the detection coils (DC mode). For small signals  $10^{-5}$  to  $10^{-5}$  Am<sup>2</sup>, a reciprocating sample option (RSO) is used to reduce the signal to noise ratio. The PPMS-14 (Quantum Design) is used for magnetization measurements in fields up to 14 T and in the temperature range  $5 \leq T \leq 400$  K.

The isofield studies of the magnetization  $M(T)$  are performed using a zero-field-cooled (ZFC), field-warmed (FW), and field-cooled (FC) protocol. A bifurcation in the ZFC and FC magnetization measurement provide information on the presence of mixed FM/AF interaction [Zie75, Wac83, Dum02, May17]. Any difference in FC and FW  $M(T)$  paths issues information on the presence of first-order structural transformations. For a ZFC measurement, the sample is cooled in zero-field from 380 to 5 K to ensure a unmagnetized state. Subsequently, a field is applied and  $M(T)$  is measured while the temperature is increased from 5 to 380 K. Afterwards, the FC-curve is measured at applied field by decreasing the temperature from 380 to 5 K. The FW-curve is recorded during reincreasing the temperature from 5 to 380 K.

Isothermal  $M(B)$  measurement are carried out to determine the saturation magnetization  $M_S$ , saturation field  $B_S$ , the coercive field  $B_C$ , and the remanent magnetization  $M_R$ . Additionally,  $M(B)$  can be used to determine the total isothermal entropy change  $\Delta S_T$ . In chap. 2.1 eq. (2.11), we show that  $\Delta S_T$  can be calculated by numerically

integrating  $\partial M/\partial T$  in the field range  $H_1 \leq H \leq H_2$  using the relationship

$$\begin{aligned}\Delta S_T &= \int_{H_1}^{H_2} \left( \frac{\partial M}{\partial T} \right)_H dH \\ &\approx \frac{1}{T_i - T_{i+1}} \int_{H_1}^{H_2} (M(T_i) - M(T_{i+1})) dH.\end{aligned}\tag{3.1}$$

This method is actually not valid at pure first-order transitions, due to the discontinuous nature of  $M(T)$  at the transition [Gig99]. However, most magnetocaloric materials show a finite width at the transition, causing  $M(T)$  to spread over the transition range [Dub12]. In the case of a first-order transition, care has to be taken that the sample is brought to a well defined state before the  $M(B)$  measurement is performed. Namely, the sample is warmed or cooled far below or above the transition temperature before each  $M(B)$  measurement.

The magnetization measurements under adiabatic conditions were performed in pulsed magnetic fields at the Helmholtz-Zentrum Dresden-Rossendorf at the High Magnetic Field Laboratory (HLD-EMFL) in Dresden [Wos07]. A magnetic field-pulse is generated by a solenoid with a pulse duration of 75 ms with the maximum field-pulse reaching 71 T [Zhe06]. The magnetization of the sample is measured by a system of pick-up coils [Sko11]. Fig. 3.3(a) shows schematically the pick-up coil system, and fig. 3.3(b) shows the actual unit. The field pick-up coil (1) measures the induced voltage proportional to the magnetic field change  $dB/dt$ . The magnetic field is subsequently calculated by integrating the voltage over time and is normalized by a reference measurement. A sufficient distance between the field pick-up coil and the position of the sample (2) minimizes the influence of the magnetization of the sample on the field measurement. The sample is placed at the center of the magnetization pick-up coil which detects the magnetic signal and the magnetic field. To detect only the magnetization of the sample, the magnetization pick-up coil is additionally connected in series with a compensation coil compensating the field-signal so that only the magnetization signal is read. At each temperature setting, the sample is removed and a reference measurement is done to detect the background signal. Since background signals cannot be fully avoided, a fine compensation circuit is connected to the unit to compensate the background signal. Fig. 3.3(c) shows the plastic tube sample holder. The sample is fixed with a toothpick and covered with cloth to avoid movement. A detailed description of the setup can be found in [Sko11].

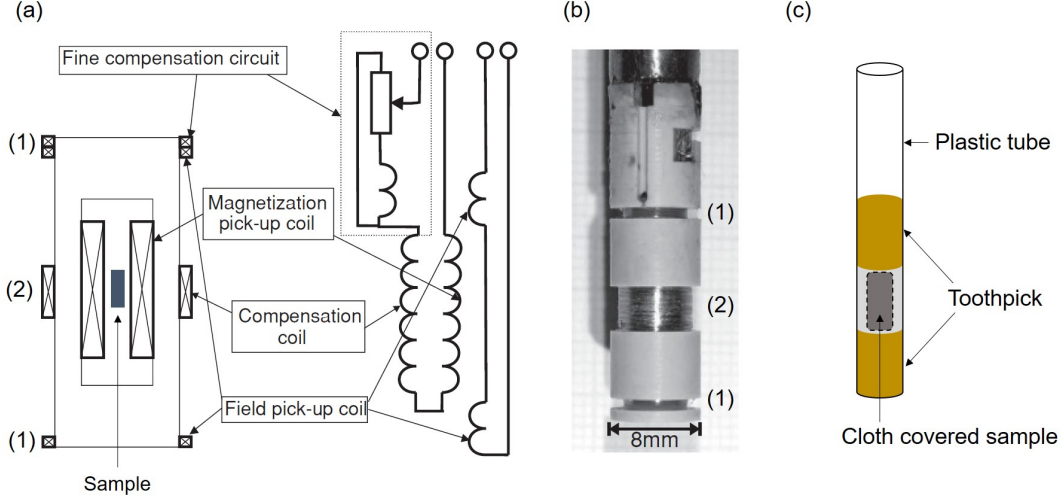


**Figure 3.3:** Pulsed-field magnetometer at HLD-EMFL. (a) Schematic of the pick-up coil system. (b) Picture of the setup. (c) Schematic of the sample holder [Sko11].

### 3.3.2 Magnetic resonance

As given in reference [Sto06], the position of the FMR line is a function of the size and direction of the applied magnetic field. Therefore, measuring the angular dependence of FMR can give information on internal magnetic fields and magnetic interactions [Kit06]. FMR is based on the resonant absorption of electromagnetic radiation by a FM material. In our setups, the resonances can be measured in the microwave range between 100 MHz and 40 GHz. In the classical picture, at resonance, the magnetization  $\mathbf{M}$  precesses around the effective magnetic field  $\mathbf{B}_{\text{eff}}$ , which is a superposition of the external magnetic field  $\mathbf{B}_{\text{ext}}$  and the internal field of the sample.

The following section gives an overview on magnetic resonance. A more detailed description can be found in references [Von66, Poo83, Mec97].

The resonance condition is fulfilled when,

$$\omega = \gamma B_{\text{eff}} \quad ; \quad \gamma = \frac{g\mu_B}{\hbar}, \quad (3.2)$$

where  $\omega$  is the resonance frequency and  $\gamma$  is the gyromagnetic ratio [Kit06].  $\gamma$  depends on the Landé  $g$ -factor,  $\mu_B$  and the reduced Planck constant  $\hbar$ . In our FMR measurements, we keep  $\omega$  constant and vary  $\mathbf{B}_{\text{eff}}$ .

The precession of  $\mathbf{M}$  can be described by the Landau-Lifshitz-Gilbert (LLG) equation [Lan35, Gil04]

$$\frac{\partial \mathbf{M}}{\partial t} = -\gamma (\mathbf{M} \times \mathbf{B}_{\text{eff}}) + \frac{\alpha}{M} \left( \mathbf{M} \times \frac{\partial \mathbf{M}}{\partial t} \right). \quad (3.3)$$

The first term on the right describes the undamped precession, while the second term describes the damping of the precession with the damping-term  $\alpha = \lambda/(\gamma M)$ , where  $\lambda$  is the relaxation frequency.

$\mathbf{B}_{\text{eff}}$  of the sample is a combination of the external field and the different contributions from the internal field arising from shape and magneto-crystalline anisotropies [Kag88]. The different contributions can be considered with the free energy density function  $F(\mathbf{M}, \mathbf{B})$  [Hel94, Kit06], given as

$$dF = \mathbf{B}_{\text{eff}} \cdot d\mathbf{M}. \quad (3.4)$$

The perturbation series of equation (3.3) gives the resonance condition [Skr66, Smi55]

$$\left( \frac{\omega}{\gamma} \right)^2 = \frac{1 + \alpha^2}{M^2 \sin^2(\theta)} \left[ \frac{\partial^2 F}{\partial \theta^2} \cdot \frac{\partial^2 F}{\partial \phi^2} - \left( \frac{\partial^2 F}{\partial \theta \partial \phi} \right)^2 \right], \quad (3.5)$$

where  $\theta$  and  $\phi$  are the polar and azimuth angles of the position of equilibrium of the magnetization vector  $\mathbf{M}$ . At resonance (eq. (3.5)), the boundary conditions

$$\frac{\partial F}{\partial \theta} = 0 \quad \text{and} \quad \frac{\partial F}{\partial \phi} = 0, \quad (3.6)$$

must be fulfilled. For the systems used in this work we take  $F(\mathbf{M}, \mathbf{B})$  as,

$$F(\mathbf{M}, \mathbf{B}) = \frac{1}{4} K_4 (\alpha_1^2 \alpha_2^2 + \alpha_1^2 \alpha_3^2 + \alpha_2^2 \alpha_3^2) + \frac{1}{2} \mu_0 \mathbf{M} \cdot \underline{\underline{N}} \cdot \mathbf{M} - \mathbf{M} \cdot \mathbf{B}. \quad (3.7)$$

The first term on the right is related to the contribution of the magneto-crystalline anisotropy energy (MCAE) with the cubic anisotropy constant  $K_4$  and the direction cosines  $\alpha_i$  [Kit06]. The second term describes the anisotropic energy density due to the reduced dimension of the sample that leads to a demagnetizing field described by the demagnetization-tensor  $\underline{\underline{N}}$ . In our studies, the shape of the sample can be approximated by a spheroid [Zin16]. The last term is the Zeeman energy [Skr66].

Angular dependent FMR is a direct measurement of the free energy density surface [Pri82]. An example is given in reference [Lin08].

$\mathbf{M}$  and  $\mathbf{B}_{\text{eff}}$  can be described by static and dynamic contributions as

$$\mathbf{M} = \mathbf{M}_S + \mathbf{m} \cdot e^{i\omega t} \quad (3.8)$$

and

$$\mathbf{B}_{\text{eff}} = \begin{pmatrix} b \cdot e^{i\omega t} \\ 0 \\ B_{\text{ext}} \end{pmatrix} + \begin{pmatrix} F_{M_x} \\ F_{M_y} \\ F_{M_z} \end{pmatrix} \quad ; \quad F_{M_i} = \frac{\partial F}{\partial M_i}. \quad (3.9)$$

Here  $b \cdot e^{i\omega t}$  is the high-frequency magnetic field of the microwave,  $F_{M_i}$  are the components of  $B_{\text{eff}}$  and  $\mathbf{m} \cdot e^{i\omega t}$  is the dynamic component of the precessing magnetization. The high-frequency susceptibility tensor  $\underline{\underline{\chi}}$  describes thereby the response of  $\mathbf{m}$  on the dynamic component of the magnetic field  $\mathbf{b}$

$$\mathbf{m} = \underline{\underline{\chi}} \mathbf{b}. \quad (3.10)$$

Eqs. (3.8) and (3.9) can be used in the LLG equation (3.3) and can be rewritten as (3.10) by linear approximation. A detailed description is given in [Mec97]. The use of a linear polarized microwave reduces the components of the  $\chi$ -tensor that have to be considered to the  $\chi_{xx}$  component.  $\chi_{xx}$  is complex, whereby the imaginary part  $\chi''_{xx}$  is proportional to the energy absorption of the high-frequency field of the microwave of the FM sample.

With our setup we are able to measure small differences in the resonance field by modulating  $B_{\text{ext}}$  and using a lock-in amplifier. The absorption due to the FM material is directly proportional to the field-derivative of  $\chi''_{xx}$ , so that

$$\frac{\partial(\text{FMR}_{\text{abs}})}{\partial B} \propto \frac{\partial \chi''_{xx}}{\partial B}. \quad (3.11)$$

### The FMR setup for external fields up to 1.6 T

A microwave resonator can be used to measure the energy absorption of the high-frequency field of the microwave. Fig. 3.4 shows schematically a microwave resonator placed between the poles of an electromagnet generating a maximum field of 1.6 T. The high-frequency magnetic field of the microwave  $b e^{i\omega t}$  is perpendicular to  $B_{\text{ext}}$  in the region of the sample, and the absorption leads to a precession of  $M$  around  $B_{\text{eff}}$  (see inset).

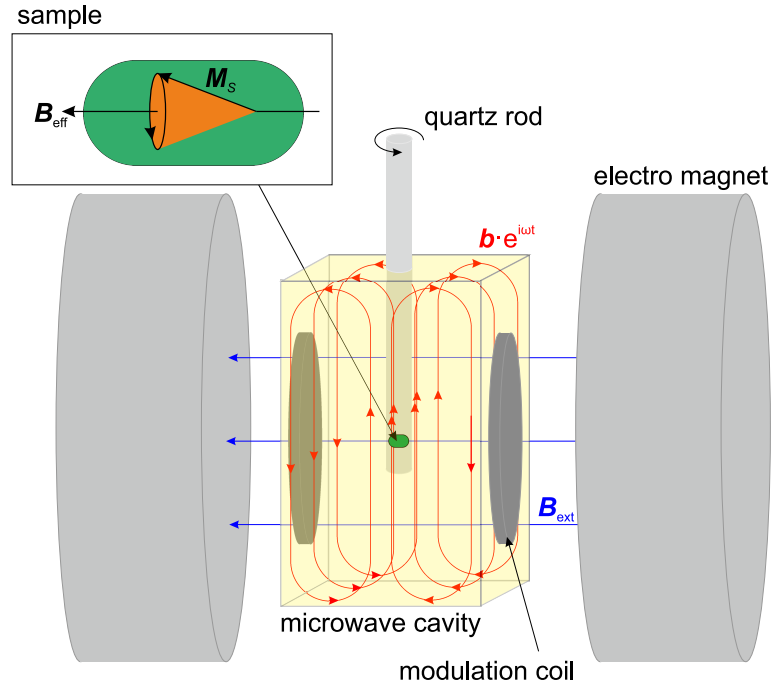


**Figure 3.4:** Schematic of FMR in a microwave cavity placed between the poles of an electromagnet with field  $B_{\text{ext}}$ . The field-modulation is done by modulation coils. The high-frequency field ( $b e^{i\omega t}$ ) of the microwave is perpendicular to  $B_{\text{ext}}$  in the range of the sample which leads to a precession of the magnetization  $M_S$  (upper left box).

FMR measurements on the  $\text{Mn}_3\text{GaC}$  single crystal discussed in chap. 4.2.2 are carried out in a Varian TE102 rectangular cavity. The microwave is generated by an X-Band klystron. A temperature-controlled nitrogen flow quartz-inset is incorporated into the cavity for temperature-dependent studies between 100 and 800 K. In combination with the quartz-inset, the cavity has an eigenfrequency of 9.238 GHz. The sample is placed into the nitrogen flow and can be rotated by a goniometer with an angular resolution of  $0.5^\circ$  [Mec97].  $B_{\text{ext}}$  is superimposed on the field of the modulation coils. In the present studies, we use a maximum field-amplitude of 1.5 mT and a frequency of 100 kHz.





respect to a unit without a tuner. The microwave absorption derivative is detected by a Schottky diode and is analyzed by a lock-in amplifier. The magnetic field  $\mathbf{B}$  is swept at a rate of  $1 \text{ mTs}^{-1}$ . A field-modulation coil around the sample-holder generates the modulation of  $\mathbf{B}$ . Two different sample-holders allow the sample to be mounted parallel or perpendicular to  $\mathbf{B}$ . Fig. 3.5(c) shows the actual mounted sample. In this case, the longitudinal axis of the sample is parallel to  $\mathbf{B}$ . The sample-temperature is measured by a sensor at the bottom of the sample-holder, and the temperature is controlled by the He gas-flow which is regulated by a heater and a capacitive temperature sensor at the bottom of the cryostat. The setup enables also multiple frequency FMR studies. A detailed description of the setup can be found in reference [Rie14].

#### Simulation of angular dependent FMR

The MCAE density of  $\text{Mn}_3\text{GaC}$  can be determined by comparing the results of angular dependent FMR measurements on the  $\text{Mn}_3\text{GaC}$  single crystal discussed in chap. 4.2.2 with simulations based on a general analytical solution of the LLG equation (eq. (3.3)). For the calculation of MCAE, the sample should be oriented with a crystal edge along the x, y, or z-axis of the coordinate system of the experimental setup in order to solve the LLG equation. In the case when the sample is mounted with the axis off this directions, the solution of the LLG equation has to be linearized for each orientation to obtain an analytic solution. However, simulations eliminate the necessity for linearization by employing  $\underline{\underline{\chi}}$  in its Jacobian matrix form (eq. (9) in [Zin17])

$$\underline{\underline{\chi}} = - \left( \left( \underline{\underline{J}}_{\mathbf{m}} \right)^{-1} \cdot \underline{\underline{J}}_{\mathbf{b}} \right), \quad (3.12)$$

where  $\underline{\underline{J}}_{\mathbf{m}}$  and  $\underline{\underline{J}}_{\mathbf{b}}$  are the Jacobian matrices in magnetization  $\mathbf{m}$  and microwave magnetic field  $\mathbf{b}$ , respectively [Zin16, Zin17]. The field-derivative of the projection of  $\underline{\underline{\chi}}$  in the direction of  $\mathbf{m}$  and  $\mathbf{b}$  is proportional to the field-derivative of the FMR absorption and can be written as

$$\frac{\partial(\text{FMR}_{\text{abs}})}{\partial B} \propto \frac{\partial \hat{e}_{\phi}^{\mathbf{M}} \cdot \underline{\underline{\chi}} \cdot \hat{e}_{\phi}^{\mathbf{B}}}{\partial B}. \quad (3.13)$$

The advantage of this non-linearized projection of  $\underline{\underline{\chi}}$  is that all possible excitations are included in the calculation of the spectra, and the complete signal of the angular dependent FMR can be simulated [Zin16, Zin17].

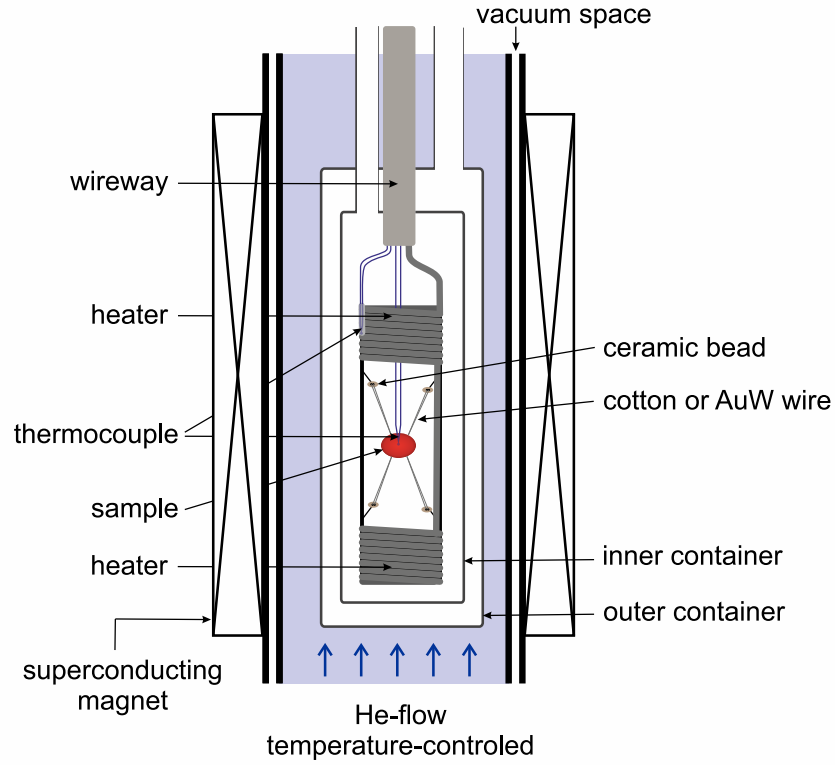
### 3.4 Adiabatic magneto-calorimeter

To study the dynamics of the MCE at first-order magnetostructural transitions,  $\Delta T_{\text{ad}}$  measurements were performed using different field-sweep rates. The field and the time dependence of  $\Delta T_{\text{ad}}$  for the rates  $11 \text{ mTs}^{-1}$  (slow),  $700 \text{ mTs}^{-1}$  (medium),  $20 \text{ Ts}^{-1}$  (fast) and  $\sim 1 \text{ kTs}^{-1}$  (very fast) are compared. The following section describes the setup and the data analysis for the different rates. The  $\Delta T_{\text{ad}}$  measurements with a slow rate of  $11 \text{ mTs}^{-1}$  were performed at our laboratories. The measurements with the rate of  $700 \text{ mTs}^{-1}$  are done at the Institute of Functional Materials at the Technical University of Darmstadt. The fast rate ( $20 \text{ Ts}^{-1}$ ) is used in the setup at the University of Parma in the Department of Mathematical, Physical and Computer sciences. The measurements in pulsed magnetic field with very fast rates of  $\sim 1 \text{ kTs}^{-1}$  are done at the HLD-EMFL.

#### Slow field-sweep rate ( $11 \text{ mTs}^{-1}$ )

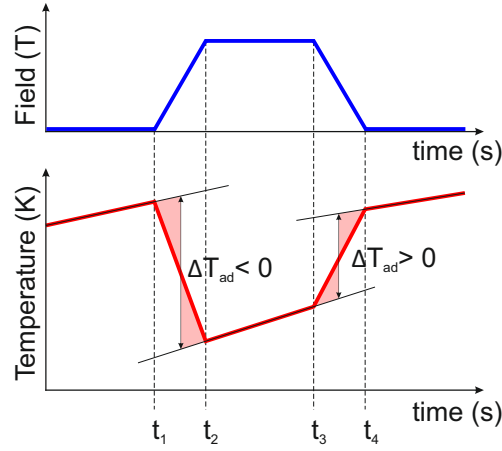
A calorimeter was designed for measuring directly  $\Delta T_{\text{ad}}$  when a magnetic field up to 5 T is applied or removed. This calorimeter operating in the temperature range  $100 < T < 750 \text{ K}$  and is based on a similar design of an existing calorimeter [Aks10, Tit12] operating in the range  $5 \leq T \leq 290 \text{ K}$ . Both setups can be placed into a helium cryostat with a superconducting magnet. The magnetic field can be continuously varied in the range  $-5 \leq B \leq 5 \text{ T}$  with a field-sweep rate of  $11 \text{ mTs}^{-1}$ .

Fig. 3.6 shows a schematic drawing of the high-temperature adiabatic magneto-calorimeter inserted into the helium cryostat. The sample is hung using silk thread or tungsten wire depending on the temperature-range of the measurements. The wires are electrically and thermally insulated with ceramic beads. The temperature of the sample is measured with a chromel/constantan thermocouple. The cylindrical design of the double bifilar heater enables a homogeneous temperature at the sample area. A Lakeshore TG-120-P controls the power to the heater up to 22 W, and the temperature of the heater is measured with a further thermocouple which also acts as the sensor for the temperature control. The inner container houses the heater and the sample. The outer container can be filled with He-gas or pumped down to about  $1 \times 10^{-5} \text{ mbar}$  thereby, enabling or preventing heat exchange between the sample and the He-flow of the cryostat. During the measurement, the inner and outer containers are evacuated to attain adiabatic conditions. For changing the temperature of the sample between 100 and 290 K, both containers are filled with He-gas, and the temperature of the He-flow and the heater are adjusted to the new temperature. To change the temperature above 290 K, the outer container has to be evacuated, and only the inner container is filled with He-gas. The temperature of the He-flow is set to the maximum value of 290 K, and the temperature of the heater is adjusted to the new temperature. After the system reaches thermal equilibrium, the heater is switched off when both containers are evacuated.



**Figure 3.6:** Schematic drawing of the high-temperature adiabatic magneto-calorimeter for  $\Delta T_{\text{ad}}$  measurements with slow field-sweep rate  $11 \text{ mTs}^{-1}$  inserted into a helium cryostat with a superconducting magnet (5 T).

During the experiment, the field and the temperature are read out while a program controls the field-sweep. Fig. 3.7 shows schematically the time dependence of the sample-temperature and the magnetic field during the measurement. The waiting period before and after a field-sweep is necessary to account for the non-adiabatic contributions to the temperature change. To calculate  $\Delta T_{\text{ad}}$ , the temperature drift during the waiting times  $t < t_1$ ,  $t_2 < t < t_3$ , and  $t > t_4$  are linearly extrapolated. The average time in the range of temperature change corresponds to the time where the shaded areas are equal. The intersection with the linear extrapolation at this average time is  $\Delta T_{\text{ad}}$ .



**Figure 3.7:** Schematic time dependence of the magnetic field, the sample-temperature and the determination of  $\Delta T_{\text{ad}}$  considering the example of an inverse magnetocaloric sample

### Medium field-sweep rate ( $700 \text{ mTs}^{-1}$ )

The  $\Delta T_{\text{ad}}$  measurements for moderate field-sweep rates ( $\sim 700 \text{ mTs}^{-1}$ ) are performed in a setup which is implemented into two nested Halbach magnets [Got16a, Got12]. The magnets rotate against each other and therefore generate a sinusoidal magnetic field profile. The maximum field of 1.93 T can be applied with a field-sweep rate of  $700 \text{ mTs}^{-1}$ .  $\Delta T_{\text{ad}}$  is directly measured by a differential T-type thermocouple mounted between two sample-plates and is fixed with a silver-based epoxy (fig. 3.8 (a)). The wires of the thermocouple are twisted to avoid induction signals. One of the ends of the differential thermocouple is fixed close to the sample at the sample holder (fig. 3.8 (b)) and the other end is referenced to ice water. To ensure adiabatic conditions, the sample holder is mounted into a vacuum tube and additionally wrapped with insulating wool. The temperature is controlled by a resistive heater next to the sample.

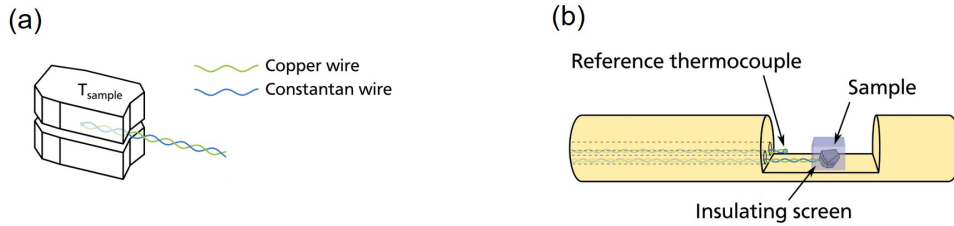


**Figure 3.8:** (a) Sample-plates with thermocouple in between. (b) Schematic of the sample holder of the  $\Delta T_{\text{ad}}$ -measurement setup with medium field-sweep rate ( $700 \text{ mTs}^{-1}$ ).  $\Delta T_{\text{ad}}$  is measured with a differential thermocouple (fig. 3.8 [Got16a]).

### Fast field-sweep rate ( $20 \text{ Ts}^{-1}$ )

This setup consists of an electromagnet and a cryostat which contains a pneumatic movable sample probe. The device is described in detailed in [Por13].  $\Delta T_{\text{ad}}$  can be measured by turning on and off the magnetic field while the sample is static or by mechanically moving the sample with a pneumatic driven holder into a static field. The low inductive electromagnet reaches a maximum field of  $2.02 \pm 0.005 \text{ T}$  with a field-sweep rate of  $2 \text{ Ts}^{-1}$ . The pneumatic cylinder drives the sample into the static field in 100 ms giving a field-sweep rate of  $20 \text{ Ts}^{-1}$ . This rate is within the range of the time response of the temperature sensor. Fig. 3.9 (a) show the pneumatic movable sample probe placed in a vacuum chamber ( $1 \times 10^{-4} \text{ mbar}$ ) at the bottom of the probe stick. The stick is connected to the pneumatic cylinder which moves the sample inside the cryostat placed between the poles of the electromagnet. The sample is glued with thermo-conductive paste on top of a Cernox bare chip (fig. 3.9 (b)) to measure the temperature of the sample. The chip has a time response of 0.135 s. Fig. 3.9 (c) shows a schematic side view of the sample holder with a sample placed on top of the Cernox bare chip. The sample-temperature is controlled by nitrogen gas-flow. After thermal equilibrium is reached, the probe is pumped, and the  $\Delta T_{\text{ad}}$  measurement is performed.  $\Delta T_{\text{ad}}$  is calculated from temperature change during the magnetic field change. The static magnetic field is subsequently measured with a Hall probe, and the field profile is determined by the detection of the induced voltage in a pickup coil.

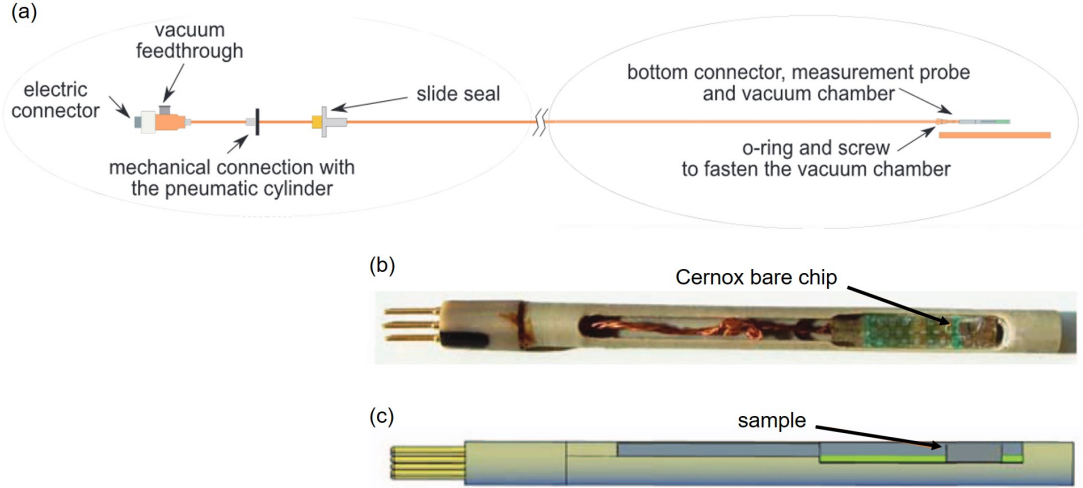


**Figure 3.9:** (a) Schematic of the measurements probe of the  $\Delta T_{\text{ad}}$ -measurement setup with fast field-sweep rate ( $20 \text{ Ts}^{-1}$ ). (b)  $\Delta T_{\text{ad}}$ -measurement probe with Cernox bare chip. (c) Sketch of the side view of the measurement probe. Fig. 1 and 2 [Por13]

### Very fast field-sweep rate ( $\sim 1 \text{ kTs}^{-1}$ )

The  $\Delta T_{\text{ad}}$  measurements in pulsed magnetic fields reaches a field-sweep rate up to  $1500 \text{ Ts}^{-1}$ . A magnetic field pulse is generated by a solenoid with a pulse duration of 150 ms, and the field can be varied up to 70 T [Sch15, Got16c, GZ15, Set16]. Due to the constant duration of the pulse, the field-sweep rate increases with increasing maximum magnetic field. Fig. 3.10 shows the pulse profile of a 2, 5, 7, 10 and 12 T pulse. The corresponding field-sweep rate as a function of field is shown in the inset of fig. 3.10.

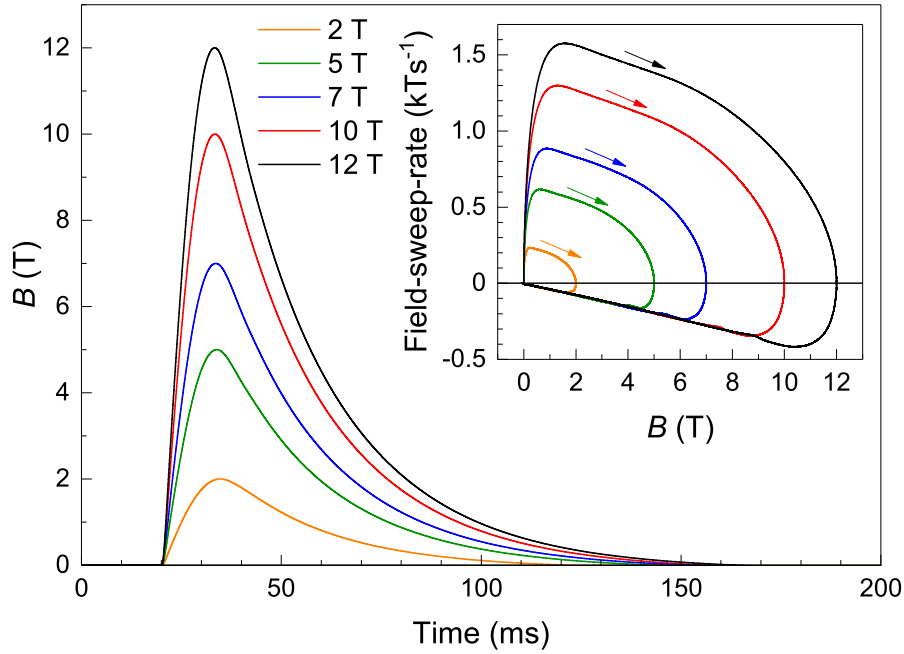


**Figure 3.10:** Profile of a 2, 5, 7, 10 and 12 T magnetic field pulses. The corresponding field-sweep rate as a function of field is shown in the inset.

Fig. 3.11 (a) shows schematically the sample holder which is located in the bore of the solenoid. The absolute temperature is measured with a PT 100 sensor and  $\Delta T_{\text{ad}}$  of the sample is measured with a differential T-type thermocouple. To ensure a fast response of the thermocouple,  $25 \mu\text{m}$  Cu and constantan wires are used. Due to the large resistivity of the thin constantan wires, the differential thermocouple is prepared in a Y-shape (shown in fig. 3.11 (b)) to minimize the length of the constantan wire. Due to this Y-shape, it is possible to build a differential thermocouple with a total resistivity of about  $190 \Omega$ . One thermocouple is glued with silver-based epoxy

between two sample plates, while the reference is fixed at the holder close to the sample. The pickup coils at the bottom of the sample holder enable the measurement of the magnetic field by integrating the induction in the coils over time. To get absolute values of the magnetic field, the signal is normalized using reference measurements of the solenoid. The temperature is controlled by a coil resistance-heater which covers the sample holder. Induction signals in the  $\Delta T_{\text{ad}}$  signal can be subtracted by a reference measurement far below the transition temperature.

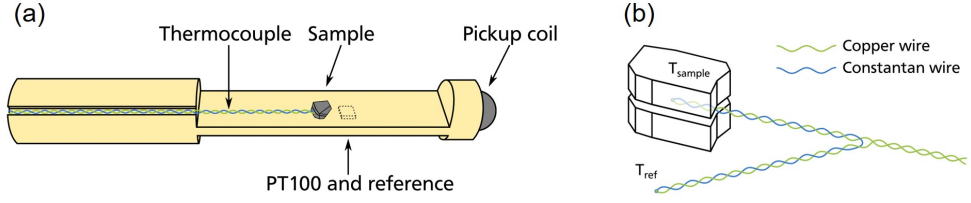


**Figure 3.11:** (a) Schematic of the sample holder of the  $\Delta T_{\text{ad}}$  measurements with very fast field-sweep rate (up to  $1.5 \text{ kTs}^{-1}$ ). (b) Sample-preparation of the Y-shape differential thermocouple. Fig. 3.10 and 3.9 [Got16a]



## 4 Results and discussion

This chapter presents the results and discussions of the experimental analysis and simulations. The chapter is divided in four sections. Section 4.1 present the magnetic and thermodynamic studies on  $\text{Mn}_3\text{GaC}$ . The measurements are done to compare the isothermal and adiabatic magnetization in the vicinity of the first-order transition. Furthermore,  $\Delta T_{ad}$  measurements on different field-sweep rates are performed to study the transition dynamics. Section 4.2 gives details on the magnetic and structural characterization of a  $\text{Mn}_3\text{GaC}$  single crystal. FMR analysis and simulations are done to determine the magnetocrystalline anisotropy-energy. The section compares also the magnetic behavior of single crystal and polycrystalline  $\text{Mn}_3\text{GaC}$  particularly around the first-order transition. Section 4.3 presents the results on magnetic and thermodynamic studies on Cr and Co-doped  $\text{Mn}_2\text{Sb}$ . Similar to the investigations on  $\text{Mn}_3\text{GaC}$ , the  $\Delta T_{ad}$  measurements at different field-sweep rates are performed to study the transition dynamics. The last section present the magnetic characterization of nano-precipitates in decomposed off-stoichiometric Ni-Mn-In Heusler alloy.

### 4.1 Transition dynamics of $\text{Mn}_3\text{GaC}$ at different time-scales

Antiperovskite  $\text{Mn}_3\text{GaC}$  is a material exhibiting a first-order AF/FM transition with narrow thermal hysteresis and a sufficiently large shift of the transition temperature  $T_i$  promising a reversible transformation in small fields up to 2 T [Toh03, Ç12, Sch15]. Previous studies show a reversible  $\Delta T_{ad}$  of 2.8 K in 3 T at a field-sweep rate of  $11 \text{ mTs}^{-1}$  [Ç12]. Using such material in cooling devices requires that the transformation of the material from one state to the other can follow the field-sweep rate of the device. The operating frequency of magnetic regenerators is at the moment 1-10 Hz. In combination with a permanent magnet of 2 T, a field-sweep rate of  $2 - 20 \text{ Ts}^{-1}$  can be achieved [Yu10, Loz14]. The MCE at the first-order transition in  $\text{Mn}_3\text{GaC}$  is based on a nucleation and growth process of domains of the new phase [Cas04, Ç14b] so that the dynamics of this process can limit the operating frequency of the regenerators. Therefore, an investigation of  $\Delta T_{ad}$  over a broad range ( $10 \text{ mTs}^{-1}$  to  $1 \text{ kTs}^{-1}$ ) of field-sweep rates is required to study the time dependence of the MCE at the first-order transition. The following section presents direct  $\Delta T_{ad}$  studies performed at slow ( $11 \text{ mTs}^{-1}$ ), medium ( $700 \text{ mTs}^{-1}$ ), fast ( $20 \text{ Ts}^{-1}$ ) and very fast ( $\sim 1 \text{ kTs}^{-1}$ ) field-sweep rates. The measurements are presented in chap. 4.1.2, 4.1.3, 4.1.4 and 4.1.5, respectively. For consistency, all measurements are carried out on the same sample except the one

for  $20 \text{ Ts}^{-1}$  (chap. 3.1). The magnetization measurements in section 4.1.1 and the  $\Delta T_{ad}$  studies with field-sweep rates of  $11 \text{ mTs}^{-1}$ ,  $700 \text{ mTs}^{-1}$  and  $\sim 1 \text{ kTs}^{-1}$  are made on sample  $\text{Mn}_3\text{GaC}$  1, and the  $\Delta T_{ad}$  studies with  $20 \text{ Ts}^{-1}$  are performed on sample  $\text{Mn}_3\text{GaC}$  2. A comparison of the studies with different field-sweep rates is given in chap. 4.1.6. In addition to the  $\Delta T_{ad}$  studies, a comparison of the magnetic behavior of  $\text{Mn}_3\text{GaC}$  under isothermal and adiabatic conditions in the vicinity of the first-order transition is able to estimate  $\Delta T_{ad}$ , the results are shown in section 4.1.1.

#### 4.1.1 Isothermal and adiabatic magnetization

In this section, the magnetization of  $\text{Mn}_3\text{GaC}$  is studied under isothermal and adiabatic conditions. The entropy change  $\Delta S_T$  of the field-induced first-order transition can be determined from the isothermal magnetization measurements. On the other hand, adiabatic magnetization measurements in pulsed fields enable the observation of the magnetization during the transformation of the material. These can be compared to  $\Delta T_{ad}$  studies. As mentioned in chap. 2.1, a coupling of the magnetic and structural subsystem is expected for materials exhibiting the inverse MCE. Therefore, the comparison of the adiabatic magnetization process and  $\Delta T_{ad}$  enables to draw conclusions about the structural subsystem.

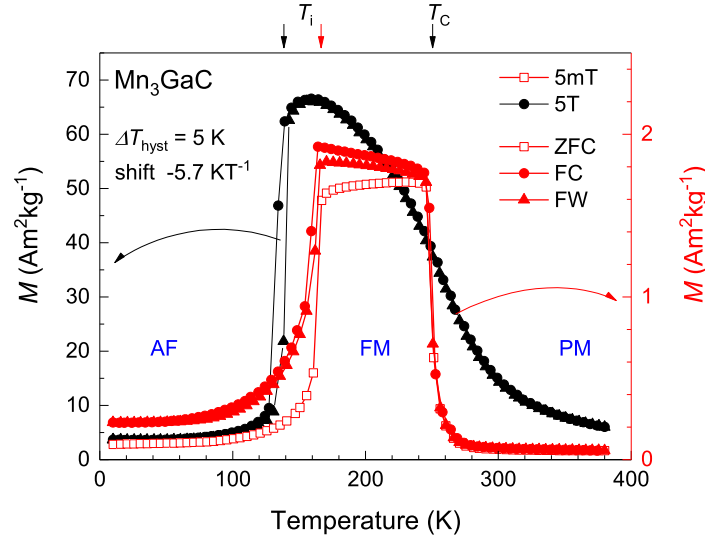


**Figure 4.1:** Temperature-dependent magnetization of  $\text{Mn}_3\text{GaC}$  powder in 5 mT (red) and 5 T (black).  $M(T)$  is measured under ZFC, FC and FW conditions. FC and FW curve show a thermal hysteresis  $\Delta T_{\text{hyst}} = 5 \text{ K}$  at the first-order transition, which can be shifted by field with a rate of  $-5.7 \text{ KT}^{-1}$  [Sch15].

Fig. 4.1 shows the temperature dependence of the magnetization  $M(T)$  of  $\text{Mn}_3\text{GaC}$  powder in the range  $10 \leq T \leq 380$  K in an external field of 5 mT (red) and 5 T (black). The magnetization is measured with the ZFC, FC, FW protocol (chap. 3.3).  $M(T)$  exhibits a first-order transition at  $T_i = 163$  K from the AF to the FM state with increasing temperature. The transition is shifted to lower temperatures with increasing measuring field at a rate of  $-5.7 \text{ K T}^{-1}$ . The thermal hysteresis  $\Delta T_{\text{hyst}}$  between the FC and the FW curves is 5 K. The background magnetization at low temperatures is due to FM impurities in the sample. The sample has a Curie temperature of  $T_C = 253$  K. The temperature of the first and second-order transition are in agreement with previous studies [Ç12, Toh03]. Small variations are due to minor deviations of the carbon concentration [Dia14].

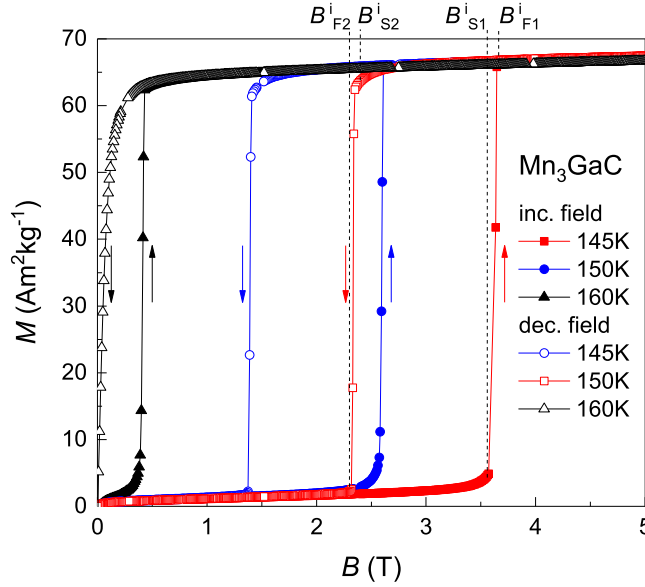


**Figure 4.2:** Field-dependent magnetization of  $\text{Mn}_3\text{GaC}$  compact sample at 145 K, 150 K and 160 K measured in increasing (full symbol) and decreasing (open symbol) field [Sch15].

Fig. 4.2 presents the isothermal field-dependent magnetization measurements  $M(B)$  in the vicinity of  $T_i$ , where the field-induced transition can be observed \*. The figure shows  $M(B)$  at 145 (red), 150 (blue) and 160 K (black) for increasing (filled symbols) and decreasing (open symbols) fields. The measurements are done on a compact  $\text{Mn}_3\text{GaC}$  1 sample. At the beginning of the measurements, the sample is in the AF state, for all temperatures. The steep increase of the  $M(B)$ -curve with increasing filed

\*The measurements are done by Dr. Tino Gottschall at the Technical University of Darmstadt.

corresponds to the transformation from the AF to the FM state. The critical field value  $B_{S1}^i$  is marked in the 145 K-curve as an example. The AF/FM transformation finishes at  $B_{F1}^i$ , where the  $M(B)$ -curve shows a saturation. For decreasing field, the reverse transformation from the FM to the AF phase starts at the critical field  $B_{S2}^i$ . This value is 1.1 T lower than  $B_{S1}^i$  due to the hysteresis at the first-order magnetostructural transition. The reverse transformation is finished at  $B_{F2}^i$ , where  $M(B)$  is almost zero. The critical fields decrease with increasing temperature. At 160 K, a reverse FM/AF transformation cannot be observed, since the sample remains in the FM phase when the field is decreased. The decrease in  $M(B)$  is, in this case, the decrease in magnetization in the FM phase.

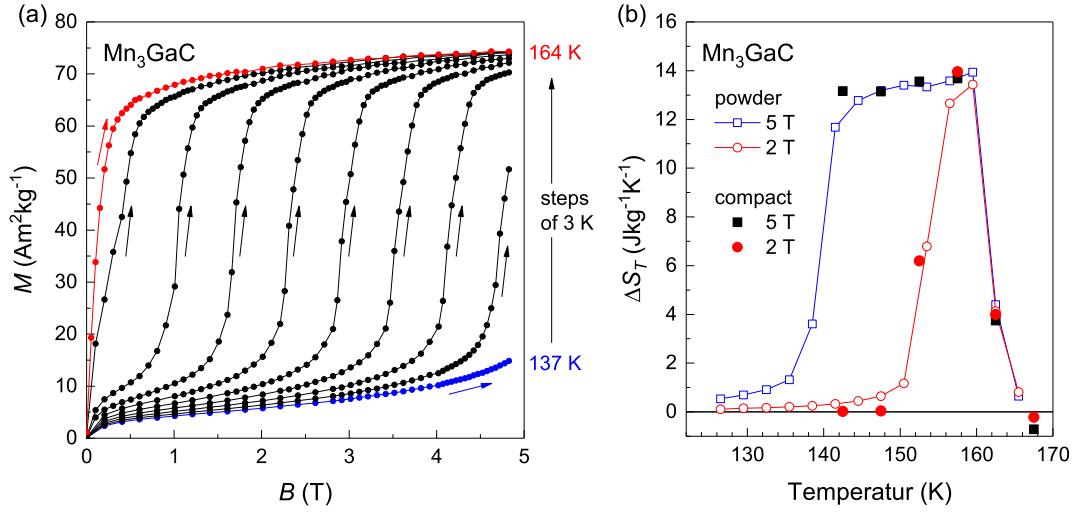


**Figure 4.3:** (a) Field-dependent magnetization of  $\text{Mn}_3\text{GaC}$  powder in the range  $137 \leq T \leq 164$  K measured in 3 K steps. (b) Entropy change  $\Delta S_T$  of powder and compact samples  $\text{Mn}_3\text{GaC}$  1 calculate by integrating  $M(B)$ -curves for 2 T and 5 T field.

The following  $M(B)$  measurements are done on a powder form of sample  $\text{Mn}_3\text{GaC}$  1 to compare  $M(B)$  and  $\Delta S_T$  with the measurements on the compact sample to investigate the effect of sample-morphology. Fig. 4.3(a) shows a series of  $M(B)$ -curves between 137 K (blue) and 164 K (red) with a step-size of 3 K. The plot shows  $M(B)$  for increasing field only. At 137 K, the sample is in the AF phase, and only a FM contribution as background and a linear contribution from the AF can be observed. The non-linear increase above 4.5 T indicates the start of the transformation to the FM phase. The critical field  $B_{S1}^i$  decreases with increasing temperature. At 158 K, a field of 2 T is sufficient to induce a full transformation.  $M(B)$  at 161 K shows a steeper increase

since the sample is already partially transformed to the FM state at 0 T. The increase of  $M(B)$  is at this temperature a combination of the saturation of the FM part and the field-induced transformation of the AF part. Above 163 K,  $\text{Mn}_3\text{GaC}$  is in the FM state, and the magnetization  $M(B)$  at 164 K is the initial magnetization curve. The comparison of  $B_{S1}^i$  of powder and compact (fig. 4.2) samples show that  $B_{S1}^i$  are equal, at similar temperatures. By contrast,  $B_{F1}^i$  of the powder sample is higher than  $B_{F1}^i$  in the compact sample. A much sharper increase of the  $M(B)$ -curve is seen in fig. 4.2 for the compact sample. The same effect was also observed in  $\text{La}(\text{Fe},\text{Si})_{13}$  [Was15, Lov15].

$\Delta S_T$  of powder and compact samples is calculated by integrating  $M(B)$  (eq. 2.11). Fig. 4.3(b) shows  $\Delta S_T$  as a function of temperature for applied fields of 2 (red) and 5 T (black).  $\Delta S_T$  of the powder sample is calculated from  $M(B)$  in fig. 4.3(a) and are shown with filled symbols.  $\Delta S_T$  of the compact sample is calculated from  $M(B)$  in fig. 4.2 and are shown with open symbols. For the powder, the 5 T-curve shows that in the case of a full transformation from the AF to the FM state, the maximum entropy change  $\Delta S_{T,max}$  is  $13.7 \text{ Jkg}^{-1}\text{K}^{-1}$ . A complete transformation can take place in the range  $145 \leq T \leq 160 \text{ K}$ . For lower temperatures, the transformation is not complete in 5 T, and the sample remains in a mixed AF/FM state showing a smaller  $\Delta S_T$ . At 161 K, the temperature is close to  $T_i$ , and the sample is in a mixed AF/FM state at the start of the measurement leading to a lower  $\Delta S_T$ . Above  $T_i$ , the sample is in the FM state showing a conventional MCE with negative  $\Delta S_T$ . The same effects are observed in 2 T, whereby the entropy change  $\Delta S_{T,max} = 13.7 \text{ Jkg}^{-1}\text{K}^{-1}$  of the full transformation is also reached at 160 K.  $\Delta S_{T,max} = 13.7 \text{ Jkg}^{-1}\text{K}^{-1}$  is comparable to  $\Delta S_{T,max} = 15 \text{ Jkg}^{-1}\text{K}^{-1}$  obtained in previous studies [Toh03, Ç12, Dia14].  $\Delta S_T$  of the compact sample exhibits the same  $\Delta S_{T,max}$  of  $13.7 \text{ Jkg}^{-1}\text{K}^{-1}$  as the powder sample. A difference in  $\Delta S_T(B, T)$  between powder and compact sample is only present for 145 K in 5 T. Due to the lower critical field  $B_{F1}^i$  of the compact sample, the transformation can be completed in 5 T leading to a higher  $\Delta S_T$  compared to the powder sample.  $\Delta S_T$  and the magnetization difference between AF and FM states are independent from the shape of the sample, while the critical fields  $B_{F1}^i$  and  $B_{F2}^i$  and the steepness of the transformation depend on the sample-morphology.

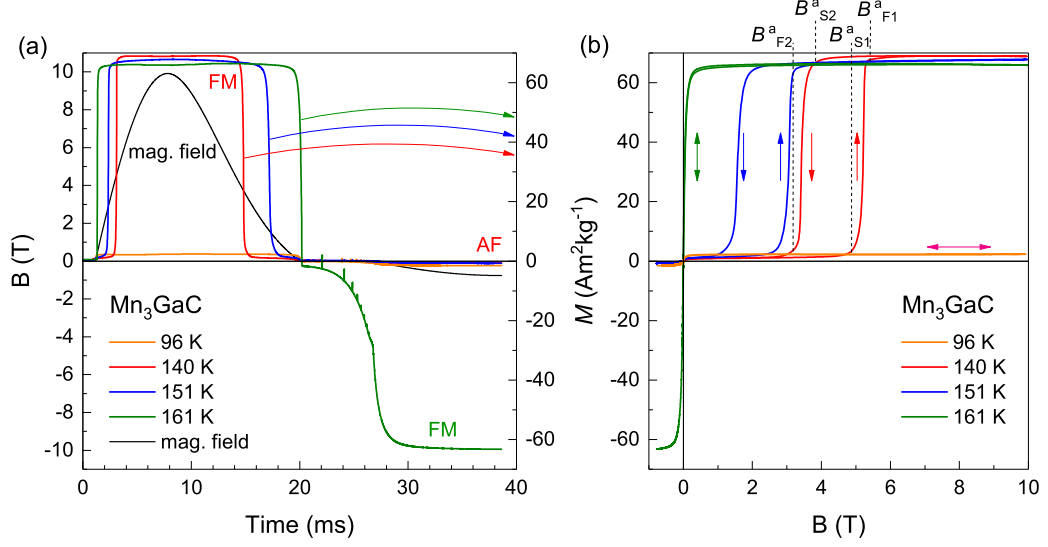


**Figure 4.4:** Magnetization of compact sample  $Mn_3GaC$  1 in pulsed magnetic field of 10 T. The profile of the magnetic pulse is shown in (a) (black, left axis) together with the time dependence of the magnetization at different temperatures (right axis). The field-dependence  $M(B)$  is shown in (b), the field-sweep direction is indicated by arrows.

We have also studied the magnetization process in the vicinity of  $T_i$  of the compact sample  $Mn_3GaC$  1 in pulsed fields. Due to the fast field-sweep rate of  $1.3 \text{ kTs}^{-1}$ , the measurements can be considered to be performed under adiabatic conditions \*. Fig. 4.4 shows the (a) time and (b) field dependencies of the magnetization at 96 (orange), 140 (red), 151 (blue) and 161 K (green). For all temperatures, a field-pulse of 10 T is applied. The critical magnetic fields of the adiabatic measurements are defined as  $B_{S1}^a$ ,  $B_{F1}^a$ ,  $B_{S2}^a$  and  $B_{F2}^a$  and are marked by dashed lines on the 140 K-curve (fig. 4.4(b)). The profile of the pulse (black) is shown in fig. 4.4(a) (left axis). The field increases after 2 ms and reaches the maximum field of 10 T in 8 ms. Afterwards, the field decreases and reaches 0 T in about 20 ms. After 20 ms, the direction of the field reverses and a field of  $-0.75 \text{ T}$  is reached at 39 ms. At 140 and 151 K, the sample is in the AF state. The applied field leads to an increase in  $M(B)$  (right axis) due to the transformation from the AF to the FM state. The saturation magnetization is about  $65 \text{ Am}^2\text{kg}^{-1}$ .  $M(B)$  decreases to zero when the field is reversed, which indicates a full reversible transformation. The negative field of  $0.75 \text{ T}$  is not sufficient to induce the transformation, and  $M(B)$  is close to zero in the negative field-range. At 161 K, the temperature is close to  $T_i$ , so that the sample is not able to transform back to the AF

\*The measurements are performed at HLD-EMFL in collaboration with Dr. Yuri Skourski.

state, and remains in the FM state when the field is reversed. This leads to a increase in  $M(B)$  in the negative field-range. At 96 K, the field of 10 T is not sufficient to induce a transformation, and the sample remains in the AF phase in the complete range of the applied field. The low background magnetization during the pulse is related to FM impurities as also observed in  $M(B)$  in fig. 4.4(b). At 140 K and 151 K, the field is large enough to induce the first-order transition so that magnetization increases after  $B_{S1}^a$  is exceeded.  $M(B)$  saturates at  $B_{F1}^a$ , indicating that the transition can follow a field-sweep rate of  $1.3 \text{ kTs}^{-1}$ . When the field is reversed, the sample starts to transform back to the AF phase at  $B_{S2}^a$  and is fully transformed at  $B_{F2}^a$ . Increasing the temperature to 151 K leads to a decrease in the critical fields. At 161 K, the magnetization increases immediately after the pulse is applied and saturates below 1 T. The FM state remains when the field is reversed and leads to a negative magnetization at negative fields.

To compare the isothermal and adiabatic magnetizations, the critical fields are plotted in fig. 4.5 as a function of temperature. The isothermal critical fields are shown as open symbols, and the adiabatic critical fields are shown as filled symbols. The linear decrease of  $B_{S1}^i$  (black),  $B_{F1}^i$  (green),  $B_{S2}^i$  (blue) and  $B_{F2}^i$  (red) is shown by the straight lines.  $B_{S1}^i$  and  $B_{F1}^i$  decrease at a rate of  $-4.8 \text{ K T}^{-1}$  while  $B_{S2}^i$  and  $B_{F2}^i$  decrease at a rate of  $-5.4 \text{ K T}^{-1}$ . The different rates lead to an increase in the width of the field-hysteresis  $\Delta B_{\text{AF/FM}}$ .  $\Delta B_{\text{AF/FM}}$  increases from 1.0 T at 155 K to 1.3 T at 140 K. A similar effect is also observed in Ni-Mn-In-Co [Got16b]. By contrast, the width of the transformation,  $\Delta B_j^i = B_{Sj}^i - B_{Fj}^i$  ( $j = 1, 2$ ), is independent of temperature. The AF to the FM transformation  $\Delta B_1^i = 0.2 \text{ T}$  is slightly narrower than the FM to the AF transformation with  $\Delta B_2 = 0.1 \text{ T}$ .

The comparison of the adiabatic measurements (filled symbols) and the isothermal measurements show that the critical fields do not coincide except for  $B_{F2}^a$ . The values of  $B_{S1}^a$  are larger by 0.4 T than those of  $B_{S1}^i$ . The increase can be explained by a super-cooling of the start of the transformation due to a slow nucleation process relative to the fast movement of the phase boundary between the AF and FM phases. A slow nucleation process was also observed in Ni-Mn-In Heusler alloys [Got16c]. This shows that the field-sweep rate plays an important role on  $B_{S1}$ .  $B_{F1}^a$  is about 0.6 T higher than  $B_{F1}^i$ , but it has to be considered that the temperature of the sample decreases by  $\Delta T_{ad}$  due to the adiabatic conditions of the measurements. Previous studies have given a  $\Delta T_{ad}$  between 3 and 5 K for  $\text{Mn}_3\text{GaC}$  [Toh03, Ç12].  $\Delta T_{ad}$  of the  $\text{Mn}_3\text{GaC}$  1 sample can be measured by the distance between  $B_{F1}^a$  and the linear fit of  $B_{F1}^i$ . The measurements at 140 K shows a  $\Delta T_{ad}$  of 3.2 K, and at 151 K, a  $\Delta T_{ad}$  of 3.9 K is measured. The values fit within the range of  $\Delta T_{ad}$  reported in the literature. Direct  $\Delta T_{ad}$  measurements on  $\text{Mn}_3\text{GaC}$  1 are given in chap. 4.1.5. The results are in agreement with the values obtained from the magnetization measurements.

To compare  $B_{S2}^a$  and  $B_{S2}^i$ , the decrease in the temperature by  $\Delta T_{ad}$  has to be considered as well. The shift of  $B_{S2}^a$  by the corresponding  $\Delta T_{ad}$  of 3.2 K (140 K)

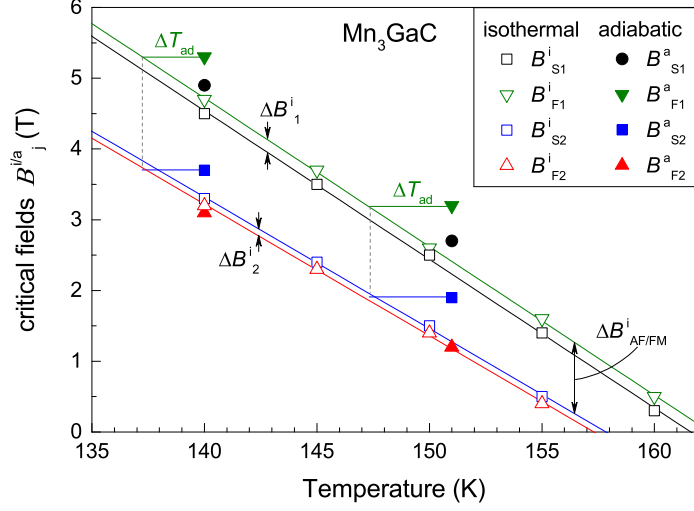


**Figure 4.5:** Critical field values  $B_{S/Fj}^{i/a}$  ( $j = 1, 2$ ) of the first-order transition of compact  $Mn_3GaC$  1 for isothermal (open) and adiabatic (filled)  $M(B)$ -curves for different temperatures, see fig. 4.2(a) and 4.4. The error bar is smaller than the size of the symbols.

and 3.9 K (151 K) is shown with the blue horizontal lines. The left end of the line corresponds to the shifted  $B_{S2}^a$ , which is lower than the linear fit to  $B_{S2}^i$ . The lower values of the shifted  $B_{S2}^a$  indicates that the FM to AF transformation also has a slow nucleation process. The effect of super-cooling is however smaller in case of the FM to AF transformation compared to the AF to FM transformation. The difference can be explained by the different field-sweep rates of the field-pulse (fig. 3.10(b), chap. 3.4). The super-cooling of  $B_{S1}^a$  and  $B_{S2}^a$  increases with increasing field-sweep rate.  $B_{F2}^a$  coincides with the linear fit to  $B_{F2}^i$ , which shows that the movement of the phase boundary between the AF and FM phases can follow the field-sweep rate for the pulse. The temperature of the sample is increased during the full reverse of the transformation by  $\Delta T_{ad}$  and is equal to the temperature before the pulse.

The comparison of critical fields in isothermal and adiabatic  $M(B)$  measurements shows that the field-sweep rate of the magnetic field influences the nucleation process of the first-order transition. However, the movement of phase boundary is independent of the field-sweep rate up to  $1.3 \text{ kTs}^{-1}$ . A  $\Delta T_{ad}$  of 3.2 K (140 K) and 3.9 K (151 K) were determined for the adiabatic  $M(B)$  measurements, which will be compared to direct adiabatic  $\Delta T_{ad}$  measurements in chapter 4.1.5.



#### 4.1.2 $\Delta T_{ad}$ at slow field-sweep rate $11 \text{ mTs}^{-1}$

This section discusses the direct  $\Delta T_{ad}$  measurements on  $\text{Mn}_3\text{GaC}$  1 carried out using a superconducting 5 T magnet with a field-sweep rate of  $11 \text{ mTs}^{-1}$ . The setup is described in chap. 3.4.  $\Delta T_{ad}$  is measured during the field-sweep between 0 T and 5 T in the temperature range  $130 \leq T \leq 170 \text{ K}$ .

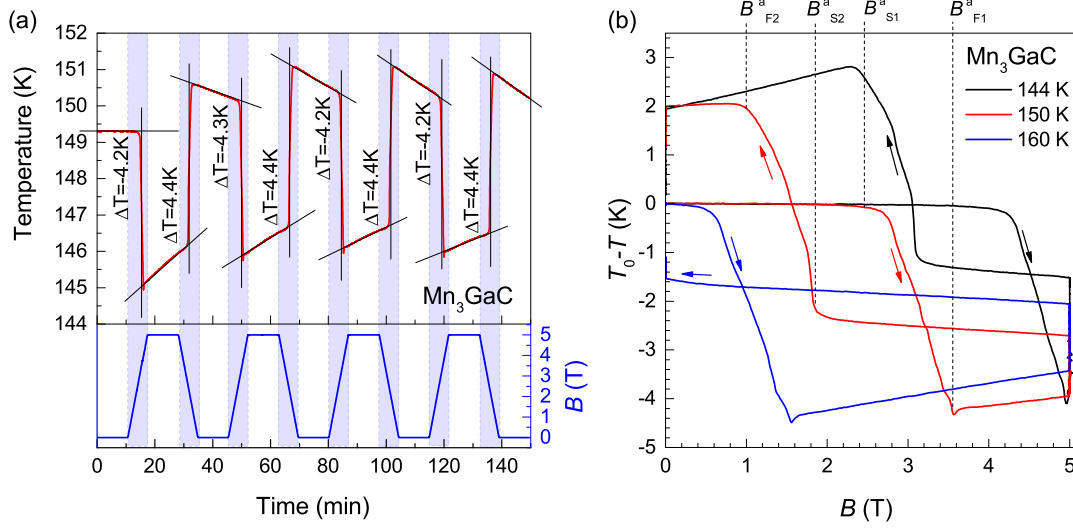


**Figure 4.6:** Direct  $\Delta T_{ad}$  measurements of compact  $\text{Mn}_3\text{GaC}$  1 performed in 5 T magnetic field with field-sweep rate of  $11 \text{ mTs}^{-1}$ . (a) shows the oscillation of the magnetic field with time (blue) and the corresponding variation of temperature (red) around 150 K. The time range with changing field are highlighted in blue.  $\Delta T_{ad}$  is shown for each field change. (b) shows the field dependence of temperature change  $T_0 - T$  for measurements around 144 K, 150 K and 160 K. The critical fields are marked for the measurement around 150 K, the field-sweep direction is indicated by arrows [Sch15].

Fig. 4.6(a) shows the temperature change around 150 K during the 5 T field-sweep as a function of time. The field-sweep from 0 to 5 T and back to 0 T is done four times. The blue curve (bottom plot) shows the profile of the magnetic field (right axis). The blue highlighted areas corresponds to the time-range where the field is changed. The red curve (left axis, upper plot) shows the temperature of the sample. The temperature shows a fast decrease and increase in the time-range where the field is changed. However, a variation of temperature is also observed in the time-range where the magnetic field is constant. This temperature-drift is related to non-adiabatic conditions.  $\Delta T_{ad}$  is calculated for each field-sweep by taking this into account (chap. 3.4). The values of  $\Delta T_{ad}$  vary between 4.2 and 4.4 K. Within an error of  $\pm 0.1 \text{ K}$ ,  $\Delta T_{ad}$

is reversible at the first-order transition. The comparison of  $|\Delta T_{ad}|$  for increasing and decreasing fields shows that  $|\Delta T_{ad}|$  for decreasing fields (4.4 K) is larger than  $|\Delta T_{ad}|$  for increasing fields (4.2 K to 4.3 K), for all field-oscillations. The difference is caused by the temperature-drift in the time-range where the field is held constant. The drift can initiate the AF/FM transformation before the field is applied so that  $\Delta T_{ad}$  reduces.

Fig. 4.6(b) shows the temperature change  $T_0 - T$  at 144 K, 150 K and 160 K as a function of field.  $T_0$  corresponds to the equilibrium temperature before the field is applied. The field-sweep direction is indicated by arrows. The critical fields are marked for the 150 K-measurement. All measurements show a decrease in  $T_0 - T$  above  $B_{S1}^a$ . Above  $B_{F1}^a$  the temperature increases caused by the conventional MCE in the FM phase and the temperature-drift due to non-adiabatic conditions. At 5 T, the temperature increases by 1 K during which the field is held constant. This is caused by non-adiabatic conditions. Reversing the field leads to a small increase in  $T$  in the range  $5 \text{ T} \geq B > B_{S2}^a$ , which is also caused by non-adiabatic conditions and the conventional MCE in the FM phase. The fast increase in  $T$  in the range  $B_{S2}^a > B > B_{F2}^a$  is due to the reverse FM/AF transformation. The slow decrease in  $T$  below  $B_{F2}^a$  is again related to non-adiabatic conditions. For the 160 K-measurement, the sample is not able to transform back to the AF state and remains in a mixed state on removing the field. For all three temperatures, a full transformation from the AF phase to the FM phase can be observed. The maximum  $T_0 - T$  slightly decreases with increasing temperature from  $-4.5 \text{ K}$  at 160 K to  $-4.0 \text{ K}$  at 144 K. The critical fields of the adiabatic measurements coincide with those of the isothermal magnetization measurements presented in chap. 4.1.1.

### 4.1.3 $\Delta T_{ad}$ at moderate field-sweep rate $700 \text{ mTs}^{-1}$

$\Delta T_{ad}$  measurements in the range  $140 \leq T \leq 170 \text{ K}$  on sample  $\text{Mn}_3\text{GaC}$  1 have also been carried out in a nested Halbach magnet setup with a field-sweep rate of  $700 \text{ mTs}^{-1}$  and a maximum field of  $2 \text{ T}$  \*. The setup is described in chap. 3.4.

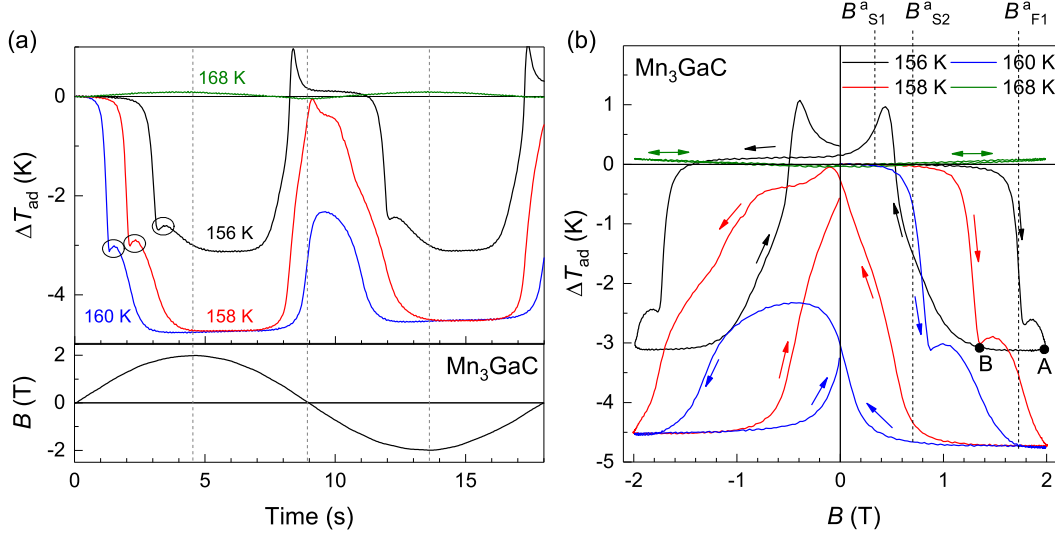


**Figure 4.7:** Direct  $\Delta T_{ad}$  measurements of compact  $\text{Mn}_3\text{GaC}$  1 performed in  $2 \text{ T}$  magnetic field with a field-sweep rate of  $700 \text{ mTs}^{-1}$ . (a) The bottom graph shows the oscillation of the magnetic field as a function of time. The top part shows the variation of  $\Delta T_{ad}$  for the start temperatures 156, 158, 160, and 168 K. The maximum, minimum, and zero field are marked with dashed lines. (b) shows the field dependence of  $\Delta T_{ad}$ , the field-sweep direction is indicated by arrows [Sch15].

Fig. 4.7 shows the measurements at 156 (black), 158 (red), 160 (blue) and 168 K (green). Fig. 4.7(a) shows the time dependence of  $\Delta T_{ad}$  in the upper panel and the magnetic field-profile in the lower panel. The magnetic field oscillates between  $2 \text{ T}$  and  $-2 \text{ T}$ . The maximum, minimum and zero field positions are indicated by dashed lines. The measurement at 168 K (green) shows a faint conventional MCE, with the sample warming and cooling in phase with the field. On increasing the field to  $2 \text{ T}$ , the measurements at 156 (black), 158 (red) and 160 K (blue) show a negative  $\Delta T_{ad}$  due to the inverse MCE. At 160 and 158 K, the sample shows a full transformation from the AF phase to the FM phase with a  $\Delta T_{ad}$  of  $-4.7 \text{ K}$ . At 156 K, a field of  $2 \text{ T}$  is not sufficient to induce a full transformation, and the sample remains in a mixed AF/FM state. The incomplete transformation results in a  $\Delta T_{ad}$  reduced to  $-3 \text{ K}$ . Reducing

\*The measurements are performed by Dr. Tino Gottschall at the Technical University of Darmstadt.

the field to zero causes  $\Delta T_{ad}$  to increase, and at 156 and 158 K, the sample returns to the AF state. At 160 K, the temperature is too close to  $T_i$  so that the sample remains in a mixed state at 0 T and  $\Delta T_{ad} \neq 0$  K. The overshoot in  $\Delta T_{ad}$  at 156 K close to 0 T is due to non-adiabatic conditions and is explained below. Reversing the field gives nearly the same  $\Delta T_{ad}$  behavior for 156 and 158 K.

Fig. 4.7(b) shows  $\Delta T_{ad}$  as a function of field. The critical fields are marked on the 160 K-curve. The field-sweep directions are indicated by arrows.  $\Delta T_{ad}$  at 168 K (green) shows a slow increase with increasing field due to the conventional MCE in the FM phase. The forward and reverse path of  $\Delta T_{ad}$  are the same. The measurements at 156 (black), 158 (red) and 160 K (blue) show a decrease of  $\Delta T_{ad}$  after  $B_{S1}^a$  is exceeded. Comparing  $B_{S1}^a$  and  $B_{S1}^i$  (fig. 4.5 in chap. 4.1.1) shows that  $B_{S1}^a$  is 0.5 T greater. On the other hand,  $B_{F1}^a = B_{F1}^i$ . This shows that at a field-sweep rate of  $700 \text{ mTs}^{-1}$ , the nucleation process in the FM phase is already too slow leading to super-cooling of  $B_{S1}^a$ . The same effect was also observed in the adiabatic  $M(B)$  measurements in pulsed fields (fig. 4.5). At 158 and 160 K, the transformation is complete at  $B_{F1}^a$  with a  $\Delta T_{ad} = -4.7$  K. At 156 K, the transformation is not complete, and the sample exhibits a mixed AF/FM state at 2 T leading to a lower  $\Delta T_{ad}$ . Decreasing the field from 2 T shows no change in  $\Delta T_{ad}$  which verifies nearly adiabatic conditions.  $\Delta T_{ad}$  increases when  $B_{S2}^a$  is exceeded. A reverse transformation to the initial AF state is only observed in measurements at 156 K leading to a symmetric  $\Delta T_{ad}$ -curve for the reverse field-direction ( $0 \leftrightarrow -2$  T). In the case of the measurements at 158 and 160 K, the sample is not fully transformed back to the initial AF state, and the  $\Delta T_{ad}$ -curve in the negative field-direction is not symmetric to the positive field-direction. The irreversibility of the transformation reduces also  $\Delta T_{ad}$  in the negative field-direction ( $-4.5$  K for 158 K and  $-2$  K for 160 K).

A positive  $\Delta T_{ad}$  at 156 K is observed in the time-range  $8 < t < 9$  s and  $17 < t < 18$  s, fig. 4.7(a), and also in the corresponding field-range  $0 \leq B < 0.8$  T and  $-0.8 < B \leq 0$  T in fig. 4.7(b). The effect can be explained by a slight increase of the temperature during the measurements due to non-adiabatic conditions. The positive  $\Delta T_{ad}$  originates from different  $\Delta T_{ad}$  for increasing and decreasing field. A  $\Delta T_{ad} = -3$  K is observed for increasing field related to the AF to FM transition. For decreasing field, a  $\Delta T_{ad} = 4$  K is observed related to the FM to AF transition. The increase in  $|\Delta T_{ad}|$  can only be explained if during the reverse transformation more FM phase is transformed to the AF phase than the FM phase being transformed from the AF phase during the forward transformation. This requires a decrease of the AF/FM ratio at the end of the forward transformation (A) and at the start of the reverse transformation (B) (see fig. 4.7(b)). The decrease of the AF/FM ratio can be explained by an increase of the temperature leading to a further transformation to the FM state. Due to the sharp transformation (fig. 4.2), a slight increase of  $0.1 \text{ K} - 0.2 \text{ K}$  is sufficient to change the AF/FM ratio. The effect is not observed at 158 K since the sample is fully transformed to the FM state at 2 T and an increase of the temperature does not change the AF/FM ratio.

Furthermore, the measurements at 156, 158 and 160 K exhibit a 0.3 K increase in the temperature during the time-range  $0 \leq t \leq 4$  s, marked by black, open circles in fig. 4.7(a). For all measurements, the increase is observed when  $\Delta T_{ad}$  reaches  $-2.5$  K to  $-3$  K. The increase can be related to an additional conventional MCE which is superimposed on the inverse MCE. An increase in temperature can only be observed if the AF/FM ratio does not change when increasing the field. In fig. 2.6, it is shown that the transformation branch cannot be left during increasing field, which means that a pause of the transformation is not possible. The increase of  $\Delta T_{ad}$  by 0.3 K can be explained by a secondary phase of  $\text{Mn}_3\text{GaC}$  with slightly lower carbon content. In this case, the carbon-deficient phase has a lower  $T_i$  than the main phase [Dia14]. The increasing field will first transform the carbon deficient phase (lower  $T_i$ ) and, second, transform the main phase (higher  $T_i$ ). It is known that carbon-deficient  $\text{Mn}_3\text{GaC}$  has a lower  $\Delta S$  than the alloy without carbon deficiencies [Dia14] assuming also a lower  $\Delta T_{ad}$  value. This matches with the  $\Delta T_{ad}$ -curves in fig. 4.7(a), where the 0.3 K increase is observed when  $\Delta T_{ad}$  reaches  $-2.5$  K to  $-3$  K. The reduced  $\Delta T_{ad}$  of about  $-2.5$  K to  $-3$  K then corresponds to the inverse MCE of the carbon-deficient phase. The subsequent increase of 0.3 K with increasing field would then correspond to the conventional MCE in the FM state. The further increase of the field induces the transition in the main  $\text{Mn}_3\text{GaC}$  phase leading to a decrease in  $\Delta T_{ad}$  to  $-4.7$  K. In this case, the two phases have a  $\Delta T_{ad}$  of about  $-3$  K and  $-4.7$  K which is in agreement with  $\Delta T_{ad}$  reported in the literature [Toh03, Ç12, Sch15]. For the reverse field-direction, the increase in the  $\Delta T_{ad}$ -curve can only be observed at 156 K, since the transformation is fully reversed.

The  $\Delta T_{ad}$  measurements at a field-sweep rate of  $700 \text{ mTs}^{-1}$  show super-cooling in  $B_{S1}^a$  due to the slow nucleation process of the first-order transition. A further comparison of the measurements with different field-sweep rates is given in chap. 4.1.6.

#### 4.1.4 $\Delta T_{ad}$ at fast field-sweep rate $20 \text{ Ts}^{-1}$

The  $\Delta T_{ad}$  measurements with a field-sweep rate of  $20 \text{ Ts}^{-1}$  in a field of 2 T are carried out in an electromagnet using a pneumatic sample-holder to move the sample in and out of the magnetic field \*. The setup is described in chap. 3.4. The measurements are performed on sample  $\text{Mn}_3\text{GaC}$  2. For this sample,  $T_i = 161 \text{ K}$  and  $T_C = 250 \text{ K}$ . Compared to sample  $\text{Mn}_3\text{GaC}$  1,  $T_i$  decreases by 2 K while  $T_C$  decreases by 3 K. These small differences can be explained by a slight variations in the carbon concentrations [Dia14].

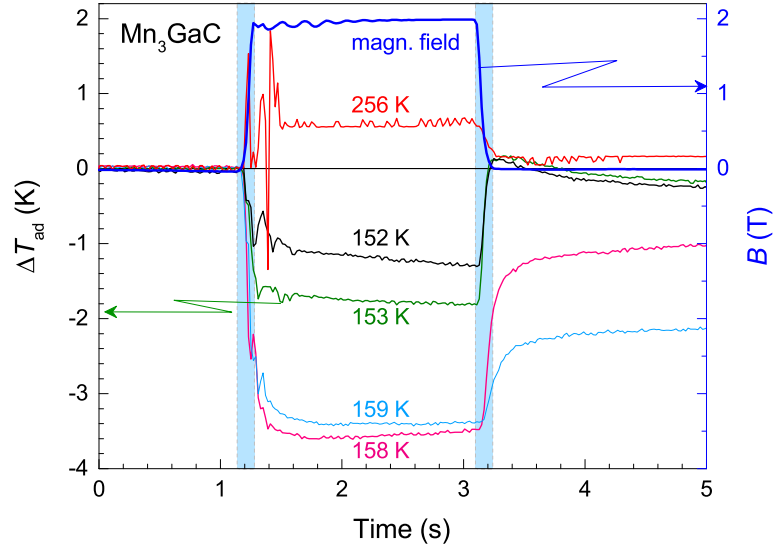


**Figure 4.8:** Direct  $\Delta T_{ad}$  measurements of compact  $\text{Mn}_3\text{GaC}$  2 performed in 2 T magnetic field with a field-sweep rate of  $20 \text{ Ts}^{-1}$ . The field profile (blue) scales with the right axis and the time range of changing field is highlighted in blue. The left axis shows the time dependence of  $\Delta T_{ad}$  for the start temperatures 152, 153, 158, 159, and 256 K.

$\Delta T_{ad}$  is measured in the temperature-range  $124 \leq T \leq 164 \text{ K}$  in the vicinity of  $T_i$  as well as at 256 K; close to  $T_C$ . Fig. 4.8 shows the time dependence of  $\Delta T_{ad}$  at 152 (black), 153 (green), 158 (pink), 159 (light blue) and 256 K (red). The field-profile (blue) is scaled on the right axis. The time-range of the field-sweep is within the range of each blue bar. During the waiting-time  $0 \leq t \leq 1.2 \text{ s}$ , no temperature change is observed. At 1.2 s, the sample enters the static field leading to a decrease of  $\Delta T_{ad}$  for

\*The measurements are performed at the University of Parma in collaboration with Dr. Francesco Cugini, Prof. Dr. Massimo Solzi and Dr. Özner Çakır.

the measurements below 160 K and an increase of  $\Delta T_{ad}$  for the measurement at 256 K. The large oscillations in the range  $1.2 \leq t \leq 1.6$  s are related to induction signals, which are generated by the mechanical vibrations of the sample-holder when the movement is halted in the field. Oscillations can also be observed in the field-profile. During the waiting-time between 1.6 and 3.1 s, nearly no change in  $\Delta T_{ad}$  is observed indicating that the conditions are adiabatic. At 3.1 s the sample is moved out of the magnetic field leading to an increase in  $\Delta T_{ad}$  for the measurements below 160 K and a decrease for the measurement at 256 K. During the waiting-time at the end of the movement, a nearly constant  $\Delta T_{ad}$  is observed for all measurements. The 256 K-curve shows a  $\Delta T_{ad}$  of 0.6 K caused by the conventional MCE. The remaining  $\Delta T_{ad}$  for  $t > 3.3$  s is caused by drift due to imperfect adiabatic conditions. At 158 and 159 K, a  $\Delta T_{ad}$  of  $-3.6$  and  $-3.4$  K is observed showing a nearly full transformation from the AF to the FM state. After the sample is moved out of the field,  $\Delta T_{ad}$  remains at  $-1.1$  and  $-2.2$  K showing that the transformation is not reversible, and the sample is then in a mixed AF/FM state at  $t > 3.3$  s. The measurements at 152 and 153 K yield a  $\Delta T_{ad}$  of  $-1.1$  and  $-1.7$  K when the field is applied. These lower values with respect to the higher temperature values show that for both temperatures the transformation from the AF to the FM state is not complete at 2 T, and the sample remains in a mixed state for  $1.5 \text{ s} < t < 3 \text{ s}$ . The subsequent decrease of the field causes the state to transform back to the AF state. At both temperatures,  $\Delta T_{ad}$  reverses back to zero, which also shows that the transformation is fully reversed, and the sample is in the AF state.

The  $\Delta T_{ad}$  measurements performed with a field-sweep rate of  $20 \text{ T s}^{-1}$  show that a nearly full transformation can be induced at 158 and 159 K in a field of 2 T. Here, the maximum  $\Delta T_{ad}$  of  $-3.6$  K is, however, smaller than the maximum  $\Delta T_{ad}$  of  $-4.7$  K observed for  $\text{Mn}_3\text{GaC}$  1 (chap. 4.1.3). It is not clear if the difference in the maximum  $\Delta T_{ad}$  is related to the different field-sweep rates or to the use of different samples.

#### 4.1.5 $\Delta T_{\text{ad}}$ in pulsed fields up to $1 \text{ kTs}^{-1}$

This chapter presents  $\Delta T_{\text{ad}}$  measurements on sample  $\text{Mn}_3\text{GaC}$  1 using field-sweep rates up to  $1 \text{ kTs}^{-1}$  with pulsed fields up to  $10 \text{ T}^*$ . The setup is described in chap. 3.4.

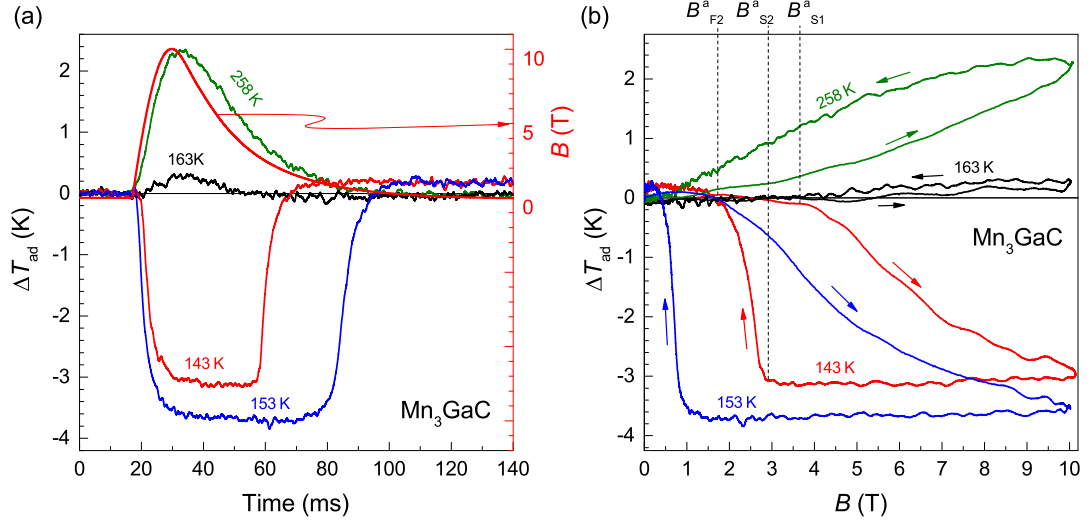


**Figure 4.9:** Direct  $\Delta T_{\text{ad}}$  measurements of  $\text{Mn}_3\text{GaC}$  1 performed in  $10 \text{ T}$  pulsed magnetic fields with field-sweep rate of about  $1 \text{ kTs}^{-1}$ . (a) Time dependence of  $\Delta T_{\text{ad}}$  (left axis) for the start temperatures 143, 153, 163, and 258 K. The magnetic pulse profile (red) is scaled with the right axis. (b) shows the field dependence of  $\Delta T_{\text{ad}}$ , the field-sweep direction is indicated by arrows [Sch15].

Fig. 4.9(a) shows the time dependence of  $\Delta T_{\text{ad}}$  at 143 (red), 153 (blue), 163 (black) and 258 K (green) and the field-profile of the magnet-field pulse (red, right axis). Fig. 4.9(b) shows  $\Delta T_{\text{ad}}$  as a function of field. The direction of the field-sweep is indicated by arrows. As shown in fig. 4.9(a) the field-pulse starts after a waiting time of 17 ms and reaches the maximum field of  $10 \text{ T}$  after 30 ms. The decrease of the field is slower than its increase, and the field reduces to  $0 \text{ T}$  at about 120 ms. For the measurement at 258 K,  $\Delta T_{\text{ad}}$  increases by 2.3 K. 258 K corresponds to the PM state and is close to  $T_C$  so that the positive  $\Delta T_{\text{ad}}$  is caused by the conventional MCE at the second-order PM/FM transition. At 163 K, the sample is in the FM state  $T_i < T < T_C$ , and the increase of  $\Delta T_{\text{ad}}$  of about 0.3 K is also related to the conventional MCE, occurring in the FM phase. The influence of eddy-current during the field-pulse has a minor effect on  $\Delta T_{\text{ad}}$ , since no measurable increase of the temperature can be observed at

\*The measurements are performed at HLD-EMFL in collaboration with Dr. Tino Gottschall, Dr. Mahdiyeh Ghorbani Zavareh and Dr. Yuri Skourski.



163 K after the field pulse. The measurements at 143 and 153 K show a negative  $\Delta T_{\text{ad}}$  of  $-3.0$  and  $-3.8$  K, respectively. This is due to the inverse MCE at the first-order transition from the AF to the FM phase. At both temperatures, the  $\Delta T_{\text{ad}}$ -curves fully reverse after the field-pulse indicating a reversible transformation.

The data taken at 258 K shows a delay of about 3 ms with respect to the field-profile caused by the thermal lag with the thermocouple. The delay can be observed as a deviation of the  $\Delta T_{\text{ad}}$ -curve for both increasing and decreasing fields in fig. 4.9(b). In the case of the first-order transformation at 143 and 153 K,  $\Delta T_{\text{ad}}$  decreases after  $B_{S1}^a$  is exceeded.  $\Delta T_{\text{ad}}$  decreases continuously until the field reaches its maximum at 10 T. A maximum  $|\Delta T_{\text{ad}}|$  of 3.0 and 3.8 K is observed for the measurements at 143 K and 153 K, respectively. The  $\Delta T_{\text{ad}}$  measurements presented in section 4.1.2 and 4.1.3 show a maximum  $|\Delta T_{\text{ad}}|$  of 4.7 K for a 5 T field change for  $\text{Mn}_3\text{GaC}$  1 in the case of a full transformation from the AF to the FM state. A field change of 10 T should therefore also be sufficient to induce the full transformation. However, measurements in fig. 4.9 show for a 10 T field change a reduced  $\Delta T_{\text{ad}}$  of  $-3.0$  and  $-3.8$  K for 143 K and 153 K, respectively. Besides this,  $B_{F1}^a$  cannot be observed in fig. 4.9(b) for 143 K and 153 K indicating that the transformation is not complete.

For decreasing field, a weak decrease in  $\Delta T_{\text{ad}}$  can be observed until  $B_{S2}^a$  is exceeded. In this range, the AF/FM ratio does not change, and the weak decrease in  $\Delta T_{\text{ad}}$  corresponds to the conventional MCE in the FM phase. This can be confirmed by the decrease in  $\Delta T_{\text{ad}}$  at 163 K showing the conventional MCE of the FM phase. The slopes of the  $\Delta T_{\text{ad}}$ -curve at 163 K and the ones at 143 K and 153 K in the range  $10 \text{ T} \geq B > B_{S2}^a$  are equal confirming the conventional MCE in this range. The further decrease of the field ( $B < B_{S2}^a$ ) leads to a fast increase of  $\Delta T_{\text{ad}}$  due to the inverse MCE of the FM to AF transformation. The reverse of  $\Delta T_{\text{ad}}$  to 0 K is reached at  $B_{F2}^a$ , indicating a full reversible transformation to the AF state.

Comparing the  $\Delta T_{\text{ad}}$ -curves for forward ( $B_{S1}^a < B \leq 10 \text{ T}$ ) and reverse ( $B_{F2}^a < B \leq B_{S2}^a$ ) transformations at 143 K and 153 K, the reverse transformation shows a much faster increase compared to the forward transformation. This relates to the slower field-sweep rate of the pulse (fig. 3.10) for decreasing fields, which also decreases the delay of the thermocouple reading.

The assertion of an incomplete transformation is in contrast to the results of adiabatic magnetization measurements in pulsed-fields given in chap. 4.1.1, where a complete transformation is observed. The inconsistency of the two measurements can be explained by different time-responses of the magnetic and structural transformations. The magnetic response is fast and can follow the field-sweep rate of about  $1 \text{ kTs}^{-1}$ , while the structural response is slower and cannot follow the field-sweep rate. The reason for the slow structural response can be due to the large volume change (about 0.5%) at the transition. The volume change induces strain and stress in the material [Ç14b] leading to a slow response.

The comparison of the critical fields in isothermal and adiabatic magnetization

measurements, presented in chap. 4.1.1 fig. 4.5, indicated a  $\Delta T_{\text{ad}}$  of 3.2 K at 140 K, and 3.9 K at 151 K. These values coincide perfectly with the direct measurements of  $\Delta T_{\text{ad}}$  in fig. 4.9.

The  $\Delta T_{\text{ad}}$  measurements of the sample  $\text{Mn}_3\text{GaC}$  1 in pulsed-field with a field-sweep-rate up to  $1 \text{ kTs}^{-1}$  show that the structural transformation of the first-order AF/FM transition cannot follow this rate, leading to a reduced  $\Delta T_{\text{ad}}$  compared to slower field rates. A detailed comparison of the  $\Delta T_{\text{ad}}$  measurements with different field-sweep rates is given in the next chapter.

#### 4.1.6 Comparison of $\Delta T_{\text{ad}}$ at different field-sweep rates

In this chapter, we compare the results of the  $\Delta T_{\text{ad}}$  measurements presented in chap. 4.1.2, 4.1.3, 4.1.4, and 4.1.5.  $\Delta T_{\text{ad}}$  is also compared with  $\Delta S$  obtained from the isothermal magnetization measurements in chap. 4.1.1.

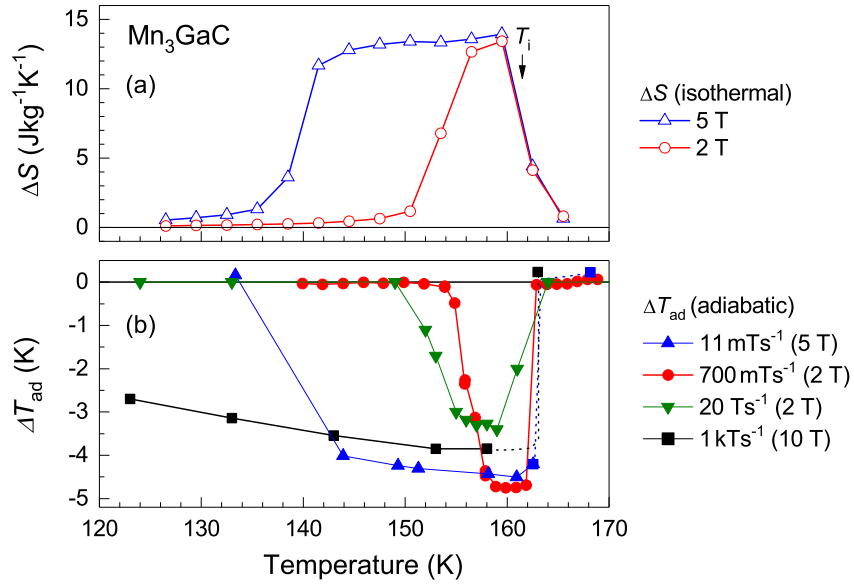


**Figure 4.10:** (a) Entropy change  $\Delta S_T$  of compact  $\text{Mn}_3\text{GaC}$  1 for 2 T (red) and 5 T (blue) field change as a function of target temperature (fig. 4.3(b)). (b) Target temperature dependent  $\Delta T_{\text{ad}}$  for different field-sweep rates. For 10 T pulsed field  $\Delta T_{\text{ad}}$  is lower due to the incomplete transformation. The  $\Delta T_{\text{ad}}$  at  $20 \text{ Ts}^{-1}$  show a lower  $\Delta T_{\text{ad}}$  and a shift of the transition the different carbon content in sample  $\text{Mn}_3\text{GaC}$  2 [Sch15].

Fig. 4.10 shows  $\Delta S$  (open symbols) and  $\Delta T_{\text{ad}}$  (full symbols) in the vicinity of  $T_i$  as a function of temperature. Fig. 4.10(a) shows  $\Delta S$  for an isothermally applied field of 2

(red) and 5 T (blue). Fig. 4.10(b) shows  $\Delta T_{\text{ad}}$  as a function of temperature. The  $\Delta T_{\text{ad}}$  measurements at a field-sweep rate of  $11 \text{ mTs}^{-1}$  and a maximum field of 5 T are shown in blue. The data for  $700 \text{ mTs}^{-1}$  and  $20 \text{ Ts}^{-1}$  for a maximum field of 2 T are shown in red and green, respectively. The data for  $1 \text{ kTs}^{-1}$  and a maximum field of 10 T are shown in black.

The  $700 \text{ mTs}^{-1}$ -data show a  $\Delta T_{\text{ad}}$  around zero for  $T \leq 152 \text{ K}$ , since 2 T is not sufficient to induce the AF to FM transition. Between 154 and 162 K,  $\Delta T_{\text{ad}}$  is negative showing the inverse MCE. A nearly constant  $\Delta T_{\text{ad}}$  of about  $-4.7 \text{ K}$  in the range  $158 < T \leq 162 \text{ K}$  indicates a complete AF/FM transition in 2 T. Above  $T_i = 163 \text{ K}$ , the sample is in the FM phase, and  $\Delta T_{\text{ad}}$  is close to zero.

The  $11 \text{ mTs}^{-1}$ -data show a  $\Delta T_{\text{ad}}$  around zero for  $T < 144 \text{ K}$ , since a field of 5 T is not sufficient to induce the AF/FM transition. The transition can be induced in the range  $144 \leq T \leq 162 \text{ K}$  giving a negative  $\Delta T_{\text{ad}}$ . A value of  $-4.5 \text{ K}$  is observed at 161.2 K and the value gradually reduces to  $-4 \text{ K}$  at 144 K. Above  $T_i$ , the sample is in the FM state and the conventional MCE leads to a  $\Delta T_{\text{ad}}$  of about  $0.2 \text{ K}$  in 5 T.

Measurements at  $1 \text{ kTs}^{-1}$  show a negative  $\Delta T_{\text{ad}}$  even at 123 K and attain a value of  $-3.7 \text{ K}$  at 153 K. As the measurements with  $11 \text{ mTs}^{-1}$ ,  $\Delta T_{\text{ad}}$  decreases with decreasing temperature. Above  $T_i$ , the sample is in the FM state and a conventional MCE with a  $\Delta T_{\text{ad}}$  of about  $0.2 \text{ K}$  can be observed. The  $11 \text{ mTs}^{-1}$  and  $700 \text{ mTs}^{-1}$ -measurements show a comparable  $\Delta T_{\text{ad}}$  for a full transformation, while the measurements with a  $1 \text{ kTs}^{-1}$ -rate show a lower  $\Delta T_{\text{ad}}$ . This verifies that maximum  $\Delta T_{\text{ad}}$  depend on the field-sweep rate. The  $\Delta S$ , observed in the isothermal magnetization measurements in chap. 4.1.1, and  $\Delta T_{\text{ad}}$ -curves have similar profiles for the 2 T and 5 T-data. The  $\Delta S$ -curve for 5 T shows, as the  $\Delta T_{\text{ad}}$ -curves, a decrease with decreasing temperature.

$\Delta T_{\text{ad}}$  for the field-sweep rate of  $20 \text{ Ts}^{-1}$  is measured on sample  $\text{Mn}_3\text{GaC}$  2, which has a slightly lower  $T_i$  of 161 K than that of sample  $\text{Mn}_3\text{GaC}$  1. Therefore, this sample shows a shifted  $\Delta T_{\text{ad}}$ -curve compared to the  $\Delta T_{\text{ad}}$ -curve for  $700 \text{ mTs}^{-1}$  and the  $\Delta S$ -curve for 2 T. A full transformation from the AF to the FM state with a nearly constant  $\Delta T_{\text{ad}}$  of about  $-3.5 \text{ K}$  is observed in the range  $156 \leq T \leq 159 \text{ K}$ . Below 156 K, a lower  $\Delta T_{\text{ad}}$  is observed, since 2 T is not sufficient to induce a full AF/FM transition. For  $T \leq 149 \text{ K}$ , no transformation can be induced and  $\Delta T_{\text{ad}}$  is zero. The same is observed for  $T > 161 \text{ K}$ , where the sample is in the FM state. The lower value of  $\Delta T_{\text{ad}} = -2 \text{ K}$  at 161 K can be explained by a mixed AF/FM state at the start of the measurements. The comparison of the maximum  $|\Delta T_{\text{ad}}|$  of  $20 \text{ Ts}^{-1}$  and  $700 \text{ mTs}^{-1}$ -measurements shows a lower value of  $|\Delta T_{\text{ad}}|$  for  $20 \text{ Ts}^{-1}$  arising possibly from the different carbon concentrations in the sample and is also the reason for the different  $T_i$  [Dia14].

The  $\Delta T_{\text{ad}}$  measurements and the isothermal  $\Delta S$  show that a full transition can be achieved even in a 2 T field with a field-sweep rate of up to  $20 \text{ Ts}^{-1}$ . The maximum  $\Delta T_{\text{ad}}$  of  $-4.7 \text{ K}$  is measured for the moderate field-sweep rate of  $700 \text{ mTs}^{-1}$  in a field of 2 T. The value is close to  $-5.4 \text{ K}$  which is estimated from the data of Tohei et al. [Toh03] for a full transformation from the AF to the FM phase in 2 T. The comparison of

$\Delta T_{\text{ad}}$  of the samples Mn<sub>3</sub>GaC 1 and Mn<sub>3</sub>GaC 2 shows that the carbon concentration in Mn<sub>3</sub>GaC is an important parameter regarding  $\Delta T_{\text{ad}}$ . The measurements in pulsed fields with rates up to 1 kTs<sup>-1</sup> also show a reduced  $\Delta T_{\text{ad}}$  compared to lower rates, which shows that also the field-rate plays an important role. The optimum field-rate for this alloy is between 700 mTs<sup>-1</sup> and 20 Ts<sup>-1</sup>. This is equivalent to a 2 T field-oscillation with a frequency between 0.3 and 10 Hz, which matches with the operating frequency of active magnetic regenerators at the moment [Yu10].

## 4.2 Characterization of $Mn_3GaC$ single crystal and comparison with polycrystalline sample

This chapter presents the results of investigations on structural and magnetic properties of a  $Mn_3GaC$  single crystal, which as obtained for the first time. The results are compared with those of polycrystalline specimens. The first section deals with the compositional (EDX) and structural (EBSD) analysis. In the second part, the results on magnetic properties investigated by magnetization and magnetic resonance measurements techniques are shown.

### 4.2.1 Structural characterization

A  $Mn_3GaC$  single crystal of size  $15 \times 15 \times 28 \mu m^3$  is separated from a segregated off-stoichiometric  $Mn_3GaC$  sample which was prepared by solid state reaction (see chap. 3.1). The crystal is fixed by carbon tape on a Si substrate to handle the crystal for the different analysis. Carbon tape and Si substrate are chosen due to there good conductivity necessary for characterization by SEM, EDX and EBSD.

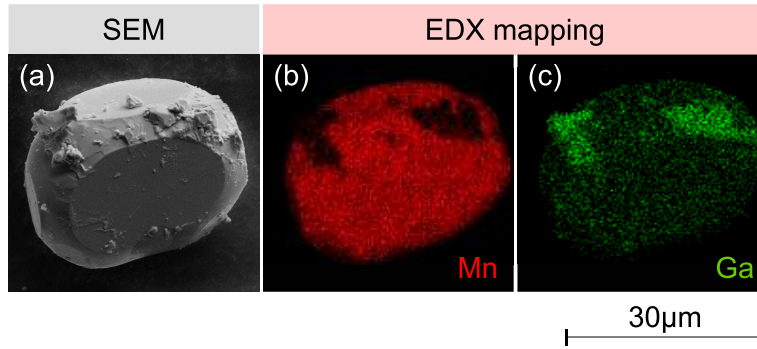


**Figure 4.11:** (a) SEM image of the  $Mn_3GaC$  crystal with small pieces of Ga-rich phase at the corners. (b) and (c) show the Mn  $K_{\alpha 1}$  (red) and the Ga  $K_{\alpha 1}$  (green) emissions of the EDX mapping of the crystal.

The SEM image in fig. 4.11(a) show a faceted rectangular crystal. Irregular smaller crystallites are located at the corner of the crystal as well as on top of the facets. An EDX analysis is carried out to determine the composition of the crystal. Fig. 4.11(b) and (c) show the Mn  $K_{\alpha 1}$  (red) and the Ga  $K_{\alpha 1}$  (green) emissions of the EDX mapping. The crystal itself is composed of a Mn-rich phase with a Mn/Ga ratio of 3 : 1, while the small irregular crystallites at the corners are composed of a Ga-rich phase with a ratio of 7 : 18. The composition of the Ga-rich phase is close to that of  $Mn_2Ga_5$  [Kim08].

EBSD measurements were carried out to confirm the antiperovskite structure of

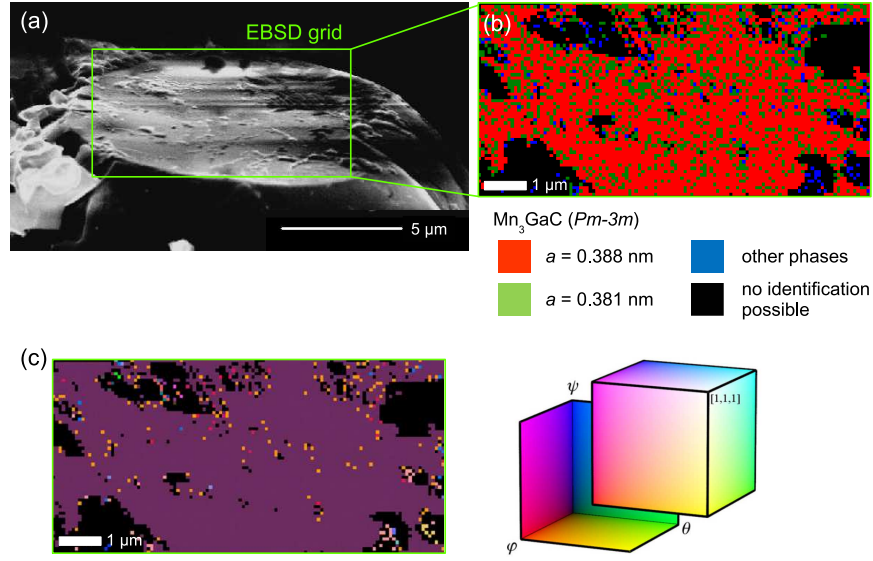


**Figure 4.12:** (a) SEM image of the surface of  $\text{Mn}_3\text{GaC}$  crystal, the green frame marks the grid of the EBSD analysis. (b) EBSD grid ( $9.6 \times 4.8 \mu\text{m}$  with a resolution of  $0.08 \mu\text{m}$ ) the color code corresponds to the identified phases. (c) EBSD grid with color coded crystal orientation direction. Color code of the Euler angles and crystal orientation directions, see [Nol15] fig. 7.

$\text{Mn}_3\text{GaC}^*$ . The analysis identifies the crystallographic orientation of the sample and verifies its single-crystallinity. Fig. 4.12(a) shows the surface of the  $\text{Mn}_3\text{GaC}$  crystal which is used for the analyses. The grid of the analyzed area is marked with the green frame. The EBSD image is a  $20^\circ$  projection of fig. 4.11(a). No surface treatment was carried out. The grid has dimensions of  $9.6 \times 4.8 \mu\text{m}^2$  with a resolution of  $0.08 \mu\text{m}$ . The diffraction pattern of each cell is compared with a simulated pattern of the antiperovskite structure of  $\text{Mn}_3\text{GaC}$  and other potential phases. The identification process is described in chap. 3.2.2. Fig. 4.12(b) shows the EBSD grid, and the phases of the cells in color code. The red cells are identified as  $\text{Mn}_3\text{GaC}$  with a lattice constant of  $a = 0.388 \text{ nm}$ . The green cells also correspond to a  $\text{Mn}_3\text{GaC}$  structure but with a smaller lattice constant ( $a = 0.381 \text{ nm}$ ) [Lew06]. The two different lattice parameter of  $\text{Mn}_3\text{GaC}$  are chosen to consider the variation of  $a$  given in the literature. Reference [Dia14] shows that the cell volume of  $\text{Mn}_3\text{GaC}_x$  decreases with decreasing carbon concentration  $x$ . Therefore, the EBSD analysis can estimate the carbon content. The blue cells are identified as other phases, and the black cells are marked as cells where an identification is not possible due to insufficient contrast in the diffraction pattern. The analysis shows that the main part of the surface is identified as  $\text{Mn}_3\text{GaC}$  with  $Pm - 3m$  symmetry and a lattice constant of  $a = 0.388 \text{ nm}$  (red). The second common structure is  $\text{Mn}_3\text{GaC}$

\*The measurements are performed together with Dr. Detlef Spoddig.

with  $a = 0.381$  nm (green). The missing phase boundary between the red and blue areas indicates that both areas belong to the same structure and a distinction between the different  $a$  parameters cannot be made. The resolution of lattice constant obtained from EBSD measurements depends on the quality of the Kikuchi pattern which again depends on the quality of the sample surface. Other phases (blue) are only detected in or near areas where an identification is not possible. The un-identified areas (black) and other phases (blue) are mainly located at the corner of the crystal where a clear identification is difficult. A reliable phase identification is obtained at the center of the facet. The diffraction patterns give also the crystallographic orientation of the  $\text{Mn}_3\text{GaC}$  surface. Fig. 4.12(c) shows the measured Euler angles  $\varphi, \theta$  and  $\psi$  of the diffraction pattern using the common representation of the color code given next to the figure [Nol15]. The surface is determined to be a (100) plane after taking into account the tilt of the surface with the detector. The black area corresponds again to the cells with insufficient contrast of the diffraction pattern. The other orientations (blue, orange, green, etc.) coincide with the areas which were identified as other phases in fig. 4.12(b).

EBSD and EDX confirm the antiperovskite structure of  $\text{Mn}_3\text{GaC}$  and its composition, respectively. It further shows that the crystal grows with surfaces parallel to  $\{100\}$ .

### 4.2.2 Magnetic properties

The magnetic properties of the  $\text{Mn}_3\text{GaC}$  single crystal are studied using magnetization and FMR measurements. Angular-dependent FMR measurements in combination with simulations provides information on the magneto-crystalline anisotropy energy of  $\text{Mn}_3\text{GaC}$ . Regarding the MCE, the field-induced transition along the magnetization easy-axis leads to the fastest change of the magnetization [Fri16].

#### Magnetization

The temperature-dependent magnetization of the  $\text{Mn}_3\text{GaC}$  single crystal is shown in fig. 4.13.  $M(T)$  is measured in a field of 50 mT (red, right axis) and 2 T (black, left axis). The measurements are done using the ZFC, FC and FW protocol (see chap. 3.3.1). The background due to the carbon tape, the Si substrate, and the FM impurities of the  $\text{Mn}_2\text{Ga}_5$  phase, is subtracted from the data. The background is determined from the data in the AF temperature-range ( $T \leq 140$  K). The crystal exhibits a FM/PM transition at  $T_C = 236$  K and an AF/FM magnetostructural transition at  $T_i = 163$  K in a field of 50 mT. The difference of the FC and FW measurements in the vicinity of  $T_i$  shows a thermal hysteresis of  $\Delta T_{\text{hyst}} = 3$  K.  $M(T)$  measured in 2 T shows a decrease of  $T_i$  by  $-5 \text{ K T}^{-1}$ , while the hysteresis remains as 3 K. The transition temperatures, thermal hysteresis, and shift of the transition temperature are similar to those in bulk  $\text{Mn}_3\text{GaC}$  [Toh03, Ç12, Sch15]. The narrow hysteresis,  $\Delta T_{\text{hyst}} = 3$  K, of the single crystal is the same as in bulk  $\text{Mn}_3\text{GaC}$  with no carbon deficiency [Dia14, Ç15b]. A thermal broadening of the first-order magnetostructural transition is observed in carbon deficient alloys [Ç15b]. Due to the absence of broadening and the identification of a homogeneous  $\text{Mn}_3\text{GaC}$  phase (EBSD measurements chap. 4.2.1), we consider that the single crystal has no carbon deficiency.



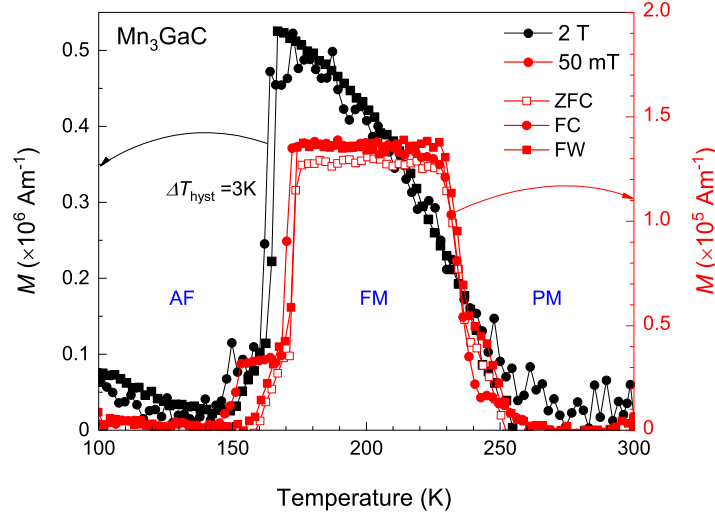


**Figure 4.13:** Temperature-dependent magnetization of  $\text{Mn}_3\text{GaC}$  single crystal for an applied field of 50 mT (red, right axis) and 2 T (black, left axis).

### Ferromagnetic resonance

Regarding the MCE, a sharp field-induced transformation (with a fast change of the magnetization) favors reversible  $\Delta T_{\text{ad}}$  in low magnetic fields. The smallest saturation field is obtained when the magnetization easy-axis is parallel to the field-direction. The easy-axis is governed by the shape, surface, and magnetocrystalline anisotropies (see chap. 3.3.2). The influence of the MCAE on the MCE is, for example, shown by  $\Delta T_{\text{ad}}$  and  $\Delta S$  measurements on a  $\text{Co}_2\text{B}$  single crystal [Fri16]. The study shows an increase of  $\Delta T_{\text{ad}}$  and  $|\Delta S|$  when the field is applied along the magnetization easy-axis with respect to applying the field along the hard-axis. For a powder sample of  $\text{Co}_2\text{B}$ , these are at intermediate values. An anisotropic MCE can also be observed on single crystal rare-earth metals [And89, Sko16].

Till now, no measurements on  $\text{Mn}_3\text{GaC}$  single crystal have been reported. In previous studies, it has been suggested that the MCAE has to be small to cause a sharp first-order transition [Toh03]. In this case, the effect of the MCAE on the thermal hysteresis,  $\Delta T_{\text{ad}}$ , and  $|\Delta S|$  would also be weak. This explains the similar  $M(T)$  results obtained for measurements on bulk and single crystalline  $\text{Mn}_3\text{GaC}$  shown above. Here, FMR measurements are carried out on the  $\text{Mn}_3\text{GaC}$  single crystal to estimate the MCAE.

The FMR measurements were carried out in a Varian TE102 cavity with an eigenfrequency of 9.238 GHz equipped with a cooling-attachment operating in the temperature-

range  $100 \leq T \leq 300$  K. A field-modulation of 1.5 mT with a frequency of 100 kHz was applied \*. The details of the setup are described in chap. 3.3.2.

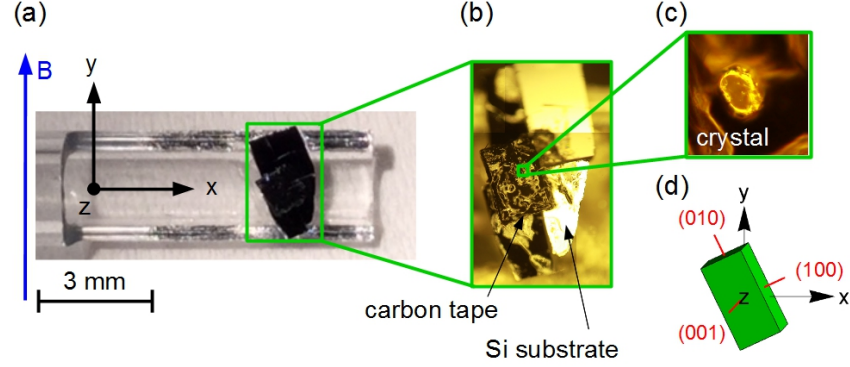


**Figure 4.14:** FMR quartz-tube sample-holder (a) with  $\text{Mn}_3\text{GaC}$  crystal shown in (b) and (c). (d) shows the sketch of the crystal orientation related to the coordinate system of the FMR setup.

Fig. 4.14(a) shows the quartz-tube sample-holder with the sample fixed with silica glass. The images 4.14(b) and 4.14(c) show the sample on top of the carbon tape fixed on the Si substrate. The sketch in fig. 4.14(d) shows the orientation of the crystal with respect to the coordinate system of the FMR setup. Fig. 4.14(d) shows the crystal-orientation for the rotation angle  $\theta = 0^\circ$ . The longitudinal axis of the crystal is at an angle  $26^\circ$  with the y-axis and  $13^\circ$  with the z-axis. The crystallographic axes are marked in red. In the FMR setup, the magnetic field generated by the electromagnet is aligned along the y-axis, and the magnetic component of the high-frequency field of the microwave is aligned along the z-axis. The sample is rotated in the y-z plane.

Temperature-dependent FMR measurements are performed at constant rotation-angle  $\theta = 0^\circ$  in the temperature-range  $150 \leq T \leq 270$  K. Fig. 4.15 shows the spectra in the field-range  $0 \leq B \leq 0.6$  T. All spectra are subtracted from a reference spectrum taken at 140 K which includes the ESR of the carbon tape, of which the position is indicated by the red line. The origin of the ESR are free radicals giving a temperature-independent signal. At 140 K, no FMR signal can be observed, since the sample is in the AF phase. The same applies for the measurements at 150 K and 160 K. For  $T > T_i = 163$  K, the crystal is in the FM phase and FMR can be observed at 0.289 T at 170 K. With increasing temperature, the saturation magnetization decreases, and the FMR shifts to the ESR position at 0.332 T. Above  $T_C = 236$  K, the sample is in the PM state, and thus, the ESR of the crystal is superimposed by the ESR signal of the background, which is by far stronger due to the large amount of carbon tape.

\*The measurements are performed together with Dr. Ralf Meckenstock.

## 4.2 Characterization of $\text{Mn}_3\text{GaC}$ single crystal and comparison with polycrystalline sample

The spectra measured at a temperature above  $T_C$  show a small dip around 0.332 T. The presence of this dip is related to the broader line width of the PM signal with respect to the line width of the ESR signal of the carbon tape. The subtraction of the reference spectrum gives the spectrum for  $\text{Mn}_3\text{GaC}$ .

In addition to the main resonance around 0.289 T, further minor resonances can be observed in the field-range  $0.330 \leq \mu_0 H \leq 0.463$  T up to 220 K. As the main resonance, the additional resonances are only present in the FM phase. The intensity of the excitations increase with increasing temperature and reaches a maximum at 210 K, while the resonance field shifts to the ESR position as the main FMR does. For  $T \geq 220$  K, the minor resonances superimpose with the ESR of the background and can no longer be detected. The origin of these lines are discussed below, where we study the angular dependence of the FMR.

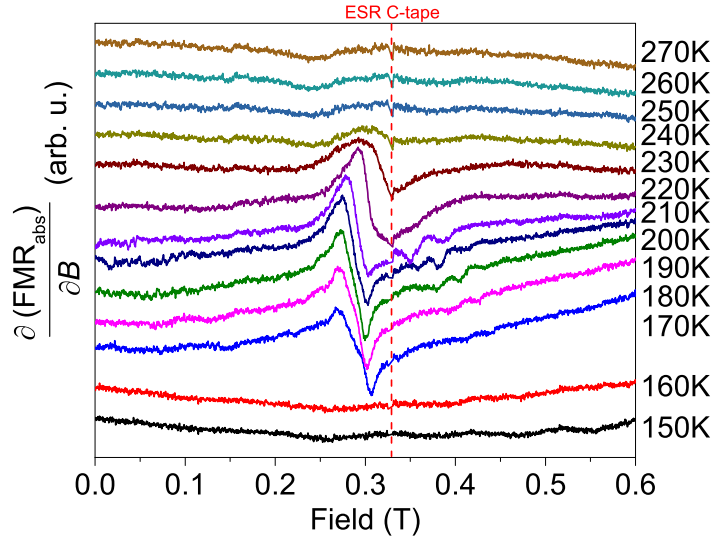


**Figure 4.15:** Field-dependent FMR absorption derivative  $\partial(\text{FMR}_{\text{abs}})/\partial B$  spectra of  $\text{Mn}_3\text{GaC}$  crystal performed in the temperature range  $150 \leq T \leq 270$  K at constant angle ( $\theta = 0^\circ$ ). All spectra are subtracted by a reference spectra at 140 K to eliminate the ESR background signal.

Angular-dependent FMR spectra are performed in the FM state of the crystal to study the different resonances in more detail and to determine the MCAE of  $\text{Mn}_3\text{GaC}$ . Angular-dependent FMR spectra of the  $\text{Mn}_3\text{GaC}$  crystal are shown in fig. 4.16(i) in the range  $0.2 \leq B \leq 0.5$  T. The measurements are performed at 200 K. The FMR absorption derivative  $\partial(\text{FMR}_{\text{abs}})/\partial B$  is gray scaled where black is negative and white is positive. An angular range  $220^\circ$  is chosen since we expect a twofold shape anisotropy energy (SAE) and a fourfold MCAE. A minimum range of  $180^\circ$  is required to include all crystallographic directions. Due to the  $13^\circ$  tilt between the longitudinal crystal-axis

and the y-axis, the range must be further extend by a minimum of  $26^\circ$  to ensure that all principle crystalline-axes are included in the angular-dependent measurements (see fig. 4.16 (a), (c), (e), and (g)). The crystal is rotated in steps of  $1^\circ$ . Fig. 4.16(a),(c),(e), and (g) show schematically the orientation of the crystal for the rotation-angles  $0^\circ$ ,  $86^\circ$ ,  $130^\circ$ , and  $170^\circ$ . Fig. 4.16(b), (d), (f), and (h) show the corresponding orientations of the  $\text{Mn}_3\text{GaC}$  unit cell. The angular-dependent gray scale plot of  $\partial(\text{FMR}_{\text{abs}})/\partial B$  principally provides FMR line positions on crossing from bright to dark shades. The gray scale plot shows a twofold symmetry with an easy-axis at about  $0^\circ$  and  $170^\circ$  and a hard-axis at  $86^\circ$ . The ESR of the carbon tape at 0.322 T is independent of sample-rotation.

At  $0^\circ$  (fig. 4.16(a)), the longitudinal axis of the crystal is aligned principally along the y-direction, and therefore, parallel to the external magnetic field. The rotation aligns the longitudinal axis more and more along the x-axis. A nearly perfect alignment of the longitudinal axis and the x-axis is attained at  $86^\circ$  so that the short-axis is essentially parallel to the magnetic field (fig. 4.16(c)). Concerning the SAE, the parallel alignment of the short-axis with the magnetic field corresponds to the hard-axis of magnetization, and the parallel alignment of the longitudinal axis with the magnetic field corresponds to the easy-axis. This situation is seen in the angular-dependent FMR in fig. 4.16(i) where an increase of the FMR field from 0.28 T ( $0^\circ$ ) to 0.36 T ( $86^\circ$ ) is seen. Further rotating to  $170^\circ$  leads again to a parallel alignment of the longitudinal axis and the field (fig. 4.16(g)). The angular-dependent FMR measurements in this angular range show a decrease of the FMR field to the minimum value of 0.28 T. The dominant influence of the SAE is shown by the twofold symmetry of the FMR field in this range. The influence of the MCAE is reflected in the asymmetry of the principle twofold symmetry. The effect can especially be observed around  $86^\circ$  at the steep maximum and at the broad minimum in the range  $150^\circ \leq \theta \leq 200^\circ$ . Additional FMR can be observed in the range  $0.35 \leq B \leq 0.45$  T for the whole angular range. These additional resonances were already observed in temperature-dependent FMR measurements (fig. 4.15) in the range  $190 \leq T \leq 210$  K. These additional resonances can be related to excitations occurring at the edges of the crystal [McM06]. Concerning the volume-to-surface ratio of the crystal, we would expect a much lower intensity for these edge modes compared to the main FMR. On the other hand, the width of the main FMR is at least four times broader than the width of the edge modes. In the case of large samples with dimensions greater than the penetration depth of the microwave ( $\sim 2 \mu\text{m}$ ), the resonance-width is additionally broadened [Poo83, Fra88]. Therefore, the broadening can be explained by an inhomogeneous excitation in the crystal due to its large dimension. This indicates that the additional FMR corresponds to excitations at the edges of the crystal which normally extend about 150 nm [Mec08]; far smaller than the penetration depth of the microwave. Since the edge modes are governed by the surface of the crystal, their angular dependence shows a fourfold symmetry.

The presence of a second weaker FMR which can be seen below the main FMR

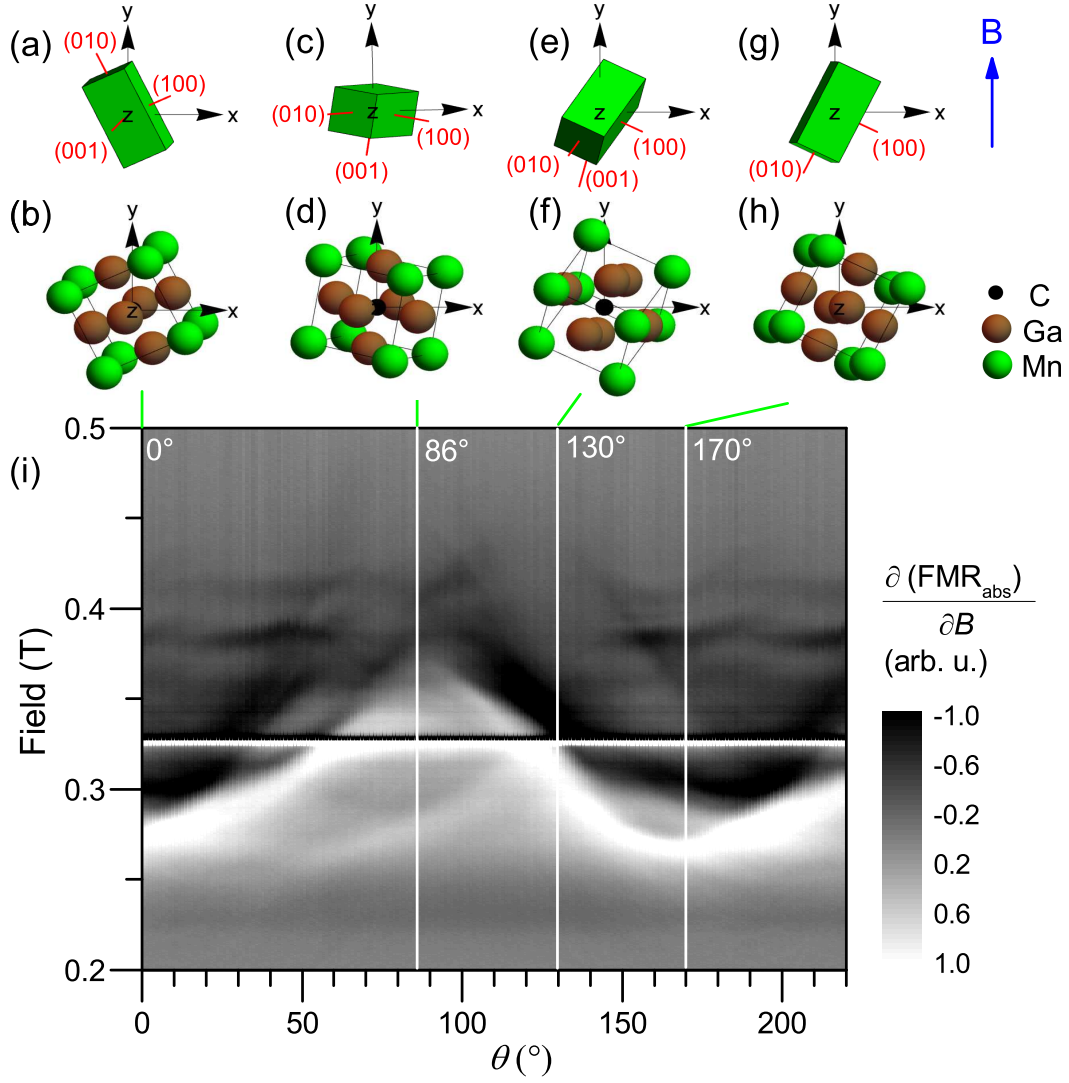


**Figure 4.16:** Angular-dependent FMR spectra of  $\text{Mn}_3\text{GaC}$  crystal. (a)-(h) show the orientation of the schematic crystal and the unit cell of cubic  $\text{Mn}_3\text{GaC}$  at the rotation angle  $0^\circ$ ,  $86^\circ$ ,  $130^\circ$ , and  $170^\circ$ . (i) Angular and field-dependent FMR absorption derivative  $\partial(\text{FMR}_{\text{abs}})/\partial B$  in gray scale measured at 200 K

in the range  $30^\circ \leq \theta \leq 110^\circ$ , and in the range  $140^\circ < \theta < 190^\circ$  above the main FMR is most probably due a second phase in the  $\text{Mn}_3\text{GaC}$  crystal with a different crystallographic orientation. The angular dependence of these FMR is shifted relative to the main FMR, which indicates that the second phase has a different crystalline orientation than the main crystal.

In summary, the angular-dependent FMR study shows a dominant SAE compared to MCAE for  $\text{Mn}_3\text{GaC}$ . A value for the MCAE cannot be calculated straight-forward since the sample is not aligned along a distinct direction of the experimental setup. However the MCAE can be estimated by simulating the FMR described in chap. 3.3.2. The results are given in the next section.

### Simulation of angular-dependent ferromagnetic resonance spectra

To analyze the angular-dependent FMR spectra in fig. 4.16(i) we compare the spectra with a general analytical solution of the LLG equation (3.3) [Zin17,Zin16]. A description of the calculation is given in chap. 3.3.2.

For the calculation of the free energy density  $F$  in eq. (3.7), we assume a fourfold MCAE  $K_4$  due to the cubic structure of  $\text{Mn}_3\text{GaC}$ . The SAE and the demagnetization matrix  $\underline{N}$  are calculated by the crystalline orientation shown in fig. 4.14(d). The shape of the sample shown in fig. 4.11(a) is approximated as an ellipsoid and is used to calculate the SAE. The saturation magnetization of the crystal is known from the magnetization data (chap. 4.2.2). This makes  $K_4$  the only free parameter for the calculation.

The best match of the simulation and measurements is obtained for a MCAE

$$K_4 = -5.49 \text{ kJm}^{-3}.$$

The calculated angular and field-dependent spectra are shown in fig. 4.17(i) \*. The amplitude is plotted in gray scale in the same field and angular range as the measured spectra in fig. 4.16(i). The angular dependence of the simulated line-position agrees well with the measured one. The simulations show, similar to the measurements, a twofold symmetry due to a dominant SAE and an asymmetry in the twofold symmetry due to the MCAE. The good agreement between the measurements and the calculations gives validity to the assumption of a dominant SAE and a small MCAE. The negative sign of  $K_4$  indicates that the  $\{111\}$ -direction is the magnetization easy-axis and the  $\{100\}$ -direction is the hard-axis.

Fig. 4.16 (a), (c), (e), and (g) show the crystal-orientation at the angle  $0^\circ$ ,  $86^\circ$ ,  $130^\circ$  and  $170^\circ$ . The corresponding orientation of the  $\text{Mn}_3\text{GaC}$  unit cell is shown in 4.16 (b), (d), (f), and (h). At  $0^\circ$  (fig. 4.16(b)), the (120)-direction is nearly parallel to the external field. Rotation by  $86^\circ$  aligns the (00-1)-direction nearly parallel to the

---

\*The simulations are performed together with Benjamin Zingsem.

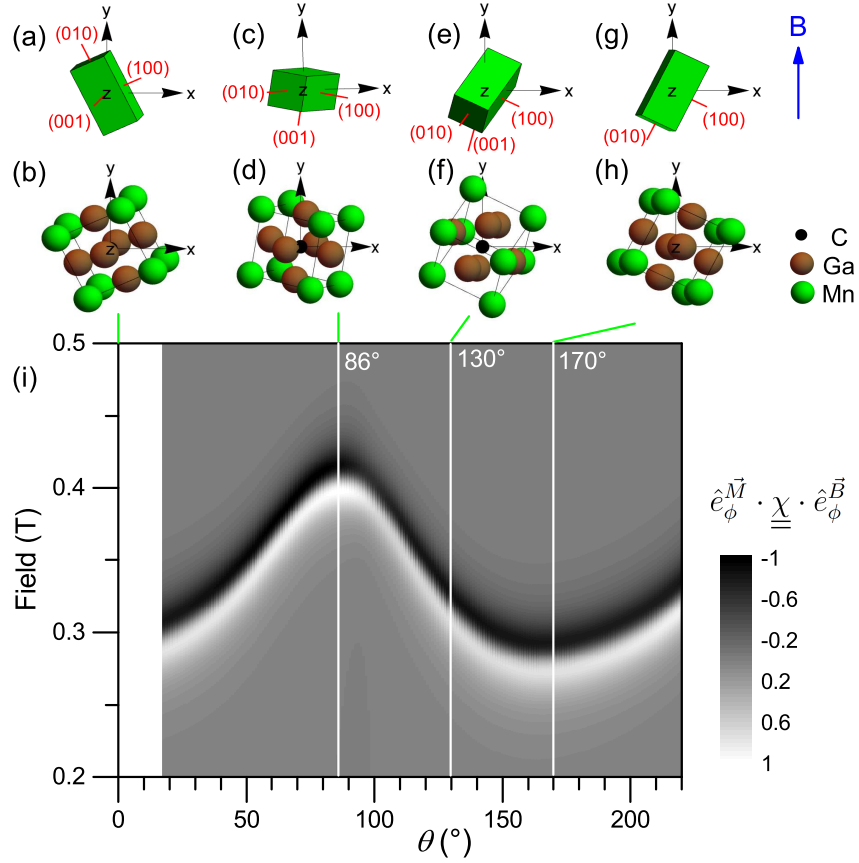


**Figure 4.17:** Simulation of the angular-dependent FMR spectra of  $\text{Mn}_3\text{GaC}$  crystal. The simulation is performed on in the same field and angular range as the measurements in fig. 4.16. (a)-(h) show the orientation of the schematic crystal and the unit cell of cubic  $\text{Mn}_3\text{GaC}$  at the rotation angle  $0^\circ$ ,  $86^\circ$ ,  $130^\circ$ , and  $170^\circ$ . (i) show the simulated field and angular-dependent amplitude of  $\hat{e}_\phi^{\vec{M}} \cdot \underline{\chi} \cdot \hat{e}_\phi^{\vec{B}}$  for  $\text{Mn}_3\text{GaC}$  crystal.

field. During the rotation from  $86^\circ$  to  $170^\circ$ , the  $(-1-1-1)$ -direction becomes parallel to the field at  $160^\circ$ . At  $170^\circ$ , the  $(-1-20)$ -direction is nearly aligned along the field, which in the cubic system is equivalent to the  $(120)$ -direction. At  $160^\circ$ , the  $(111)$ -direction of the crystal is nearly parallel to the y-axis, while for  $86^\circ$ , the  $(001)$ -direction is parallel to the y-axis. In the vicinity of these angles, a deformed, sine-like FMR is observed, which identifies the  $\{111\}$ -direction as the easy direction of the MCAE and the  $\{001\}$ -direction as the hard direction. This is in agreement with the results of previous studies on  $\text{Mn}_3\text{GaC}$  powder that identify the  $\{111\}$ -direction as the easy-axis and the  $\{001\}$ -direction as the hard-axis [Fru78]. Between  $160^\circ$  and  $200^\circ$ , the  $(110)$ -direction becomes parallel to the external magnetic field. The direction corresponds to a moderate hard-axis of the crystal which leads to a broadening of the FMR in this range. In conclusion, it can be said that the estimated anisotropy  $K_4 = -5.49 \text{ kJm}^{-3}$  of  $\text{Mn}_3\text{GaC}$  is one order of magnitude smaller than that of bcc Fe [Hal98, Tun82], so that this low anisotropy can be the reason for the sharp magnetostructural transition  $T_i$  in this alloy [Toh03].

Concerning amplitude and line-width, the simulation gives constant values, whereas in the measurements, the amplitude in the hard-direction reduces and the line-width broadens. Both effects can be explained by the inhomogeneous excitation of the sample by the microwave. The simulation considers a homogeneous microwave excitation, and a smaller line-width is expected. The reduction of the amplitude in the hard-direction of the measurement can be related to the position of the crystal. As shown in fig. 4.17(c), the external magnetic field is almost perfectly oriented along the  $(00-1)$ -direction, which is, regarding the SAE and the MCAE, a hard-axis. For this reason, the edge modes have also their hardest direction along this orientation. Due to this, the highest pinning of the main mode by the edge mode takes place at this orientation reducing the excitation of the main mode by the microwave. The assumption requires support by micro-magnetic simulations.



### 4.3 Transition dynamics of (Mn,Cr,Co)Sb pnictides probed at different time scales

This chapter presents results on the MCE of  $\text{Mn}_{1.87}\text{Cr}_{0.09}\text{Co}_{0.04}\text{Sb}$  studied by  $\Delta S$  estimated from magnetization and the direct  $\Delta T_{\text{ad}}$  measurements performed with different field-sweep rates. Doped  $\text{Mn}_{2-y}\text{X}_y\text{Sb}$  (X as Cr, Co) alloys exhibit several magnetic phases, depending on the different doping elements, doping contents, and temperature (chap. 2.2.3). Studies on the nitrogen doped system,  $\text{Mn}_3\text{GaC}_{1-x}\text{N}_x$  (chap. 2.2.2), show that suppressing long-range FM order, and therefore, the absence of FM domains in the EPM state, could be the origin of the absence of transitional hysteresis at the first-order AF/FM transition. Using this argument, we search for a doped  $\text{Mn}_{2-y}\text{X}_y\text{Sb}$  alloy that exhibits a AF/FI transition close to room temperature to study the effect of the absence of ferromagnetism on the transitional hysteresis and the MCE.

We choose  $\text{Mn}_{1.82}\text{Cr}_{0.07}\text{Co}_{0.04}\text{Sb}_{1.07}$  as our sample system, since such alloys can exhibit an AF/FI first-order transition close to 300 K. The sample is prepared by arc melting and is subsequently annealed at 1073 K for 5 days (chap. 3.1). EDX analysis shows that the compound is homogeneous.

Section 4.3.1 presents the magnetization of  $\text{Mn}_{1.82}\text{Cr}_{0.07}\text{Co}_{0.04}\text{Sb}_{1.07}$  measured under isothermal conditions. The  $\Delta T_{\text{ad}}$  measurements under adiabatic conditions are carried out in a magnetic field with a field-sweep rate of  $11 \text{ mTs}^{-1}$ . The results are presented in chap. 4.3.2.  $\Delta T_{\text{ad}}$  measurements are also carried out in a pulsed-field with a rate up to  $1 \text{ kTs}^{-1}$  and are presented in chap. 4.3.3. Chap. 4.3.4 gives a comparison of the results of  $\Delta T_{\text{ad}}$  measurements at different field-sweep rates.

#### 4.3.1 Isothermal magnetic transition with narrow hysteresis

This section present the results of the magnetization measurements on  $\text{Mn}_{1.82}\text{Cr}_{0.07}\text{Co}_{0.04}\text{Sb}_{1.07}$ . Temperature and field-dependent magnetization measurements are carried out, and the magnetic entropy change around the transition is calculated.

Fig. 4.18 shows  $M(T)$  measured in an applied field of 5 mT (red) and 5 T (black). The magnetization is measured with the ZFC (open circle), FC (filled square) and FW (filled circle) protocol. The sample is in an AF phase at low temperature and in a FI phase at high temperature with a transition temperature at 306 K for 5 mT. The FC and FW measurement displays a narrow thermal hysteresis of  $\Delta T_{\text{hyst}} = 2.5 \text{ K}$ .  $M(T)$  at 5 T shows a decrease of  $T_i$  to 281 K at a rate of  $-5 \text{ KT}^{-1}$ . In the FI phase, the alloy has a net magnetization of  $29.5 \text{ Am}^2\text{kg}^{-1}$  at 292 K. The background at low temperatures ( $T < 200 \text{ K}$ ) is due to the presence of a FM MnSb impurity phase, which been verified by XRD.

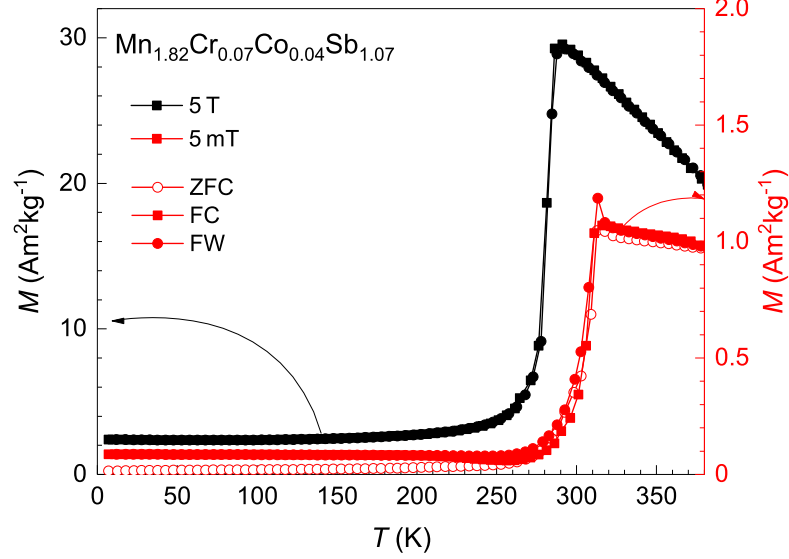


**Figure 4.18:** Temperature-dependent magnetization of  $\text{Mn}_{1.82}\text{Cr}_{0.07}\text{Co}_{0.04}\text{Sb}_{1.07}$  for an applied field of 50 mT (red, right axis) and 5 T (black, left axis).

Isothermal  $M(B)$  measurements are performed in the vicinity of  $T_i$  to calculate  $\Delta S$  (see chap. 3.3.1 eq. (3.1)). Fig. 4.19(a) shows the  $M(B)$ -curves in the temperature-range  $275 \leq T \leq 315$  K with an increment of 5 K between the measurements. At 275 K,  $M(B)$  shows a nearly linear increase with increasing magnetic field which is related to the AF phase. For the  $M(B)$  measurements above 275 K, s-type magnetization curves are observed indicating that the applied field induces an AF/FI transition. The onset of the transformation decreases with increasing temperature. At 315 K, the sample is in the FI state ( $T_i = 306$  K). For 305 K and 310 K, the sample is in a mixed AF/FI state in zero field, so that the transformed FI parts leads to a fast increase in  $M(B)$  below 0.5 T. The transition progresses by further increasing the field.

The curves at 280, 285, and 290 K exhibit a slight shoulder just before the AF/FI transformation. This can be explained by a second Mn-Cr-Co-Sb phase with a different chemical composition. Due to the different stoichiometry, this second phase has also a slightly higher transition temperature leading to a transform at lower field values.

$\Delta S$  of the transformation is calculated using equation (2.10) and  $M(B)$  in fig. 4.19(a). Fig. 4.19(b) shows  $\Delta S(T)$  for applied fields of 1, 2, 3, 4, and 5 T. The curves show a peak with a maximum of  $4.74 \text{ Jkg}^{-1}\text{K}^{-1}$  at 293 K for 5 T. Compared to other magnetocaloric materials as example  $\text{Mn}_3\text{GaC}$  ( $15 \text{ Jkg}^{-1}\text{K}^{-1}$ ) [Toh03] or  $\text{Ni}_{50}\text{Mn}_{37}\text{Sn}_{13}$  ( $18 \text{ Jkg}^{-1}\text{K}^{-1}$ ) [Kre05b], the value for  $\text{Mn}_{1.82}\text{Cr}_{0.07}\text{Co}_{0.04}\text{Sb}_{1.07}$  is about three times

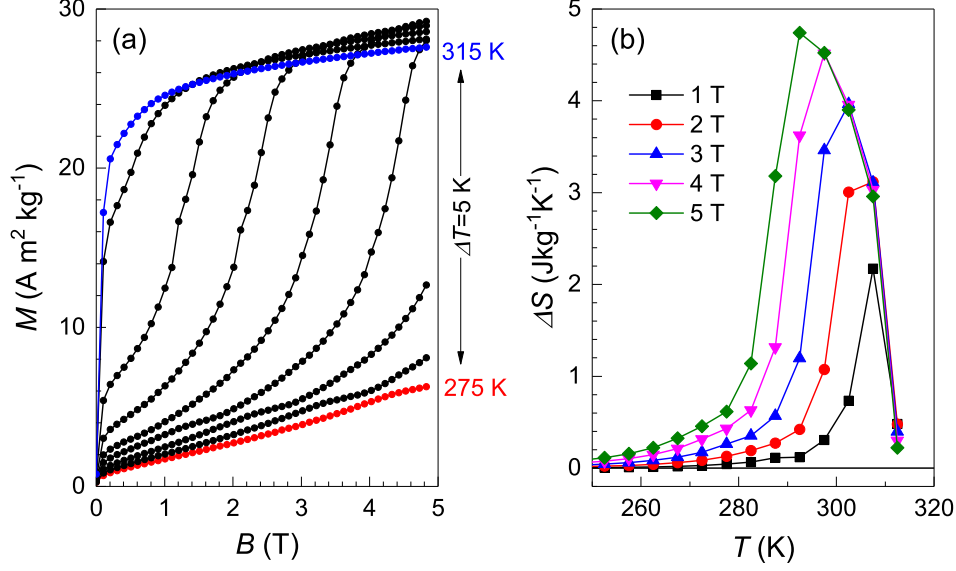


**Figure 4.19:** (a) Isothermal  $M(B)$  of  $\text{Mn}_{1.82}\text{Cr}_{0.07}\text{Co}_{0.04}\text{Sb}_{1.07}$  in the temperature range  $275 \leq T \leq 315$  K measured in steps of 5 K. (b) Temperature and field dependent  $\Delta S$  in the vicinity of  $T_i$ , calculated from  $M(B)$  measurements in (a).

smaller. However, it can still be interesting for magnetocaloric applications due to the narrow hysteresis which should give a reversible  $\Delta T_{\text{ad}}$  in small magnetic fields.

$\Delta S(T)$  of  $\text{Mn}_{1.82}\text{Cr}_{0.07}\text{Co}_{0.04}\text{Sb}_{1.07}$  exhibits no plateau as in  $\text{Mn}_3\text{GaC}$  (see fig. 4.3). This can be explained by the strong increase of the magnetization in the FI state with decreasing temperature in the range  $290 \leq T \leq 380$  K (see fig. 4.18). This increase and the increase in the difference in the magnetization before and after the transformation  $\Delta M$  leads to an increase in  $\Delta S$  (eq. (2.9)).

### 4.3.2 $\Delta T_{\text{ad}}$ at slow field-sweep rate $11 \text{ mTs}^{-1}$

This section presents the results of the adiabatic  $\Delta T_{\text{ad}}$  measurements on  $\text{Mn}_{1.82}\text{Cr}_{0.07}\text{Co}_{0.04}\text{Sb}_{1.07}$  carried out in a field of 5 T with a field-sweep rate of  $11 \text{ mTs}^{-1}$ . The measurement setup is described in chap. 3.4

$\Delta T_{\text{ad}}$  is measured in the vicinity of the AF/FI transition in the temperature-range  $260 \leq T \leq 318 \text{ K}$ . The field is cyclically applied for four times to observe the reversibility of  $\Delta T_{\text{ad}}$ . Fig. 4.20 shows the time dependence of the cycled field (blue, right axis) and the corresponding temperature change of the sample (red, left axis) measured around 287 K (AF state). The sample was initially cooled down to 260 K to ensure that it is in a defined initial state. The field of 5 T (blue, right axis) is applied and reversed after a waiting-time of 11 min. The blue highlighted areas corresponds to the time-range of changing field.

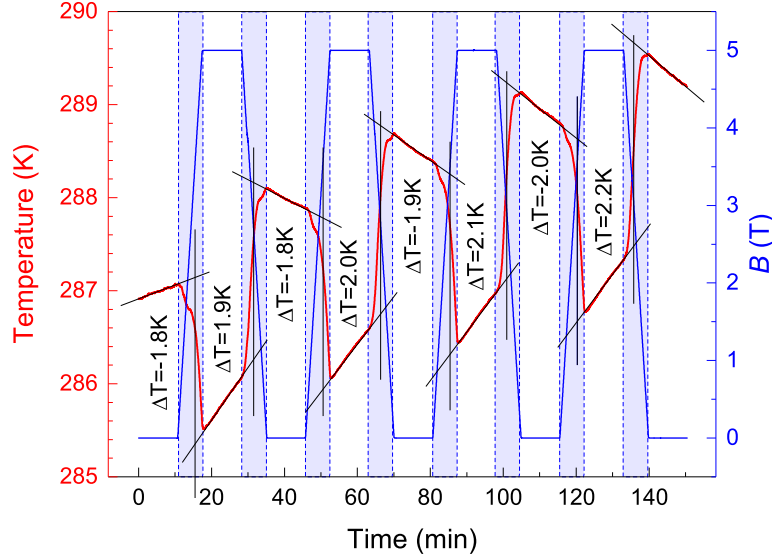


**Figure 4.20:** Direct  $\Delta T_{\text{ad}}$  measurements (red, left axis) of  $\text{Mn}_{1.82}\text{Cr}_{0.07}\text{Co}_{0.04}\text{Sb}_{1.07}$  around 287 K, done in a oscillated magnetic field of 5 T with a field-sweep rate of  $11 \text{ mTs}^{-1}$  (blue, right axis). The time range of changing field is highlighted in blue.

The sample-temperature shows a decrease in the range of increasing field and an increase in the range of decreasing field due to the inverse MCE. The temperature change during constant field is due to non-adiabatic conditions.  $\Delta T_{\text{ad}}$  is determined by taking this into account (chap. 3.4). The sample exhibits an inverse MCE with a  $|\Delta T_{\text{ad}}|$  between 1.8 K and 2.2 K, for increasing and decreasing field.  $|\Delta T_{\text{ad}}|$  increases with

further cycles due to non-adiabatic conditions causing the temperature of the setup to shift to higher values. At 287 K, a full AF/FI transformation cannot be induced by 5 T, and the sample remains in a mixed AF/FI state. With increasing temperature more amount of the AF phase can be transformed leading to an increase of  $|\Delta T_{\text{ad}}|$ .

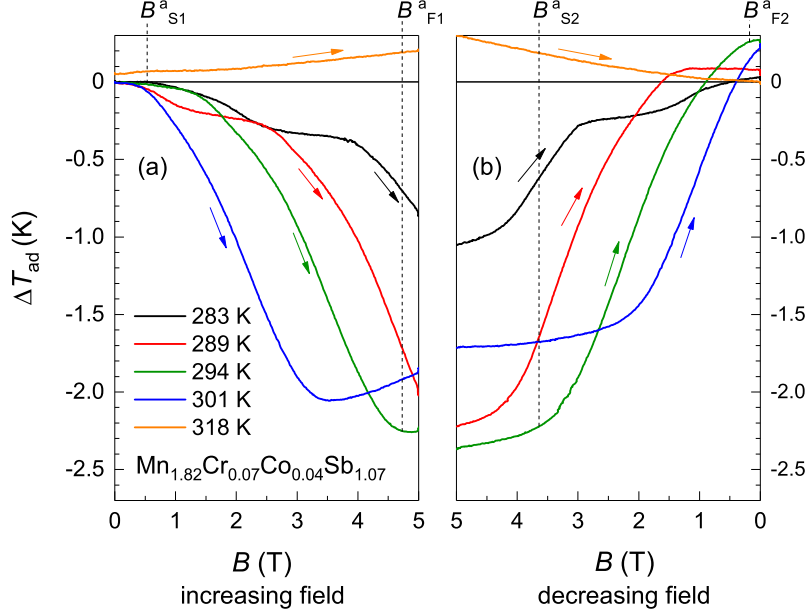


**Figure 4.21:** Field dependence of the  $\Delta T_{\text{ad}}$  measurements at 283 (black), 289 (red), 294 (green), 301 (blue), and 318 K (yellow). The left side shows  $\Delta T_{\text{ad}}$  for increasing magnetic field, the right side shows  $\Delta T_{\text{ad}}$  for decreasing magnetic field. The critical fields  $B_{\text{S1}}^a$ ,  $B_{\text{F1}}^a$ ,  $B_{\text{S2}}^a$ , and  $B_{\text{F2}}^a$  are shown for the data at 294 K.

Fig. 4.21 shows the field dependence of  $\Delta T_{\text{ad}}$  at 283 (black), 289 (red), 294 (green), 301 (blue), and 318 K (yellow). Figs. 4.21(a) and 4.21(b) shows  $\Delta T_{\text{ad}}$  for increasing fields and decreasing fields, respectively. Only the first cycle is shown. A negative  $\Delta T_{\text{ad}}$  is observed in the measurements at 301 K and below. At 318 K, an increase of  $\Delta T_{\text{ad}}$  up to 0.2 K is observed with increasing field. This is due to the conventional MCE in the FI phase. The same behavior can be observed for decreasing field (fig. 4.21(b)), the different values of  $\Delta T_{\text{ad}}$  are related to the temperature-drift, due to the non-adiabatic conditions. At 283 K, the  $\Delta T_{\text{ad}}$ -curve shows an increase to  $-0.8$  K. This  $\Delta T_{\text{ad}}$  is much smaller compared to the values obtained at higher temperatures since a field of 5 T is not sufficient to induce a full transformation from the AF to the FI state. The decrease of the field shows a decrease of  $\Delta T_{\text{ad}}$  back to zero due to the full reverse transformation to the AF phase. At 289 K,  $\Delta T_{\text{ad}}$  increases to  $-2.0$  K with increasing

field. The transformation is still not complete at 5 T. The decrease of the field shows a full reversal of the transformation to the AF state. The remaining  $\Delta T_{\text{ad}}$  at 0 T is due to temperature-drift. The measurements at 294 K show an increase of  $\Delta T_{\text{ad}}$  to  $-2.3$  K in the range  $B_{S1}^a \leq B \leq B_{F1}^a$  and a nearly constant  $\Delta T_{\text{ad}}$  for  $B_{F1}^a < B \leq 5$  T showing that the sample is fully transformed to the FI state. The decrease of the field shows a slight decrease in  $\Delta T_{\text{ad}}$  in the range  $5 \text{ T} \leq B < B_{S2}^a$  due to the conventional MCE in the FI phase and the temperature-drift. The further decrease of the field leads to the transformation from the FI state to the AF state ( $B_{F2}^a$ ). The remaining  $\Delta T_{\text{ad}}$  at 0 T is again due to the temperature-drift. At 301 K, the sample is in a mixed AF/FI state which leads to a lower  $\Delta T_{\text{ad}}$  ( $-2.1$  K) compared to the full transformation at 294 K. The decrease of  $\Delta T_{\text{ad}}$  above 3.5 T is due to the conventional MCE. The same effect is observed on decreasing field in the range  $5 \leq B \leq 3.5$  T. However, the slope of the  $\Delta T_{\text{ad}}$ -curves are different in this range. This is related to the conventional MCE which leads to a decrease in  $\Delta T_{\text{ad}}$  for increasing field and an increase for decreasing field. The superimposed drift leads then to the different slopes.

The  $\Delta T_{\text{ad}}$ -curves at 283 K and 289 K exhibit a shoulder-like feature at 3.5 T and 2 T, respectively, for increasing field. These features are not present in the measurements at 294 K and 301 K. For decreasing field, the feature can only be observed in the 283 K-curve, at about 2.5 T. The feature shifts to lower fields with increasing temperature. The effect is most likely correlated with the shoulders observed in the magnetization data in fig. 4.18, which is explained by the presence of a second Mn-Cr-Co-Sb phase with a different chemical composition. The effect disappears at higher temperatures, since the second phase has already transformed and only  $\Delta T_{\text{ad}}$  of the major phase is observed.

### 4.3.3 $\Delta T_{\text{ad}}$ in pulsed field with up to $1 \text{ kTs}^{-1}$ field-sweep rate

This section presents the  $\Delta T_{\text{ad}}$  measurements on  $\text{Mn}_{1.82}\text{Cr}_{0.07}\text{Co}_{0.04}\text{Sb}_{1.07}$  in pulsed magnetic fields \*. First we show results of the measurements in a pulsed field of 10 T with a field-sweep rate up to  $1 \text{ kTs}^{-1}$  in the range  $250 \leq T \leq 330 \text{ K}$ . Then we present  $\Delta T_{\text{ad}}$  measurements at constant temperature and different field-sweep rates (0.6 to  $1.6 \text{ kTs}^{-1}$ ). The setup and the field-profile with the corresponding field-sweep rates are given in chap. 3.4.

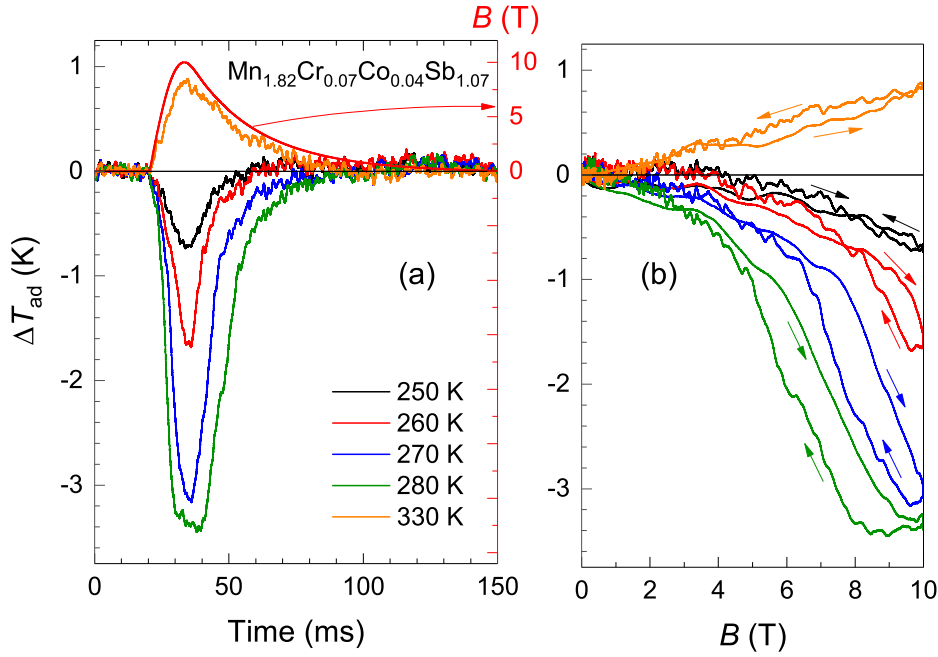


**Figure 4.22:** Direct  $\Delta T_{\text{ad}}$  measurements of  $\text{Mn}_{1.82}\text{Cr}_{0.07}\text{Co}_{0.04}\text{Sb}_{1.07}$  in 10 T pulsed magnetic fields with a field-sweep rate up to  $1 \text{ kTs}^{-1}$ . (a) Time dependence of  $\Delta T_{\text{ad}}$  at 250 (black), 260 (red), 270 (blue), 280 (green) and 330 K (yellow) (left axis). The magnetic pulse profile (red) is scaled with the right axis. (b) shows the field dependence of  $\Delta T_{\text{ad}}$ , the field-sweep direction is indicated by arrows.

Fig. 4.22(a) shows the time-dependent  $\Delta T_{\text{ad}}$  measurements at 250 (black), 260 (red), 270 (blue), 280 (green), and 330 K (yellow) (left axis). The data are taken during a field-pulse of 10 T. The field-profile is shown in red (right axis). The field increases

\*The measurements are performed at HLD-EMFL in collaboration with Dr. Catalina Salazar Mejia and Dr. Yuri Skourski.

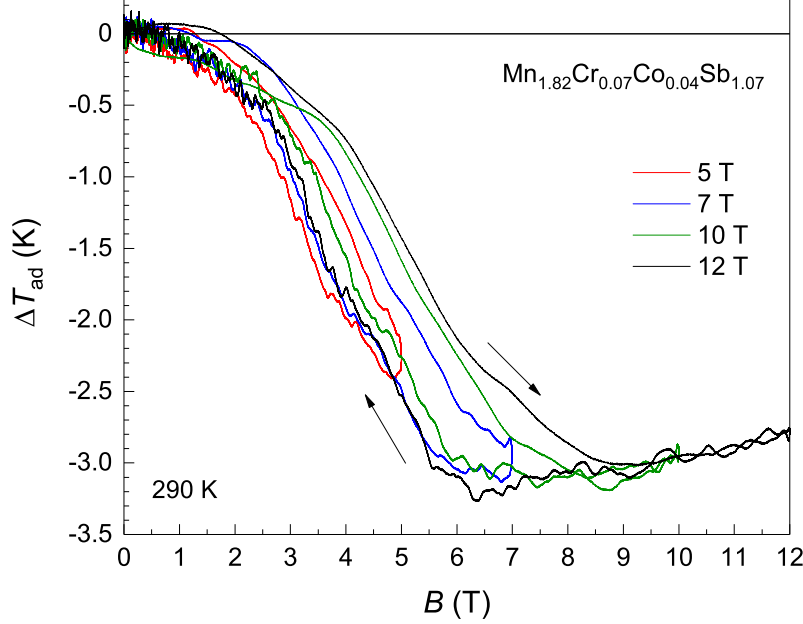
after 20 ms and reaches the maximum field of 10 T after 33 ms. The decrease of the field is slower than the increase and gives varying field-sweep rates. At 120 ms, the field reaches 0 T. Fig. 4.22(b) shows the  $\Delta T_{\text{ad}}$  measurements as a function of magnetic field. The direction of the field-sweep is indicated by arrows.

Fig. 4.22(a) shows for the measurements at  $T \leq 280$  K the inverse MCE, where  $\Delta T_{\text{ad}}$  is negative. At 330 K, the sample is in the FI phase and the measurements show a positive  $\Delta T_{\text{ad}}$  due to the conventional MCE. The shape of the  $\Delta T_{\text{ad}}$ -curve follows directly the profile of the magnetic field. For  $T \leq 280$  K, the maximum in  $\Delta T_{\text{ad}}$  decreases with decreasing temperature. The measurements at  $T \leq 270$  K have a peak shape, while at 280 K a small plateau in the range  $30 \leq t \leq 40$  ms is observed. The plateau is an indication that the AF/FI transformation is complete, and at lower temperatures, where this is not observed, it is incomplete. The approach of  $\Delta T_{\text{ad}}$  to zero for  $t > 120$  ms at all temperatures is a result of the fully reversible transformation to the AF state.

Fig. 4.22(b) shows the  $\Delta T_{\text{ad}}$ -measurements as a function of field. The conventional MCE at 330 K (yellow) is observed by the increase of  $\Delta T_{\text{ad}}$  with increasing field. The  $\Delta T_{\text{ad}}$ -curves for increasing and decreasing fields nearly coincide. This shows that there is very little lag between the thermocouple read-out and the instantaneous field.

At 280 K,  $\Delta T_{\text{ad}}$  shows an increase of  $-3.4$  K with increasing field up to 9.2 T. The slight decrease of  $\Delta T_{\text{ad}}$  above this field indicates that the transformation is complete and the sample shows a conventional MCE. The slow increase of  $\Delta T_{\text{ad}}$  in the field-range  $10 \geq B \geq 8.5$  T relates also to the conventional MCE of the FI phase. The further decrease of  $B$  shows a decrease of  $\Delta T_{\text{ad}}$ , due to the reverse transformation to the AF state. The  $\Delta T_{\text{ad}}$ -curve exhibits full reversibility. The different paths taken by the  $\Delta T_{\text{ad}}$ -curve for increasing and decreasing field is characteristic of a first-order transition, since the field has to overcome the hysteresis before the sample can undergo the reverse transformation. The deviation of about 0.5 T can be compared with the hysteresis in the magnetization study in chap. 4.3.1, fig. 4.18.  $M(T)$  shows a hysteresis of 2.5 K and a shift of  $T_i$  with a rate of  $-5 \text{ K T}^{-1}$ . Due to this, an increase in  $B$  by 0.5 T should be sufficient to overcome the hysteresis. This is roughly the difference between  $\Delta T_{\text{ad}}$ -curves for increasing and decreasing field. The same effect is also observed for the measurements at 270 and 260 K. The smaller values of  $\Delta T_{\text{ad}}$  at 10 T for these temperatures show, however, that the transformation is incomplete and the sample remains in a mixed AF/FI state. For the measurement at 250 K, the difference in the paths taken by the  $\Delta T_{\text{ad}}$ -curves cannot be properly resolved due to a smaller signal-to-noise ratio.





**Figure 4.23:** Direct  $\Delta T_{\text{ad}}$  measurements at 290 K in pulsed magnetic fields of 5 (red), 7 (blue), 10 (green), and 12 T (black), the field-sweep direction is indicated by arrows.

$\Delta T_{\text{ad}}$ -measurements at 290 K using different field-sweep rates are shown in fig. 4.23. The different field-sweep rates are achieved by applying field-pulses with different maximum fields of 5, 7, 10, and 12 T. Since the duration of the pulse is constant, an increase in the maximum field leads to an increase in the field-sweep rate (chap. 3.4 fig. 3.10). Before each measurement, the sample is cooled down to 240 K to ensure an initial AF state at the beginning of the measurement. All measurements show an increase in  $\Delta T_{\text{ad}}$ . The smaller maximum value of  $|\Delta T_{\text{ad}}|$  at the field-pulse of 5 T indicates that the transformation is not complete in this field. In contrast, the pulses of 7, 10, and 12 T show a saturation of the  $\Delta T_{\text{ad}}$ -curve at about  $-3$  K at 7 T. The measurements with 10 and 12 T pulses show further a decrease of  $\Delta T_{\text{ad}}$  in the field-range  $8 < B \leq 10$  T and  $9 < B \leq 12$  T, respectively, due to the conventional MCE in the FI phase. The effect can also be observed in the increase of  $\Delta T_{\text{ad}}$  with decreasing field in the range  $12 \geq B > 6.5$  T. The further decrease of the field leads to a decrease of  $\Delta T_{\text{ad}}$ , due to the reverse transformation to the AF state. This can be observed for all measurements and all pulses indicating a full reversal of the transformation. For  $\Delta T_{\text{ad}}$  values below  $-0.5$  K the signal-to-noise ratio becomes small, and a proper analysis is not possible.

The comparison of the  $\Delta T_{\text{ad}}$ -curves in different magnetic fields shows that the curves deviate in the range of increasing  $\Delta T_{\text{ad}}$  ( $1 \leq B \leq 8 \text{ T}$ ), while the curves more or less coincide in the range of decreasing  $\Delta T_{\text{ad}}$  ( $6.5 \geq B \geq 0 \text{ T}$ ). The deviation can be explained by the different field-sweep rates of the pulses and a delay in the temperature measurement. Fig. 3.10 (chap. 3.4) shows different field-sweep rates in the increasing field-direction for different maximum fields. On the other hand, the field-sweep rates for decreasing field ( $B < 6 \text{ T}$ ) is equivalent for all pulses. This explains why the curves in fig. 4.23 coincide in the range of decreasing  $\Delta T_{\text{ad}}$  ( $6.5 \geq B \geq 0 \text{ T}$ ). The increase of the field sweep-rates also cause an increase in the delay of the temperature reading. A small delay was already observed in fig. 4.22(b) in the measurements at 330 K indicating that the effect will become more dominant at increasing field-sweep rates. In the measurements with a 12 T-pulse the increase in the delay of the temperature reading leads also to a spreading of the  $\Delta T_{\text{ad}}$ -curve in the range between 6.5 K and 8 T.

#### 4.3.4 Comparison of $\Delta T_{\text{ad}}$ at different field-sweep rates

In this section, we compare  $\Delta T_{\text{ad}}$  presented in chap. 4.3.2 and 4.3.3 for the different field-sweep rates.

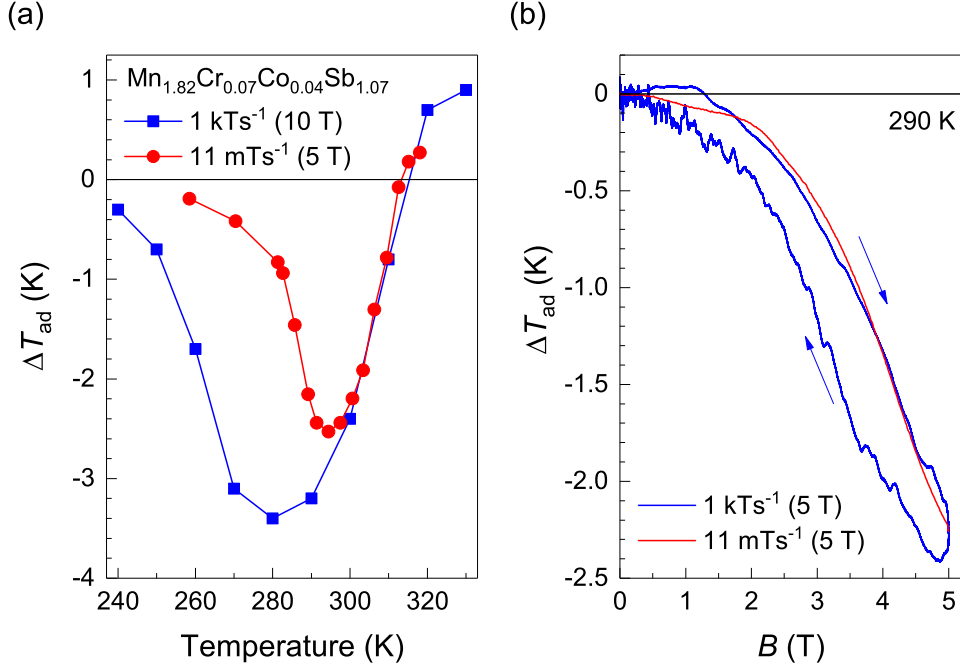


**Figure 4.24:** (a) Temperature dependence of maximum  $\Delta T_{\text{ad}}$  of the measurements in an applied field of 5 T with a field-sweep rate of  $11 \text{ mTs}^{-1}$  (red) and in pulsed field (10 T) with a field-sweep rate up to  $1 \text{ kTs}^{-1}$  (blue). (b) Field-dependent  $\Delta T_{\text{ad}}$  measurements at 290 K with an applied field of 5 T. The measurements with  $11 \text{ mTs}^{-1}$  is shown in red, the measurement in pulsed field with  $0.6 \text{ kTs}^{-1}$  is shown in blue.

Fig. 4.24(a) shows the maximum  $\Delta T_{\text{ad}}$  of the measurements using  $11 \text{ mTs}^{-1}$  (red, chap. 4.3.2) and  $1 \text{ kTs}^{-1}$  (blue, chap. 4.3.3) as a function of temperature. For the field-sweep rate up to  $1 \text{ kTs}^{-1}$  in pulsed field up to 10 T, a maximum  $\Delta T_{\text{ad}}$  of  $-3.4 \text{ K}$  is observed at 280 K. The field-dependent  $\Delta T_{\text{ad}}$ -curve (fig. 4.22) shows a full AF/FI transformation at this temperature. Fig. 4.24(a) shows a decrease of  $\Delta T_{\text{ad}}$  below 280 K indicating that the transformation is not complete and the sample remains in a mixed AF/FI state at 10 T. Above 280 K,  $\Delta T_{\text{ad}}(T)$  decreases also, this is due to the temperature which is too close to  $T_i$  and the sample is in a mixed AF/FI state before the field is applied. Above  $T_i = 306 \text{ K}$ , the sample is in the FI state, and a positive  $\Delta T_{\text{ad}}(T)$  is observed due to the conventional MCE.

For the field-sweep rate of  $11 \text{ mTs}^{-1}$  with a field of 5 T, a maximum value of  $-2.5 \text{ K}$  is observed at 294 K. The lower value shows that the field of 5 T is not sufficient to induce a complete AF/FI transformation. This is also the reason for the lower  $\Delta T_{\text{ad}}$  below 294 K compared to the measurements at  $1 \text{ kTs}^{-1}$ . In the range  $294 < T < 306 \text{ K}$ , the  $\Delta T_{\text{ad}}$ -curves at  $11 \text{ mTs}^{-1}$  (5 T) and  $1 \text{ kTs}^{-1}$  (10 T) coincide. In this case, the sample is in a mixed AF/FI state and both fields are sufficient to transform the sample to the FI state. Applying a 5 T-field above  $T_i$  leads to a conventional MCE and a  $\Delta T_{\text{ad}}$  of about 0.3 K. The effect increases when a higher field (10 T) is applied.

Fig. 4.24(b) shows field-dependent  $\Delta T_{\text{ad}}$  measurements at 290 K for an applied field of 5 T and a field-sweep rate of  $11 \text{ mTs}^{-1}$  and  $0.6 \text{ kTs}^{-1}$ . The  $\Delta T_{\text{ad}}$ -curves coincide particularly well in the range  $2 \leq B \leq 5 \text{ T}$  showing that the transition-dynamics can follow both sweep-rates. The small deviation below 2 T can be related to non-adiabatic conditions or small differences in the temperature calibration between the two measurements. In this respect, the narrow hysteresis and a reversible MCE of 2.5 K, which is also obtained in fast field-sweep rates make  $\text{Mn}_{1.82}\text{Cr}_{0.07}\text{Co}_{0.04}\text{Sb}_{1.07}$  an interesting material for magnetocaloric cooling at 300 K.

## 4.4 Magnetic properties of ferromagnetic nano-precipitates in decomposed off-stoichiometric NiMnIn

This chapter presents studies on the magnetic properties of Heusler nano-precipitates obtained by decomposing  $\text{Ni}_{50}\text{Mn}_{45.1}\text{In}_{4.9}$ . Annealing off-stoichiometric Ni-Mn-In alloys leads to decomposition into AF  $\text{Ni}_{50}\text{Mn}_{50}$  and FM stoichiometric  $\text{Ni}_{50}\text{Mn}_{25}\text{In}_{25}$  Heusler (see chap. 2.2.1).

Previous studies on annealed  $\text{Ni}_{50}\text{Mn}_{45.1}\text{In}_{4.9}$  have shown the presence of a FM phase [Cak16, Ç17b]. The  $M(B)$ -curve of an annealed  $\text{Ni}_{50}\text{Mn}_{45.1}\text{In}_{4.9}$  sample exhibits a magnetic hysteresis which is absent in the measurements on the initial state (non-annealed) of the sample. It was further shown, that the presence of a magnetic field during annealing shifts the magnetic hysteresis vertically. This vertical shift was explained by a shell-ferromagnetic nano-precipitates model. The model is explained as the formation of nano-precipitates which have a pinned, hard-magnetic shell and a soft-magnetic core; all embedded in an AF matrix [Cak16, Ç17b]. The magnetization of the shell is pinned along the magnetic field-direction during annealing. After annealing, the magnetization of the shells remains pinned, while the magnetization of the core can rotate. The pinned shell leads to vertically shifted  $M(B)$ -curves. The effect of shell-ferromagnetic nano-precipitates can be seen in reference [You16]

Fig. 4.25 shows the field-dependent magnetization of the initial state of  $\text{Ni}_{49.6}\text{Mn}_{45.5}\text{In}_{4.9}$  (red) and the annealed state (blue) with nano-precipitates. The sample was annealed at 650 K for 1 hour in an applied field of 4.5 T. The preparation is given in detail in chap. 3.1. The measurements are performed at 300 K in the field-range  $-5 \leq H \leq 5$  T (inset fig. 4.25). The initial state of the sample is AF and exhibits a linear dependence of the magnetization with field, with a susceptibility  $\chi$  of  $1.21 \times 10^{-5} \text{ Am}^2\text{kg}^{-1}\text{T}^{-1}$ . The low field region,  $-0.7 \text{ T} \leq B \leq 0.7 \text{ T}$ , shows however a slight change of the slope close to zero-field, which is related to MnO inhomogeneities observed in magnetic resonance measurements [Sch17a].

$M(B)$  of the annealed sample (blue) shows a vertically shifted magnetic hysteresis loop in the low field region  $-0.2 \text{ T} \leq B \leq 0.2 \text{ T}$  and a linear behavior of the magnetization for higher fields (inset fig. 4.25). The magnetic hysteresis indicates the formation of FM precipitates. The  $M(B)$ -curve of the annealed  $\text{Ni}_{49.6}\text{Mn}_{45.5}\text{In}_{4.9}$  alloy is similar to previous measurements [Cak16, Ç17b]. The comparison of the slopes of the initial and decomposed samples show an increase by 7 % for the decomposed sample. The increase in the susceptibility ( $\chi = 1.30 \times 10^{-5} \text{ Am}^2\text{kg}^{-1}\text{T}^{-1}$ ) relates to the formation of AF  $\text{Ni}_{50}\text{Mn}_{50}$  phase having a five times larger susceptibility than the initial  $\text{Ni}_{49.6}\text{Mn}_{45.5}\text{In}_{4.9}$  alloy [Kas59]. The green  $M(B)$ -curve in fig. 4.25 shows the magnetization of the decomposed alloy without the AF matrix. This is done by subtracting the linear contribution in  $M(B)$ , which is related to the AF matrix. The  $M(B)$ -curve is vertical shifted by  $M_{\text{shift}} = 4.6 \times 10^{-2} \text{ Am}^2\text{kg}^{-1}$ , and has a coercive field  $H_C$  of 17 mT.

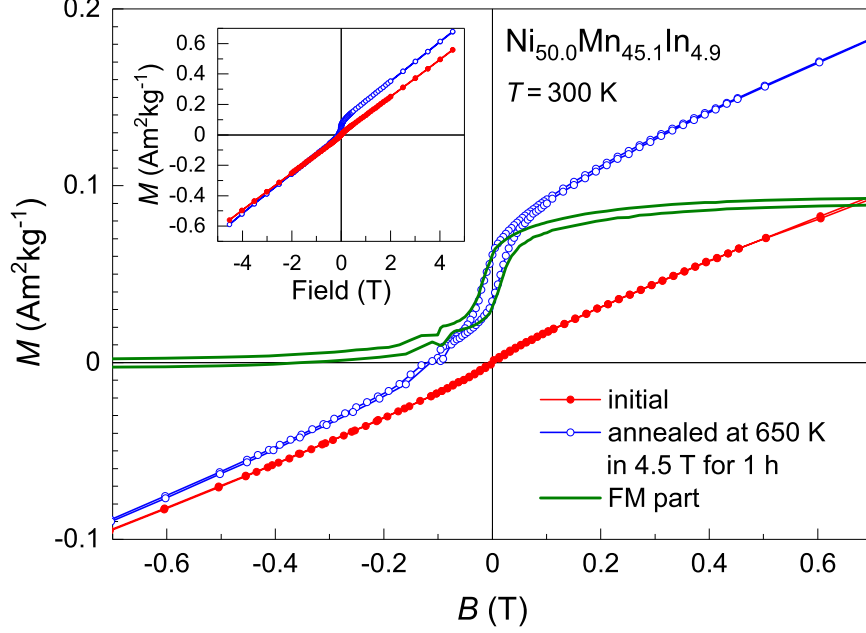


**Figure 4.25:** Field-dependent magnetization of  $\text{Ni}_{49.6}\text{Mn}_{45.5}\text{In}_{4.9}$  at 300 K for the initial state (red) and decomposed state, annealed at 650 K in 5 T for 1 hour (blue). The field-dependent magnetization of the FM precipitates after subtraction of the AF background is shown in green. The inset shows the full field-range of the measurement [Sch17a].

A remanence of  $M_{\text{R}}^{\text{upper}} = 6.1 \times 10^{-2} \text{ Am}^2\text{kg}^{-1}$  and  $M_{\text{R}}^{\text{lower}} = 3.1 \times 10^{-2} \text{ Am}^2\text{kg}^{-1}$  are observed for the upper and lower branches. The soft FM phase nearly saturates at about 0.6 T, whereas the upper and lower hysteresis branches do not overlap at high fields, which indicates that a complete saturation of the sample requires a field larger than 5 T. The magnetization above 0.6 T and below  $-0.6 \text{ T}$  can be used to estimate the saturation magnetization of the soft FM part to be  $4.5 \times 10^{-2} \text{ Am}^2\text{kg}^{-1}$ .  $M(B)$  measurements at 10 K exhibits a saturation magnetization of  $0.125 \text{ Am}^2\text{kg}^{-1}$ . Assuming that the soft FM part of the sample has a stoichiometric  $\text{Ni}_{50}\text{Mn}_{25}\text{In}_{25}$  composition with a saturation magnetization of  $80 \text{ Am}^2\text{kg}^{-1}$  [Kre06a], the amount of FM phase of the  $\text{Ni}_{50}\text{Mn}_{25}\text{In}_{25}$  precipitate can be estimated to be about 0.16 %.

To study the complete magnetization of the FM nano-precipitate,  $M(B)$  measurements in a field-range  $-14 \leq B \leq 14 \text{ T}$  are done. The results are discussed in chap. 4.4.1. Additionally, FMR measurements are performed to study the magnetic interactions of the precipitate and the AF matrix. The results are given in chap. 4.4.2.

#### 4.4.1 Field-dependent magnetization of nano-precipitates

Here we discuss the results of field-dependent magnetization measurements on annealed  $\text{Ni}_{50}\text{Mn}_{45.1}\text{In}_{4.9}$ . The measurements are performed in a PPMS (chap. 3.3.1) in magnetic fields up to 14 T \*.

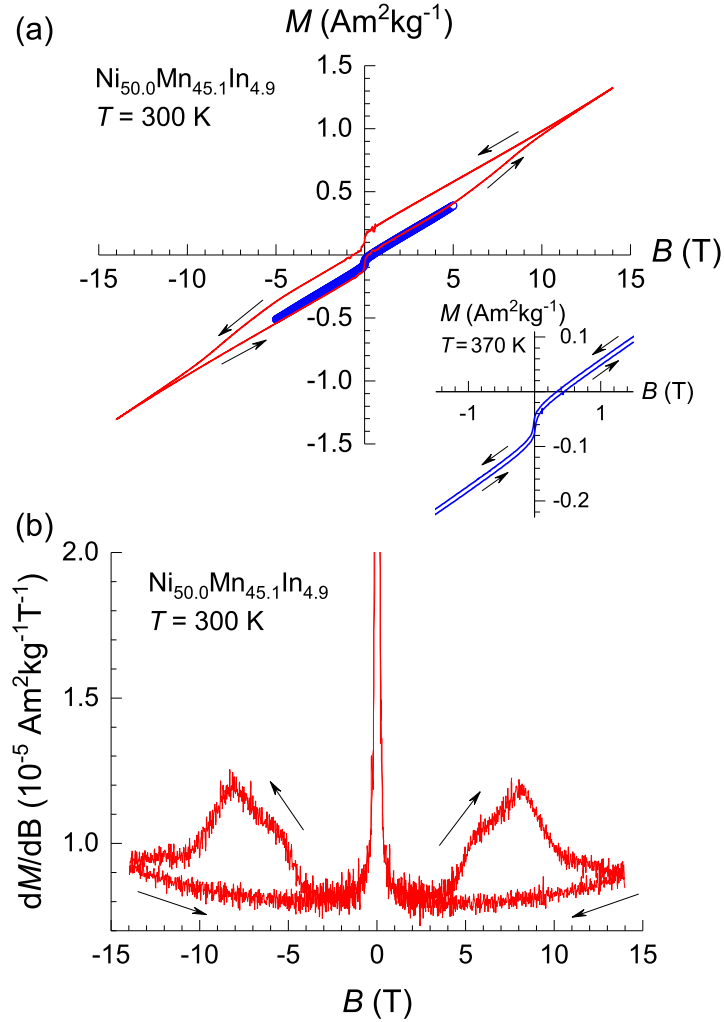
A  $\text{Ni}_{50}\text{Mn}_{45.1}\text{In}_{4.9}$  ingot was used in preparing a sample of 5.6 mg and dimensions  $1.45 \times 1.05 \times 0.50$  mm. The sample was annealed in the SQUID magnetometer in 4.5 T at 650 K for 17 hours (chap. 3.3.2).

Fig. 4.26 shows the field-dependent magnetization and its derivative of the annealed sample at 300 K (red) in the field-range of  $-14 \leq B \leq 14$  T. The direction of field-sweep is indicated by arrows. The red  $M(B)$ -curve (fig. 4.26(a)) is nearly closed. The incomplete closure of the curve can also be observed in the derivative  $dM(B)/dB$  in fig. 4.26(b), where differences of the curve with increasing and decreasing field occur around  $\pm 14$  T. The figure also shows an increase of  $dM(B)/dB$  when a field of  $\pm 5$  T is reached. The maximum is reached around  $\pm 8$  T, after which further increasing the field leads to a gradual decrease. In the case of  $M(B)$ -measurements in the range  $-5 \leq B \leq 5$  T (fig. 4.26(a), blue), a minor loop is observed in the inset for  $-1 \leq B \leq 1$  T. This is similar to previous measurements in this field-range [Cak16, Ç17b]. Here, a negative shift of the minor loop is observed because the sample was previously magnetized in  $-14$  T. The minor loop lies on the lower hysteresis branch of the measurements done in the range  $-14 \leq B \leq 14$  T (red).

The susceptibility  $\chi$  of the AF matrix is determined by the linear fit to  $M(B)$  for decreasing field case in the range between 7 T and 1 T giving  $\chi = 8.19 \times 10^{-6} \text{ Am}^2\text{kg}^{-1}\text{T}^{-1}$ . The subtraction of the AF contribution leads to the  $M(B)$ -curve related to the FM part of the precipitates (fig. 4.27). The direction of magnetic field-sweep is indicated by arrows. Even the  $M(B)$ -curve for  $-14 \leq B \leq 14$  T is vertically shifted. This shows that the magnetization is still not saturated in 14 T. The bending of  $M(B)$  at high-fields (10 to 14 T), is due to non-linear behavior of the coupled FM and AF parts. At positive high-field, the soft FM core and the hard FM shell are aligned so that  $M_S^{\text{upper}} = 0.18 \text{ Am}^2\text{kg}^{-1}$ . Below 0.3 T, the magnetization of the soft FM core starts to rotate. The magnetization is reversed at  $-0.3$  T. The difference in magnetization between 0.3 T and  $-0.3$  T is  $0.136 \text{ Am}^2\text{kg}^{-1}$ . Half of this value is the saturation magnetization of the soft FM core,  $M_S^{\text{core}} = 0.068 \text{ Am}^2\text{kg}^{-1}$ . The remanent magnetization corresponds to the remanence of the hard FM phase,  $M_{r+}^{\text{shell}} = 0.114 \text{ Am}^2\text{kg}^{-1}$ . The further reversal of the field shows an increase in  $M(B)$  above a field of about  $-4$  T. The change of  $M(B)$  corresponds to the rotation of the hard FM shell. The lower branch exhibits as the upper branch a rotation of the soft FM core in the range  $-0.3 \leq B \leq 0.3$  T. The magnetization change in this range is again  $0.136 \text{ Am}^2\text{kg}^{-1}$  so that  $M_S^{\text{core}}$  is well determined as  $0.068 \text{ Am}^2\text{kg}^{-1}$ . At 0 T, for the lower branch,  $M_{r-}^{\text{shell}} = -0.074 \text{ Am}^2\text{kg}^{-1}$ . The half of the difference of  $M_{r+}^{\text{shell}}$  and  $M_{r-}^{\text{shell}}$  shows that the  $M(B)$ -curve is vertically

---

\*The measurements are performed by Dr. Tino Gottschall at the Technical University of Darmstadt.



**Figure 4.26:** (a) Field-dependent magnetization of decomposed  $\text{Ni}_{49.6}\text{Mn}_{45.5}\text{In}_{4.9}$  (red) at 300 K measured in the field-range  $-14 \leq B \leq 14$  T. The blue curve shows the minor loop of  $M(B)$  in the field-range  $-5 \leq B \leq 5$  T the sample was previously magnetized in  $-14$  T. The inset shows the vertically shifted minor loop in the range  $-1 \leq B \leq 1$  T. (b) shows the derivative of the magnetization  $dM(B)/dB$ . The direction of field-sweep is indicated by arrows [Sch17b].



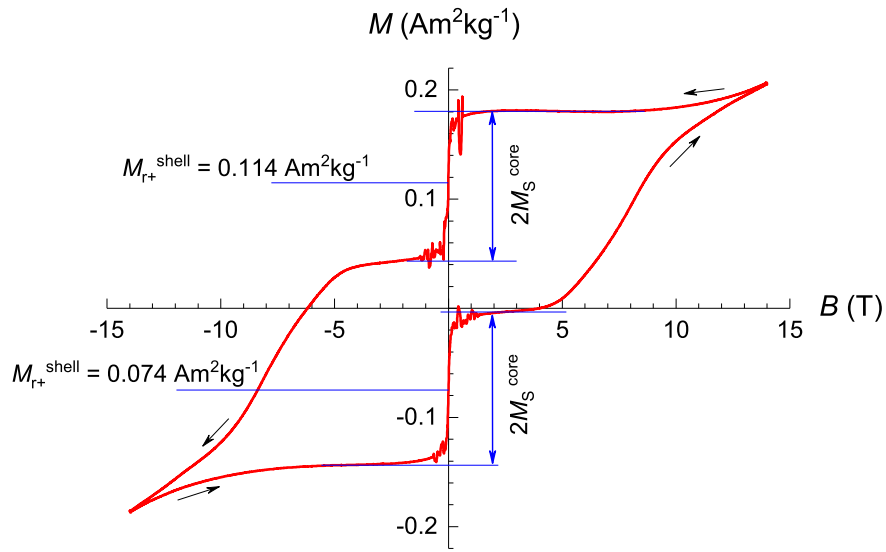


**Figure 4.27:** Field-dependent magnetization of the FM precipitates in decomposed  $\text{Ni}_{49.6}\text{Mn}_{45.5}\text{In}_{4.9}$  at 300 K, the AF matrix is subtracted. The direction of field-sweep is indicated by arrows [Sch17b].

shifted by  $0.020 \text{ Am}^2\text{kg}^{-1}$  related to the remanent pinning of the FM shell.

The saturation magnetization of  $\text{Ni}_{50}\text{Mn}_{25}\text{In}_{25}$  is  $75 \text{ Am}^2\text{kg}^{-1}$  [Kre06a]. Assuming that the precipitates also have this composition, the concentration of the soft FM phase can be estimated to be about 0.24%. The concentration is calculated from the ratio of the saturation magnetization of the precipitates,  $0.18 \text{ Am}^2\text{kg}^{-1}$  with respect to the saturation magnetization of  $\text{Ni}_{50}\text{Mn}_{25}\text{In}_{25}$ .

The magnetization measurements in fig. 4.27 give evidence for the presence of hard and soft FM phases. To understand the coupling of the hard and soft FM phases in more detail FMR measurements are performed. The results are given in chap. 4.4.2.

#### 4.4.2 Magnetic resonance of nano-precipitates in the field-range up to 11.5 T

The magnetization measurements in fields up to 14 T indicate the presence of a hard and soft FM phases. To provide further evidence we carry out FMR measurements in external fields up to 12 T. The setup is described in chap. 3.3.2 and fig. 3.5c) shows the assembling of the annealed  $\text{Ni}_{50}\text{Mn}_{45.1}\text{In}_{4.9}$  alloy. A microwave frequency of 9.048 GHz and a field-modulation of 16 mT and 123 Hz were used in the measurements \*.

Fig. 4.28(a) shows the  $\partial(\text{FMR}_{\text{abs}})/\partial B$  of annealed  $\text{Ni}_{50}\text{Mn}_{45.1}\text{In}_{4.9}$  at 300 K in the field-range  $-11.5 \leq B \leq 11.5 \text{ T}$ . Fig. 4.28(b) shows a magnification of the spectra for  $-1.5 \leq B \leq 1.5 \text{ T}$ . The spectrum with field-sweep from 0 T to 11.5 T is marked as 1 (red). Afterwards, the field is decreased from 11.5 T to 0 T (spectrum 2, red). The same measurement is performed in the reverse field-direction (3, blue) and (4, green). The direction of field-sweep is indicated with arrows. All spectra show two resonances; a major FMR at  $\pm 0.15 \text{ T}$  and a minor ESR at  $\pm 0.34 \text{ T}$ . The resonance fields are independent of the field-sweep direction. The ESR signal at 0.34 T is related to the PM MnO impurities at the surface [Sch17a]. The reason for the increase for the intensity of the ESR for the spectrum 1 and 2, and 3 and 4 is most probably related to the over-modulation of the signal. The major FMR at about  $\pm 0.15 \text{ T}$  is due to the FM precipitates. The resonance position is in good agreement with the magnetization value for  $\text{Ni}_{50}\text{Mn}_{25}\text{In}_{25}$  [Kre06a]. The shape of the resonance describes the polycrystalline morphology of the sample. The FMR signal from the various crystallographic orientations superimpose and give a distribution for the FMR. Assuming a cubic anisotropy for the precipitates, using the magnetization value for  $\text{Ni}_{50}\text{Mn}_{25}\text{In}_{25}$  and the line-width of 247 mT, we obtain a value of  $4 \times 10^4 \text{ Jm}^{-2}$  for the crystalline anisotropy. Before the first spectrum (1, black) was taken, the sample was saturated in  $-11.5 \text{ T}$ . The further increase of the field above 6 T shows additional FMR absorptions (inset fig. 4.28 above). These absorptions are most probably related to the rim of the precipitate coupled to the surrounding  $\text{Ni}_{50}\text{Mn}_{50}$  matrix. The changes

---

\*The measurements are performed together with Dr. Detlef Spoddig and Dr. Ralf Meckenstock.

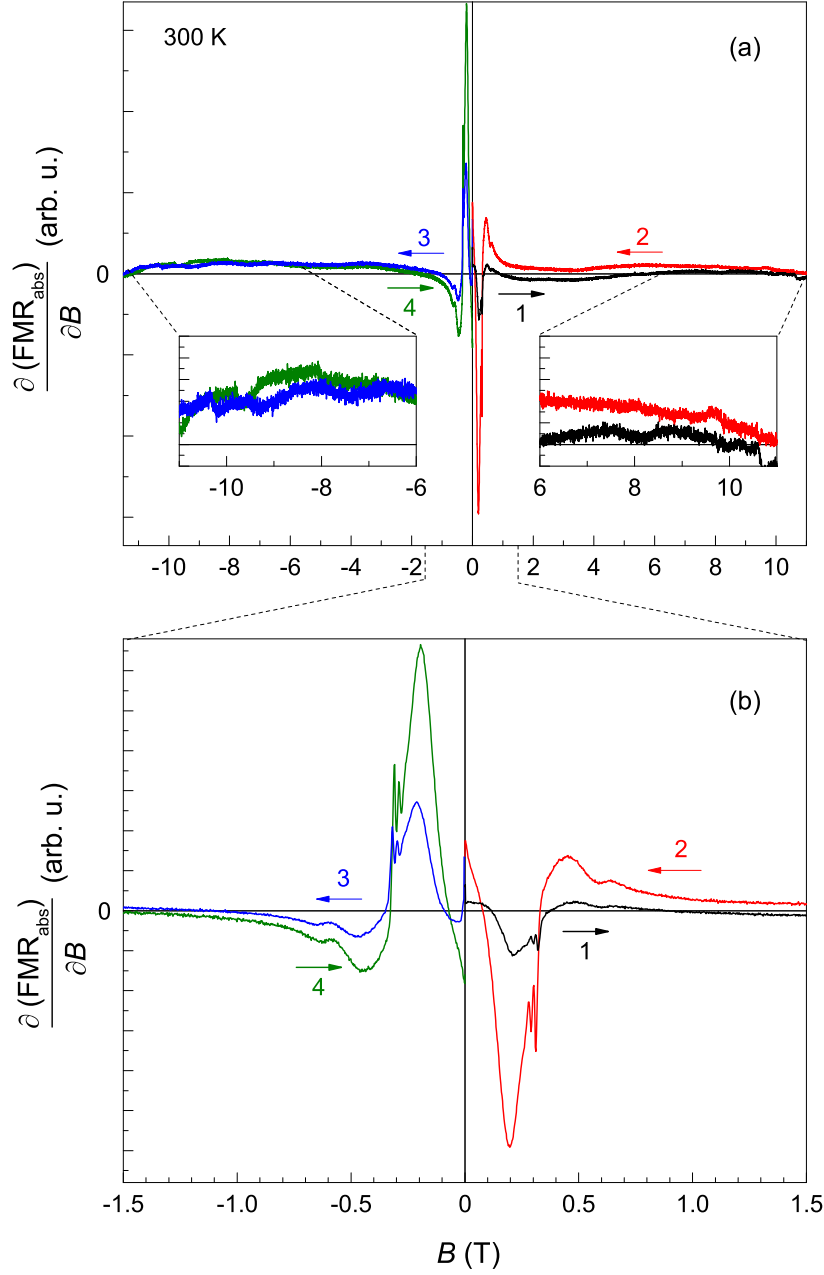


**Figure 4.28:** Bidirectional field-dependent FMR absorption derivative  $\partial(\text{FMR}_{\text{abs}})/\partial B$  of decomposed  $\text{Ni}_{49.6}\text{Mn}_{45.5}\text{In}_{4.9}$  at 300 K. (a) Full spectrum with field-range  $-11.5 \leq B \leq 11.5$  T, the insets show a magnification of the signal in range  $6 \leq B \leq 10$  T. (b) Magnification of the full spectrum in the range  $-1.5 \leq B \leq 1.5$  T. The direction of field-sweep is indicated by arrows [Sch17b].

in  $\partial(\text{FMR}_{\text{abs}})/\partial B$  are detected in the range  $6 \leq B \leq 10$  T, which reflect to changes in the hysteresis-curve in fig. 4.27. At the maximum field of 11.5 T, the hard FM is nearly in full alignment along the field-direction. The decrease of the field (spectrum 2, red) shows an increase of the intensity of the FMR around 0.15 T compared to the non-aligned case of spectrum (1, black), arising from the hard FM phase. This supports the picture that the precipitates is composed of a hard and soft FM phase. The same effect is observed for the spectrum in the reverse field-direction (3, blue and 4, green), where FMR occurs  $-0.15$  T. The changes of  $\partial(\text{FMR}_{\text{abs}})/\partial B$  above 6 T is due to the alignment of the hard FM phase and are similar to these in the positive field-direction. A comparison of spectra 2 (red) and 4 (green) shows that the spectra are point symmetric to the origin. In contrast to, spectra 1 (black) and 2 (blue) are not symmetric, since spectra 1 (black) is obtained with the sample in the initial state. Integrating spectra 3 and 4 give a ratio of 1 : 2.4 for the intensities. Since FMR probes the magnetization of the sample a similar ratio is expected in the magnetization measurements in fig. 4.27. Actually, a ratio of 1 : 2.7 is observed between the magnetization of the soft FM phase ( $M_S^{\text{core}} = 0.068 \text{ Am}^2\text{kg}^{-1}$ ) and the magnetization of the hard FM phase  $M(-2 \text{ T})^{\text{upper}} - M(-2 \text{ T})^{\text{lower}} = 0.184 \text{ Am}^2\text{kg}^{-1}$ .  $M(-2 \text{ T})^{\text{upper}} - M(-2 \text{ T})^{\text{lower}} = 0.184 \text{ Am}^2\text{kg}^{-1}$  is the difference of the magnetization in the upper and lower hysteresis branch at  $B = -2$  T ( $M(-2 \text{ T})^{\text{upper}} = 0.042 \text{ Am}^2\text{kg}^{-1}$  and  $M(-2 \text{ T})^{\text{lower}} = -0.142 \text{ Am}^2\text{kg}^{-1}$ ). A similar ratio is found if we assume a precipitate-size of 2 nm, in this case, the surface-to-volume ration is 1 : 2.

This supports the interpretation that the rim of the precipitate is only contributing to  $\partial(\text{FMR}_{\text{abs}})/\partial B$  if the hard and soft FM phases are aligned parallel. Bidirectional FMR measurements along in the field-range  $-1.5 \leq B \leq +1.5$  are done to validate this interpretation. The sample was magnetized in  $-12$  T to ensure a defined initial state. Fig. 4.29 shows the bidirectional FMR spectrum starting from  $-1.5$  T. The directions of the field-sweep are indicated by arrows. The intensity of the different field-sweep directions are the same since this field is not strong enough to align the hard FM phase along the field-direction and only the soft FM phase contribute to  $\partial(\text{FMR}_{\text{abs}})/\partial B$ . This supports the interpretation that the rim of the precipitate is contributing to the FMR signal only if the coupling to the surrounding is in the right field-direction.

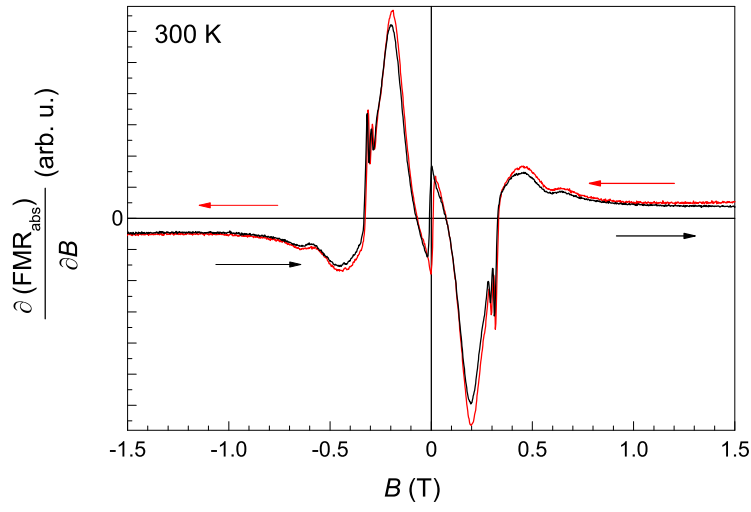


**Figure 4.29:** Bidirectional field-dependent FMR absorption derivative  $\partial(\text{FMR}_{\text{abs}})/\partial B$  of decomposed  $\text{Ni}_{49.6}\text{Mn}_{45.5}\text{In}_{4.9}$  at 300 K in the range  $-2 \leq B \leq 2$  T. The sample was saturated in  $-12$  T before performing the measurement. The direction of field sweep is indicated by arrows [Sch17b].

To summarize the results of the magnetic resonance studies we could proof the magnetization value of  $\text{Ni}_{50}\text{Mn}_{25}\text{In}_{25}$  and estimate a crystalline anisotropy of  $4 \times 10^4 \text{ Jm}^{-2}$ . High field FMR measurements up to 11.5 T verified the existence of a strong coupling of the rim of the precipitates with the surrounding  $\text{Ni}_{50}\text{Mn}_{50}$  matrix. The measurements further proof that the magnetization of rim and soft FM phase are the same.

In conclusion, the annealing temperature of 650 K is an crucial parameter for the preparation of shell-ferromagnetic nano-precipitates in annealed  $\text{Ni}_{50}\text{Mn}_{45.1}\text{In}_{4.9}$ . The effect of shell-ferromagnetim shown in chap. 4.4.2 and 4.4.1 can only observed for nano-precipitates with a size below 3 nm, since the effect is related to the surface of the precipitates, and therefore the surface-to-volume ratio has to be around 1:2. The increase of the precipitate-size decreases the surface-to-volume ratio, the magnetic behaviors of the volume dominate and the effect of shell-ferromagnetim can not be detected anymore [Ç17b]. The two investigated sample are annealed at 650 K for 1 hour (fig. 4.25) and 17 hours (fig. 4.27). Both samples show a size of the nano-precipitates of about 3 nm [Din18], which is close to the detection limit of XRD [O'C15]. The longer annealing duration therefore just increases the amount of nano-precipitates but has no influence on the size of the precipitates [Din18]. The increase of the annealing temperature to 700 and 750 K increases the size of the precipitates, which was shown by previous XRD studies [Cak16, Kre16, Ç17a]. The restricted size of the precipitates for 650 K may explained by the  $\text{Ni}_{50}\text{Mn}_{50}$  matrix acting as a barrier for the diffusion of the In atoms. The  $\text{Ni}_{50}\text{Mn}_{25}\text{In}_{25}$  precipitates can only grow if In diffuses form the base  $\text{Ni}_{50}\text{Mn}_{45.1}\text{In}_{4.9}$  alloy through the  $\text{Ni}_{50}\text{Mn}_{50}$  matrix. If the thermal energy is not high enough to overcome the  $\text{Ni}_{50}\text{Mn}_{50}$  barrier the precipitates stop growing.

## 4.5 Conclusion

The results of investigations on the field-sweep rate dependent phenomena of MCEs have been presented in the material-classes  $\text{Mn}_3\text{GaC}$  antiperovskites and Mn-Cr-Co-Sb pnictides, and the magnetic properties of a  $\text{Mn}_3\text{GaC}$  single crystal and ferromagnetic nano-precipitates in decomposed off-stoichiometric Ni-Mn-In Heusler alloy are presented.

The AF/FM first-order transition in  $\text{Mn}_3\text{GaC}$  exhibits a narrow thermal hysteresis of 5 K which can be induced by a magnetic field which shifts the transformation temperature by  $dT_i/dB = -5.7 \text{ K T}^{-1}$ . The large shift and the narrow hysteresis enable a fully reversible transformation with a cyclically applied field of 2 T. The field-induced transformation leads to a  $\Delta S$  of  $13 \text{ J kg}^{-1} \text{ K}^{-1}$  and a  $\Delta T_{\text{ad}}$  of 4.7 K, which are also fully reversible making this material interesting for magnetocaloric refrigeration below room temperature. Adiabatic magnetization measurements in pulsed fields have shown that the magnetization dynamics can follow the fast field-sweep rates of  $1.3 \text{ Ts}^{-1}$ . However, the comparison of isothermal and adiabatic critical fields exhibit a super-cooling for the start of the transformation at fast field-sweep rates. This shows that the nucleation process is influenced by the magnitude of the field-sweep rate.  $\Delta T_{\text{ad}}$  measurements at different field-sweep rates show that the structural transformation of the first-order AF/FM transformation cannot follow a rate of  $1 \text{ Ts}^{-1}$  and gives a lower value for  $\Delta T_{\text{ad}}$  compared to lower rates. This is in contrast to the results of the adiabatic magnetization measurements in pulsed fields and can be explained by different time-responses of the magnetic and structural transformation. The slow structural responses can be explained by a volume change of 0.5% occurring at the isostructural AF/FM transition causing stress and strain in the sample [C14b]. This influences the MCE. However, a rate of  $1 \text{ Ts}^{-1}$  corresponds to a frequency of 500 Hz for a cyclically applied field of 2 T. This is far above the operating frequency of magnetic refrigerators (1 – 10 Hz) so that  $\text{Mn}_3\text{GaC}$  is a potential magnetocaloric refrigerant at low temperatures.

The first studies on a  $\text{Mn}_3\text{GaC}$  single crystal have shown that the transition temperature, width, and  $dT_i/dB$  are comparable with those of polycrystalline samples. This shows that these parameters do not depend on the sample morphology. FMR studies and simulations on the single crystal show that the  $\{111\}$ -direction is the magnetic easy-axis and yield a MCAE of  $K_4 = -5.49 \text{ kJ m}^{-3}$ . The small value of  $K_4$  can be also the reason for the small hysteresis [Toh03]. Therefore, the magnetic anisotropy in  $\text{Mn}_3\text{GaC}$  depends mainly on the shape of the sample which can be optimized for magnetocaloric refrigeration devices.

The Cr and Co-doped  $\text{Mn}_2\text{Sb}$  pnictides undergo a transformation from the AF to the FI state. The first-order transition is close to room temperature. The transition temperature decreases with increasing applied field with  $dT_i/dB = -5 \text{ K T}^{-1}$  and has a narrow thermal hysteresis of 2.5 K. The material shows a reversible inverse MCE with a  $\Delta S = 4.8 \text{ J kg}^{-1} \text{ K}^{-1}$  and a  $\Delta T_{\text{ad}} = -2.5 \text{ K}$  in a field change of 5 T. The narrow

hysteresis and the sufficient  $\Delta T_{\text{ad}}$  in 5 T field makes the material a possible candidate for magnetocaloric refrigeration.

$\Delta T_{\text{ad}}$  measurements in pulsed fields show that the full transformation requires a field of 7 T or more. In contrast to  $\text{Mn}_3\text{GaC}$ , the structural transformation in Mn-Cr-Co-Sb can follow the field-sweep rate of  $0.6 \text{ Ts}^{-1}$ . The faster response time in Mn-Cr-Co-Sb can be explained by the ten-times smaller volume change (0.05%) of the transformation, compared to  $\text{Mn}_3\text{GaC}$  (0.5%), which leads to less strain and stress. Therefore, the volume change during the first-order transition has not only an effect on the energy-barrier which has to be overcome for the formation of a nuclei, which relates to the width of the hysteresis, but also influences the structural response time.

$\text{Ni}_{50}\text{Mn}_{50-x}\text{In}_x$  Heusler alloys are well known magnetocaloric materials. Recent studies have shown that off-stoichiometric alloys ( $0 < x < 25$ ) are not stable and decompose into FM  $\text{Ni}_2\text{MnIn}$  and AF NiMn when annealed in the range  $650 \leq T \leq 750 \text{ K}$ . The partial decomposition can shift the transition temperatures due to the change in the chemical composition. The selective decomposition can, therefore, also be used to tune the magnetocaloric properties. For example the NiMn phase can act as nucleations centres for the transition similar as nano-indentations [Nie16]

The annealing of  $\text{Ni}_{50}\text{Mn}_{45}\text{In}_5$  at 650 K leads to the formation nano-precipitates of FM stoichiometric  $\text{Ni}_2\text{MnIn}$  embedded in an AF matrix. Annealing in a magnetic field leads to a shell-ferromagnetic effect which gives a monopolar-like response. The effect is related to a vertical shifting the magnetic hysteresis due to the pinned FM shell of the precipitates. Magnetization and FMR measurements in fields up to 14 T have shown that the pinned FM shell of the precipitate rotates in fields above 5 T while the soft FM phase is already saturated at about 0.3 T. The FMR analysis shows a strong coupling between the hard FM phase and the AF matrix. The effect relates to the surface-to-volume ratio of the precipitate and can only be observed for precipitate sizes of several nanometer. Further studies on annealed Ni-Mn-In Heusler with first-order transitions are necessary to study the effect of decomposition on magnetism and width of hysteresis to show if the selective formation of decomposition can improve the MCE.



## Schlussfolgerung

1 Die Arbeit präsentiert die Resultate der Untersuchungen des magnetokalorischen Effekts in Bezug auf dessen Abhängigkeit von der Feldänderungsrate des angelegten Magnetfeldes. Es wurden die Materialklassen  $\text{Mn}_3\text{GaC}$  Antiperovskite und Mn-Cr-Co-Sb Pniktide untersucht. Weiterhin wurden die Resultate und Untersuchungen der magnetischen Eigenschaften eines  $\text{Mn}_3\text{GaC}$  Einkristalls und der ferromagnetischen Nanometer großen Ausscheidungen in einer nicht stöchiometrischen Ni-Mn-In Heusler Legierung präsentiert.

Der AF/FM Phasenübergang erster Ordnung in  $\text{Mn}_3\text{GaC}$  zeigt eine schmale thermische Hysterese von 5 K. Dieser kann durch ein Magnetfeld induziert werden, wobei sich die Umwandlungstemperatur mit einer Rate von  $dT_i/dB = -5.7 \text{ K T}^{-1}$  verschiebt. Die schmale Hysterese und die starke Verschiebung ermöglichen einen vollständig reversiblen Übergang für ein zyklisch angelegtes Feld von 2 T. Der feldinduzierte Phasenübergang führt zu einem  $\Delta S$  von  $13 \text{ J kg}^{-1} \text{ K}^{-1}$  und einem  $\Delta T_{\text{ad}}$  von 4.7 K, diese sind ebenfalls vollständig reversibel. Diese Eigenschaften machen die Legierung interessant für magnetokalorische Kühlung unterhalb Raumtemperatur. Adiabatische Magnetisierungsmessungen in gepulsten Magnetfeldern haben gezeigt, dass die Magnetisierungsdynamik den Feldänderungsraten von  $1.3 \text{ Ts}^{-1}$  folgen kann. Beim Vergleich der kritischen Magnetfelder der isothermen und adiabatischen Messungen zeigt sich jedoch eine Unterkühlung des Umwandlungsbeginns für schnelle Feldänderungsraten.  $\Delta T_{\text{ad}}$  Messungen bei unterschiedlichen Feldänderungsraten zeigen, dass die strukturelle Umwandlung des AF/FM Phasenübergangs erster Ordnung der Rate von  $1 \text{ Ts}^{-1}$  nicht folgen kann. Dies führt zu einer Reduzierung von  $\Delta T_{\text{ad}}$  im Vergleich zu den Messungen geringerer Raten und steht im Widerspruch zu den adiabatischen Magnetisierungsmessungen in gepulsten Feldern. Dies kann durch unterschiedliche Reaktionszeiten der strukturellen und der magnetischen Umwandlung erklärt werden. Eine langsame strukturelle Reaktionszeit kann auf Verzerrungen und Spannungen zurückzuführen sein die während des isostrukturellen AF/FM Phasenübergangs mit der Volumenänderung von 0.5% entstehen [C14b]. Dies beeinflusst wiederum den magnetokalorischen Effekt. Eine Feldänderungsrate von  $1 \text{ Ts}^{-1}$  entspricht jedoch einer Frequenz von 500 Hz für ein zyklisch angelegtes Feld von 2 T. Diese Frequenz liegt weit oberhalb der Arbeitsfrequenz eines magnetokalorischen Kühlgeräts (1 – 10 Hz), so dass die  $\text{Mn}_3\text{GaC}$  Legierung für die magnetokalorische Kühlung unterhalb Raumtemperatur potentiell in Frage kommt.

Die ersten Untersuchungen an einem  $\text{Mn}_3\text{GaC}$  Einkristalls haben gezeigt, dass sich die Umwandlungstemperatur, die Umwandlungsbreite und  $dT_i/dB$  mit denen einer polykristallinen Probe vergleichen lassen, und zeigt weiterhin die Unabhängigkeit dieser Eigenschaften bezüglich der Probenmorphologie. Ferromagnetische Resonanz Messungen und Simulationen am  $\text{Mn}_3\text{GaC}$  Einkristall zeigen eine magnetisch leichte Richtung entlang der  $\{111\}$ -Achse und eine magnetokristalline Anisotropie-Energie von  $K_4 = -5.49 \text{ kJ m}^{-3}$ . Der geringe Wert für die magnetokristalline Anisotropie-

Energie kann auch die Ursache für die schmale Hysterese sein [Toh03]. Die magnetische Anisotropie-Energie in  $\text{Mn}_3\text{GaC}$  ist damit hauptsächlich durch die Form der Probe bestimmt und kann für die magnetokalorischen Kühlgeräte optimiert werden.

Die Cr und Co dotierten  $\text{Mn}_2\text{Sb}$  Pniktide haben einen Phasenübergang von einer antiferromagnetischen in eine ferrimagnetischen Phase. Dieser Übergang liegt nahe bei Raumtemperatur. Dieser Phasenübergang erster Ordnung verschiebt sich beim Anlegen eines Magnetfeldes mit einer Rate von  $dT_i/dB = -5 \text{ K T}^{-1}$  zu geringen Temperaturen. Der Übergang hat eine schmale Hysterese von 2.5 K. Das Material zeigt einen reversiblen inversen magnetokalorischen Effekt mit  $\Delta S = 4.8 \text{ J kg}^{-1} \text{ K}^{-1}$  und  $\Delta T_{\text{ad}} = -2.5 \text{ K}$  in einem sich ändernden Feld von 5 T. Die schmale Hysterese und die hinreichend große  $\Delta T_{\text{ad}}$  in 5 T machen diese Legierung zu einem potentiellen Material für magnetokalorische Kühlung.

$\Delta T_{\text{ad}}$  Messungen in gepulsten Magnetfeldern zeigen, dass eine vollständige Phasenumwandlung eine Feldstärke von mindestens 7 T benötigt. Im Gegensatz zu  $\text{Mn}_3\text{GaC}$  kann die strukturelle Umwandlung in Mn-Cr-Co-Sb den Feldänderungsraten von  $0.6 \text{ Ts}^{-1}$  folgen. Die schnelle Reaktionszeit in Mn-Cr-Co-Sb kann durch die zehnmal geringere Volumenänderung (0.05%) verglichen mit  $\text{Mn}_3\text{GaC}$  (0.5%) erklärt werden. Die Volumenänderung von Phasenübergängen erster Ordnung hat somit nicht nur einen Effekt auf die Energiebarriere welche bei der Keimbildung der neuen Phase überwunden werden muss, und somit auch mit der Hysteresenbreite korreliert, sondern sie hat auch einen Effekt auf die strukturelle Reaktionszeit.

$\text{Ni}_{50}\text{Mn}_{50-x}\text{In}_x$  Heusler sind bekannt als magnetokalorische Legierungen. Jüngste Studien haben gezeigt, dass nicht stöchiometrische ( $0 < x < 25$ ) Legierungen instabil sind. Sie entmischen beim Heizen im Bereich zwischen 650 und 750 K in eine ferromagnetische  $\text{Ni}_2\text{MnIn}$  und eine antiferromagnetische NiMn Phase. Eine teilweise Entmischung führt zu einer Verschiebung der Phasenübergangstemperatur da sich die chemische Zusammensetzung der Probe ändert. Eine gezielte Entmischung kann daher genutzt werden um die magnetokalorischen Eigenschaften der Probe zu verändern. So kann die NiMn Phase beispielsweise als Nukleationszentrum für die Umwandlung dienen, ähnlich wie Nanoeinprägungen [Nie16].

Das Heizen von  $\text{Ni}_{50}\text{Mn}_{45}\text{In}_5$  bei 650 K führt zur Entstehung von Nanometer großen Ausscheidungen der ferromagnetischen stöchiometrischen  $\text{Ni}_2\text{MnIn}$  Phase, eingebettet in einer antiferromagnetischen Matrix. Das Heizen in einem Magnetfeld führt zu der Entstehung von Nanometer großen Ausscheidungen die sowohl hart als auch weich ferromagnetischen Eigenschaften aufweisen und zusammen ein monopolähnliches Verhalten zeigt. Der Effekt ist verbunden mit einer vertikalen Verschiebung der magnetischen Hysteresekurve und lässt sich auf die gepinnte ferromagnetische Schale der Ausscheidung zurückführen. Magnetisierungs- und ferromagnetische Resonanz-Messungen in Feldern von bis zu 14 T haben gezeigt, dass die gepinnte ferromagnetische Schale der Ausscheidung erst ab Feldern von 5 T gedreht werden kann. Im Gegensatz dazu ist die weichmagnetische Phase bereits bei 0.3 T gesättigt. Die ferromagnetische Resonanz

Analyse zeigt eine starke Kopplung zwischen der hartmagnetischen Phase und der antiferromagnetischen Matrix. Der Effekt ist mit dem Oberfläche-zu-Volumen-Verhältnis der Ausscheidungen verknüpft und kann nur für Nanometer große Ausscheidungen beobachtet werden. Es sind weiterführende Untersuchungen an Ni-Mn-In Heusler Legierungen mit Phasenübergängen erster Ordnung nötig, um den Effekt des Heizens und der Entmischung auf die Magnetisierung und die Breite der Hysterese zu untersuchen. Auf diese Weise kann auch gezeigt werden in wie weit eine Entmischung den magnetokalorischen Effekt beeinflusst.

die Entstehung von Nanometer großen Ausscheidungen mit sowohl hart wie auch weich ferromagnetischen Eigenschaften. Die hartferromagnetische Schale ist dabei gepinnt bis zu einem externen magnetischen Feld von 5 T.



# Bibliography

- [Ace11] M. ACET, L. MAÑOSA, A. PLANES. *Magnetic-Field-Induced Effects in Martensitic Heusler-Based Magnetic Shape Memory Alloys*, Vol. 19. Elsevier B.V., Oxford (2011) 15
- [Aks07] S. AKSOY, T. KRENKE, M. ACET, E. F. WASSERMANN, X. MOYA, L. MAÑOSA, A. PLANES. *Tailoring magnetic and magnetocaloric properties of martensitic transitions in ferromagnetic Heusler alloys*. Appl. Phys. Lett. Vol. 91, 241916, (2007), DOI: 10.1063/1.2825283 3, 16, 18
- [Aks10] S. AKSOY. *Magnetic interaction in martensitic Ni-Mn based Heusler systems*. Ph. D. Thesis, University Duisburg-Essen (2010) 41
- [Alp63] H. A. ALPERIN, P. J. BROWN, R. NATHANS. *Aspherical Spin Density in the Ferrimagnetic Compound  $Mn_2Sb$* . J. Appl. Phys. Vol. 34:pp. 1201 (1963), DOI: 10.1063/1.1729433 25, 26
- [And89] A. S. ANDREENKO, K. P. BELOV, S. A. NIKITIN, A. M. TISHIN. *Magnetocaloric effects in rare-earth magnetic materials*. Sov. Phys. Uspekhi. Vol. 32, 649, (1989), URL <http://stacks.iop.org/0038-5670/32/i=8/a=R01> 71
- [Aus63] A. E. AUSTIN, E. ADELSON, W. H. CLOUD. *Magnetic Structures of Chromium-Modified  $Mn_2Sb$* . Physical Review Vol. 131, 4, (1963), DOI: 10.1103/PhysRev.131.1511 26
- [Bar04] M. I. BARTASHEVICH, T. GOTO, N. V. BARANOV, V. S. GAVIKO. *Volume magnetostriction at the AF-FRI metamagnetic transition in the itinerant-electron system  $Mn_{2-x}T_xSb$  ( $T=Co, Cr$ )*. Physica B: Condensed Matter Vol. 351:pp. 71 (2004), DOI: 10.1016/j.physb.2004.05.013 26
- [Bho07] P. A. BHOBE, K. R. PRIOLKAR, A. K. NIGAM. *Room temperature magnetocaloric effect in Ni-Mn-In*. Appl. Phys. Lett. Vol. 91, 242503, (2007), DOI: 10.1063/1.2823601 18
- [Bie62] P. E. BIERSTEDT, F. J. DARNELL, W. H. CLOUD, R. B. FLIPPEN, H. S. JARRETT. *Spiral Spin Configurations Accompanying Exchange Inversion*. Phys. Rev. Lett. Vol. 8, 1, (1962), DOI: 10.1103/PhysRevLett.8.15 26

- [Bir60] R. R. BIRSS. *The thermal expansion anomaly of gadolinium*. Proc. Royal Soc. A Vol. 255:pp. 398 (1960), DOI: [10.1098/rspa.1960.0074](https://doi.org/10.1098/rspa.1960.0074) 11
- [Bit62] T. A. BITHER, P. H. L. WALTER, W. H. CLOUD, T. J. SWOBODA, P. E. BIERSTEDT. *New Modified Mn<sub>2</sub>Sb Compositions Showing Exchange Inversion*. J. Appl. Phys. Vol. 33, 3:pp. 1346 (1962), DOI: [10.1063/1.1728723](https://doi.org/10.1063/1.1728723) 26
- [Bjø16] R. BJØRK, C. R. H. BAHL, K. K. NIELSEN. *The lifetime cost of a magnetic refrigerator*. Int. J. Ref. Vol. 63:pp. 48 (2016), DOI: [10.1016/j.ijrefrig.2015.08.022](https://doi.org/10.1016/j.ijrefrig.2015.08.022) 2
- [Bla78] C. BLAAUW, G. R. MECKAY, W. LEIPER. *Mössbauer Investigations of Mn<sub>2</sub>Sb Doped with Fe and Cr*. J. Magn. Magn. Mater. Vol. 8:pp. 240 (1978), DOI: [10.1016/0304-8853\(78\)90127-0](https://doi.org/10.1016/0304-8853(78)90127-0) 26
- [Bou66] J.-P. BOUCHAUD, R. FRUCHART, R. PAUTHENET, M. CUILLOT, H. BARTHOLIN, F. CHAISSÉ. *Antiferromagnetic-Ferromagnetic Transition in the Compound Mn<sub>3</sub>GaC*. J. Appl. Phys. Vol. 37, 3, (1966), DOI: [10.1063/1.1708544](https://doi.org/10.1063/1.1708544) 21, 22
- [Bro76] G. V. BROWN. *Magnetic heat pumping near room temperature*. J. Appl. Phys. Vol. 47, 3673, (1976), DOI: [10.1063/1.323176](https://doi.org/10.1063/1.323176) 1
- [Cak16] A. CAKIR, M. ACET, M. FARLE. *Shell-ferromagnetism of nano-Heuslers generated by segregation under magnetic field*. Sci Rep Vol. 6, 28931, (2016), DOI: [10.1038/srep28931](https://doi.org/10.1038/srep28931) 19, 91, 93, 100
- [Car13] L. CARON, X. F. MIAO, J. C. P. KLAASSE, S. GAMA, E. BRÜCK. *Tuning the giant inverse magnetocaloric effect in Mn<sub>2-x</sub>Cr<sub>x</sub>Sb compounds*. Appl. Phys. Lett. Vol. 103, 112404, (2013), DOI: [10.1063/1.4821197](https://doi.org/10.1063/1.4821197) 27
- [Cas04] F. CASANOVA, A. LABARTA, X. BATLLE, E. VIVES, J. MARCOS, L. MAÑOSA, A. PLANES. *Dynamics of the first-order magnetostructural transition in Gd<sub>5</sub>(Si<sub>x</sub>Ge<sub>1-x</sub>)<sub>4</sub>*. Eur. Phys. J. B Vol. 40:pp. 427 (2004), DOI: [10.1140/epjb/e2004-00274-x](https://doi.org/10.1140/epjb/e2004-00274-x) 47
- [Ç12] Ö. ÇAKIR, M. ACET. *Reversibility in the inverse magnetocaloric effect in Mn<sub>3</sub>GaC studied by direct adiabatic temperature-change measurements*. Appl. Phys. Lett. Vol. 100, 202404, (2012), DOI: [10.1063/1.4717181](https://doi.org/10.1063/1.4717181) 3, 10, 12, 21, 22, 47, 49, 51, 53, 59, 70
- [Ç13] Ö. ÇAKIR, M. ACET. *Adiabatic temperature change around coinciding first and second order magnetic transitions in Mn<sub>3</sub>Ga(C<sub>0.85</sub>N<sub>0.15</sub>)*. J. Magn. Magn. Mater. Vol. 344:pp. 207 (2013), DOI: [10.1016/j.jmmm.2013.05.057](https://doi.org/10.1016/j.jmmm.2013.05.057) 3, 24

- 
- [Ç14a] A. ÇAKIR. *Investigation of magneto-structural phase transitions in magnetic shape memory alloys*. Ph.D. Thesis, Muğla Sıtkı Koçman University (2014) 15
- [Ç14b] Ö. ÇAKIR, M. ACET, M. FARLE, A. SENYSHYN. *Neutron diffraction study of the magnetic-field-induced transition in  $Mn_3GaC$* . J. Appl. Phys. Vol. 115, 043913, (2014), DOI: [10.1063/1.4862903](https://doi.org/10.1063/1.4862903) 21, 22, 47, 63, 101, 103
- [Ç15a] A. ÇAKIR, L. RIGHI, F. ALBERTINI, M. ACET, M. FARLE. *Intermartensitic transitions and phase stability in  $Ni_{50}Mn_{50-x}Sn_x$  Heusler alloys*. Acta Mater. Vol. 99:pp. 140 (2015), DOI: <https://doi.org/10.1016/j.actamat.2015.07.072> 18
- [Ç15b] Ö. ÇAKIR, M. ACET, M. FARLE, E. DIAS, K. PRIOLKAR. *Kinetic arrest in magnetically inhomogeneous C-deficient  $Mn_3GaC$* . J. Magn. Magn. Mater. Vol. 390:pp. 96 (2015), DOI: [10.1016/j.jmmm.2015.04.084](https://doi.org/10.1016/j.jmmm.2015.04.084) 24, 27, 70
- [Ç16] Ö. ÇAKIR, M. ACET, M. FARLE, A. WILDES. *Magnetic correlations in the magnetocaloric materials  $Mn_3GaC$  and  $Mn_3Ga_{0.85}N_{0.15}$  studied by neutron polarization analysis and neutron depolarization*. J. Phys. Condens. Matter Vol. 28, 13LT02,;p. 4 (2016), DOI: [10.1088/0953-8984/28/13/13LT02](https://doi.org/10.1088/0953-8984/28/13/13LT02) 24
- [Ç17a] A. ÇAKIR, M. ACET. *Non-volatile high-temperature shell-magnetic pinning of Ni-Mn-Sn Heusler precipitates obtained by decomposition under magnetic field*. J. Magn. Magn. Mater. (2017), DOI: <https://doi.org/10.1016/j.jmmm.2017.06.069> 19, 100
- [Ç17b] A. ÇAKIR, M. ACET, U. WIEDWALD, T. KRENKE, M. FARLE. *Shell-ferromagnetic precipitation in martensitic off-stoichiometric Ni-Mn-In Heusler alloys produced by temper-annealing under magnetic field*. Acta Mater. Vol. 127:pp. 117 (2017), DOI: [10.1016/j.actamat.2017.01.027](https://doi.org/10.1016/j.actamat.2017.01.027) 19, 91, 93, 100
- [Chi16] A. CHIRKOVA, K. P. SKOKOV, L. SCHULTZ, N. V. BARANOV, O. GUT-FLEISCH, T. G. WOODCOCK. *Giant adiabatic temperature change in FeRh alloys evidenced by direct measurements under cyclic conditions*. Acta Mater. Vol. 106:pp. 15 (2016), DOI: [10.1016/j.actamat.2015.11.054](https://doi.org/10.1016/j.actamat.2015.11.054) 1, 12
- [Clo60] W. H. CLOUD, H. S. JARRETT, A. E. AUSTIN, E. ADELSON. *Neutron Diffraction Studies of Chromium-Modified  $Mn_2Sb$* . Physical Review Vol. 120, 6, (1960), DOI: [10.1103/PhysRev.120.1969](https://doi.org/10.1103/PhysRev.120.1969) 3, 26
- [Clo61] W. H. CLOUD, T. A. BITHER, T. J. SWOBODA. *Exchange Inversion in  $Mn_{2-x}Cr_xSb$* . J. Appl. Phys. Vol. 32, 3, (1961), DOI: [10.1063/1.2000497](https://doi.org/10.1063/1.2000497) 25, 26
- [Dar63] F. J. DARNELL, W. H. CLOUD, H. S. JARRETT. *X-Ray and Magnetization Studies of Cr-Modified  $Mn_2Sb$* . Physical Review Vol. 130, 2, (1963), DOI: [10.1103/PhysRev.130.647](https://doi.org/10.1103/PhysRev.130.647) 26, 27

- [Dia14] E. T. DIAS, K. R. PRIOLKAR, A. K. NIGAM. *Effect of carbon content on magnetostructural properties of  $Mn_3GaC$* . J. Magn. Magn. Mater. Vol. 363:pp. 140 (2014), DOI: [10.1016/j.jmmm.2014.03.052](https://doi.org/10.1016/j.jmmm.2014.03.052) 24, 49, 51, 59, 60, 65, 68, 70
- [Din18] L. DINCKLAGE, F. SCHEIBEL, A. ÇAKIR, M. FARLE, M. ACET. *Annealing-time and annealing-temperature dependencies of the size of Ni-Mn-In shell-ferromagnetic nano-precipitates by Scherrer analysis*. AIP Adv. Vol. 8:p. 025012 (2018), DOI: [10.1063/1.5018851](https://doi.org/10.1063/1.5018851) 19, 20, 100
- [Dub09] I. DUBENKO, M. KHAN, A. K. PATHAK, B. R. GAUTAM, S. STADLER, N. ALI. *Magnetocaloric effects in Ni-Mn-X based Heusler alloys with X=Ga, Sb, In*. J. Magn. Magn. Mater. Vol. 321:pp. 754 (2009), DOI: [10.1016/j.jmmm.2008.11.043](https://doi.org/10.1016/j.jmmm.2008.11.043) 3, 18
- [Dub12] I. DUBENKO, T. SAMANTA, A. QUETZ, A. KAZAKOV, I. RODIONOV, D. METTUS, V. PRUDNIKOV, S. STADLER, P. ADAMS, J. PRESTIGIACOMO, A. GRANOVSKY, A. ZHUKOV, N. ALI. *The comparison of direct and indirect methods for determining the magnetocaloric parameters in the Heusler alloy  $Ni_{50}Mn_{34.8}In_{14.2}B$* . Appl. Phys. Lett. Vol. 100, 192402, (2012), DOI: [10.1063/1.4714539](https://doi.org/10.1063/1.4714539) 34
- [Dum02] E. DUMAN, M. ACET, Y. ELERMAN, A. ELMALI, E. F. WASSERMANN. *Magnetic interactions in  $Pr_{1-x}Tb_xMn_2Ge_2$* . J. Magn. Magn. Mater. Vol. 238:pp. 11 (2002) 33
- [Dut16] B. DUTTA, A. ÇAKIR, C. GIACOBBE, A. AL-ZUBI, T. HICKEL, M. ACET, J. NEUGEBAUER. *Ab initio Prediction of Martensitic and Intermartensitic Phase Boundaries in Ni-Mn-Ga*. Phys. Rev. Lett. Vol. 116, 025503, (2016), URL <https://link.aps.org/doi/10.1103/PhysRevLett.116.025503> 18
- [Fae12] S. FÄHLER, U. K. RÖSSLER, O. KASTNER, J. ECKERT, G. EGGELER, H. EMMERICH, P. ENTEL, S. MÜLLER, E. QUANDT, K. ALBE. *Caloric Effects in Ferroic Materials: New Concepts for Cooling*. Adv. Eng. Mater Vol. 14, 1-2, (2012), DOI: [10.1002/adem.201100178](https://doi.org/10.1002/adem.201100178) 15
- [Fra88] Z. FRAIT, D. FRAITOVÁ. *Spin-Wave Resonance in Metals*, Vol. 2, book section 1. North-Holland, Amsterdam (1988) 74
- [Fri16] M. FRIES, K. P. SKOKOV, D. Y. KARPENKOV, V. FRANCO, S. ENER, O. GUT-FLEISCH. *The influence of magnetocrystalline anisotropy on the magnetocaloric effect: A case study on  $Co_2B$* . Appl. Phys. Lett. Vol. 109, 232406, (2016), DOI: [10.1063/1.4971839](https://doi.org/10.1063/1.4971839) 70, 71



- 
- [Fru70] D. FRUCHART, E. F. BERTAUT, F. SAYETAT, M. NASR EDDINE, R. FRUCHART, J. P. SÉNATEUR. *Structure Magnetique et  $Mn_3GaC$* . Solid State Commun. Vol. 8:pp. 91 (1970) 21
- [Fru78] D. FRUCHART, E. F. BERTAUT. *Magnetic Studies of the Metallic Perovskite-Type Compounds of Manganese\**. J. Phys. Soc. Jpn. Vol. 44, 3, (1978) 21, 22, 24, 78
- [Fru05] D. FRUCHART, F. ALLAB, M. BALLI, D. GIGNOUX, E. K. HLIL, A. KOUMINA, N. SKRYABINA, J. TOBOLA, P. WOLFERS, R. ZACH. *On the magnetocaloric effect in d-metal pnictides*. Physica A Vol. 358:pp. 123 (2005), DOI: 10.1016/j.physa.2005.06.013 25
- [Fuj02] S. FUJIEDA, A. FUJITA, K. FUKAMICHI. *Large magnetocaloric effect in  $La(Fe_xSi_{1-x})_{13}$  itinerant-electron metamagnetic compounds*. Appl. Phys. Lett. Vol. 81, 7, (2002), DOI: 10.1063/1.1498148 2
- [Fuk06] K. FUKAMICHI, A. FUJITA, S. FUJIEDA. *Large magnetocaloric effects and thermal transport properties of  $La(FeSi)_{13}$  and their hydrides*. J. Alloys Compd. pp. 307–312 (2006), DOI: 10.1016/j.jallcom.2005.04.022 2
- [Gar83] J. GARCÍA, J. BARTOLOMÉ, D. GONZÁLEZ. *Thermophysical properties of intermetallic  $Mn_3MC$  perovskites*. J. Chem. Thermodyn. Vol. 15:pp. 1059 (1983) 21, 22
- [Gia33] W. F. GIAUQUE, D. P. MACDOUGALL. *Attainment of Temperatures Below 1° Absolute by Demagnetization of  $Gd_2(SO_4)_3 \cdot 8H_2O$* . Phys. Rev. Vol. 43:pp. 768 (1933), URL <https://link.aps.org/doi/10.1103/PhysRev.43.768> 1
- [Gig99] A. GIGUÈRE, M. FOLDEAKI, B. RAVI GOPAL, R. CHAHINE, T. K. BOSE, A. FRYDMAN, J. A. BARCLAY. *Direct Measurement of the “Giant” Adiabatic Temperature Change in  $Gd_5Si_2Ge_2$* . Phys. Rev. Lett. Vol. 83, 11, (1999), DOI: 10.1103/PhysRevLett.83.2262 34
- [Gil04] T. L. GILBERT. *A Phenomenological Theory of Damping in Ferromagnetic Materials*. IEEE Trans. Magn. Vol. 40, 6, (2004), DOI: 10.1109/tmag.2004.836740 36
- [Goo63] J. B. GOODENOUGH. *Magnetism and the Chemical Bond*. Interscience, New York-London (1963) 24
- [Got12] T. GOTTSCHALL. *Untersuchung des magnetokalorischen Effektes in Ni-Mn basierten Heusler-Legierungen*. Master Thesis (2012) 43

- [Got16a] T. GOTTSCHALL. *On the magnetocaloric properties of Heusler compounds: Reversible, time- and size-dependent effects of the martensitic phase transition.* Ph.D. Thesis, Technical University Darmstadt (2016) 43, 46
- [Got16b] T. GOTTSCHALL, K. P. SKOKOV, D. BENKE, M. E. GRUNER, O. GUTFLEISCH. *Contradictory role of the magnetic contribution in inverse magnetocaloric Heusler materials.* Phys. Rev. B Vol. 93, 184431, (2016), DOI: [10.1103/PhysRevB.93.184431](https://doi.org/10.1103/PhysRevB.93.184431) 10, 18, 53
- [Got16c] T. GOTTSCHALL, K. P. SKOKOV, F. SCHEIBEL, M. ACET, M. G. ZAVAREH, Y. SKOURSKI, J. WOSNITZA, M. FARLE, O. GUTFLEISCH. *Dynamical Effects of the Martensitic Transition in Magnetocaloric Heusler Alloys from Direct  $\Delta T_{ad}$  Measurements under Different Magnetic-Field-Sweep Rates.* Phys. Rev. Applied Vol. 5, 024013, (2016), DOI: [10.1103/PhysRevApplied.5.024013](https://doi.org/10.1103/PhysRevApplied.5.024013) 3, 45, 53
- [Gri54] M. GRIFFEL, R. E. SKOCHDOPOLE, F. H. SPEDDING. *The Heat Capacity of Gadolinium from 15 to 355° K.* Physical Review Vol. 93, 4, (1954), DOI: <https://doi.org/10.1103/PhysRev.93.657> 11
- [Gru15] M. E. GRUNER, W. KEUNE, B. ROLDAN CUENYA, C. WEIS, J. LANDERS, S. I. MAKAROV, D. KLAR, M. Y. HU, E. E. ALP, J. ZHAO, M. KRAUTZ, O. GUTFLEISCH, H. WENDE. *Element-Resolved Thermodynamics of Magnetocaloric  $LaFe_{13-x}Si_x$ .* Phys. Rev. Lett. Vol. 114, 057202, (2015), DOI: [10.1103/PhysRevLett.114.057202](https://doi.org/10.1103/PhysRevLett.114.057202) 10
- [Gsc08] K. A. GSCHNEIDNER, V. K. PECHARSKY. *Thirty years of near room temperature magnetic cooling: Where we are today and future prospects.* Int. J. Ref. Vol. 31:pp. 945 (2008), DOI: [10.1016/j.ijrefrig.2008.01.004](https://doi.org/10.1016/j.ijrefrig.2008.01.004) 1
- [Gut11] O. GUTFLEISCH, M. A. WILLARD, E. BRÜCK, C. H. CHEN, S. G. SANKAR, J. P. LIU. *Magnetic materials and devices for the 21st century: stronger, lighter, and more energy efficient.* Adv. Mater. Vol. 23:pp. 821 (2011), DOI: [10.1002/adma.201002180](https://doi.org/10.1002/adma.201002180) 1
- [Gut16] O. GUTFLEISCH, T. GOTTSCHALL, M. FRIES, D. BENKE, I. RADULOV, K. P. SKOKOV, H. WENDE, M. GRUNER, M. ACET, P. ENTEL, M. FARLE. *Mastering hysteresis in magnetocaloric materials.* Philos. Trans. R. Soc. London, Ser. A Vol. 374, 20150308, (2016), DOI: [10.1098/rsta.2015.0308](https://doi.org/10.1098/rsta.2015.0308) 2, 3, 4
- [GZ15] M. GHORBANI ZAVAREH, C. SALAZAR MEJÍA, A. K. NAYAK, Y. SKOURSKI, J. WOSNITZA, C. FELSER, M. NICKLAS. *Direct measurements of the magnetocaloric effect in pulsed magnetic fields: The example of the*

- 
- Heusler alloy Ni<sub>50</sub>Mn<sub>35</sub>In<sub>15</sub>*. Appl. Phys. Lett. Vol. 106, 071904, (2015), DOI: [10.1063/1.4913446](https://doi.org/10.1063/1.4913446) 45
- [Hal98] S. V. HALILOV, A. Y. PERLOV, P. M. OPPENEER, A. N. YARESKO, V. N. ANTONOV. *Magnetocrystalline anisotropy energy in cubic Fe, Co, and Ni: Applicability of local-spin-density theory reexamined*. Phys. Rev. B Vol. 57, 16, (1998) 78
- [Har93] T. HARADA, K. NISHIMURA, T. KANOMATA, T. KANEKO. *Transport Properties of Ternary Magnetic Compounds Mn<sub>3-x</sub>M<sub>x</sub>GaC (M=Cr and Fe)*. Jpn. J. Appl. Phys. Vol. 32:pp. 280 (1993) 22, 23
- [Hea55] L. HEATON, N. S. GINGRICH. *The Crystal Structure of Mn<sub>2</sub>Sb*. Acta Cryst. Vol. 8:pp. 207 (1955) 25
- [Hel94] K.-H. HELLWEGE. *Einführung in die Festkörperphysik*. Springer-Verlag, Berlin, 3 Edition (1994) 36
- [Hor92] E. HORNBOGEN. *Reversibility and Hysteresis of Martensitic Transformations*. Phys. Stat. Sol. B Vol. 172:pp. 161 (1992), DOI: [10.1002/pssb.2221720116](https://doi.org/10.1002/pssb.2221720116) 11, 12
- [How57] L. HOWE, H. P. MYERS. *The magnetic properties of alloys having the compositions Mn<sub>60</sub>Al<sub>x</sub>Zn<sub>20-x</sub>C<sub>20</sub> and Mn<sub>60</sub>Ga<sub>x</sub>Zn<sub>20-x</sub>C<sub>20</sub>*. Phil Mag. Vol. 2:pp. 554 (1957), DOI: [10.1080/14786435708243845](https://doi.org/10.1080/14786435708243845) 21
- [Ito08] W. ITO, M. NAGASAKO, R. Y. UMETSU, R. KAINUMA, T. KANOMATA, K. ISHIDA. *Atomic ordering and magnetic properties in the Ni<sub>45</sub>Co<sub>5</sub>Mn<sub>36.7</sub>In<sub>13.3</sub> metamagnetic shape memory alloy*. Appl. Phys. Lett. Vol. 93, 232503, (2008), DOI: [10.1063/1.3043456](https://doi.org/10.1063/1.3043456) 16, 18
- [Jar61] H. S. JARRETT, P. E. BIERSTEDT, F. J. DARNELL, M. SPARKS. *Magnetic Anisotropy and Electrical Resistivity in Exchange Inversion Compounds*. J. Appl. Phys. Vol. 32, 3, (1961), DOI: [10.1063/1.2000498](https://doi.org/10.1063/1.2000498) 26
- [Kae17] B. KAESWURM, A. BARCZA, M. VÖGLER, P. T. GEIGER, M. KATTER, O. GUTFLEISCH, L. F. COHEN. *Behaviour of the Young's modulus at the magnetocaloric transition in La(Fe,Co,Si)<sub>13</sub>*. J. Alloys Compd. Vol. 697:pp. 427 (2017), DOI: <https://doi.org/10.1016/j.jallcom.2016.11.360> 2
- [Kag88] M. I. KAGANOV, A. V. CHUBUKOV. *Spin Waves in Magnetic Dielectrics Current Status of the Theory*, Vol. 1, book section 1. North-Holland, Amsterdam (1988) 36

- [Kam98] K. KAMISHIMA, M. I. BARTASHEVICH, T. GOTO, M. KIKUCHI, T. KANOMATA. *Magnetic Behavior of  $Mn_3GaC$  under High Magnetic Field and High Pressure*. J. Phys. Soc. Jpn. Vol. 67, 5, pp. 1748 (1998), DOI: [10.1143/JPSJ.67.1748](https://doi.org/10.1143/JPSJ.67.1748) 23
- [Kan84] T. KANOMATA, H. IDO. *Magnetic transitions in  $Mn_{2-x}M_xSb$  ( $M=3d$  metals)*. J. Appl. Phys. Vol. 55, 6, pp. 2039 (1984), DOI: [10.1063/1.333558](https://doi.org/10.1063/1.333558) 3, 25, 26
- [Kan87a] T. KANEKO, T. KANOMATA, S. MIURA, G. KIDO, Y. NAKAGAWA. *Field-induced transitions in intermetallic compounds  $Mn_3GaC$  and  $Mn_3ZnC$* . J. Magn. Mater. Vol. 70, pp. 261 (1987), DOI: [https://doi.org/10.1016/0304-8853\(87\)90431-8](https://doi.org/10.1016/0304-8853(87)90431-8) 21
- [Kan87b] T. KANEKO, T. KANOMATA, K. SHIRAKAWA. *Pressure Effect on the Magnetic Transition Temperatures in the Intermetallic Compounds  $Mn_3GaC$  ( $M=Ga, Zb$  and  $Sn$ )*. J. Phys. Soc. Jpn. Vol. 56, 11, (1987) 21, 22, 23
- [Kas59] J. S. KASPER, J. S. KOUVEL. *The antiferromagnetic structure of  $NiMn$* . J. Phys. Chem. Solids. Vol. 11, pp. 231 (1959) 18, 91
- [Kau11] S. KAUFMANN, R. NIEMANN, T. THERSLEFF, U. K. RÖSSLER, O. HECZKO, J. BUSCHBECK, B. HOLZAPFEL, L. SCHULTZ, S. FÄHLER. *Modulated martensite: why it forms and why it deforms easily*. New J. Phys. Vol. 13, 053029, (2011), URL <http://stacks.iop.org/1367-2630/13/i=5/a=053029> 15
- [Kim08] S.-H. KIM, M. BOSTRÖM, D.-K. SEO. *Two-Dimensional Superdegeneracy and Structure-Magnetism Correlations in Strong Ferromagnet,  $Mn_2Ga_5$* . J. AM. CHEM. SOC. Vol. 130, pp. 1384 (2008) 67
- [Kit60] C. KITTEL. *Model of Exchange-Inversion Magnetization*. Physical Review Vol. 120, 2, (1960), DOI: [10.1103/PhysRev.120.335](https://doi.org/10.1103/PhysRev.120.335) 26, 27
- [Kit06] C. KITTEL. *Einführung in die Festkörperphysik*. Oldenbourg Verlag München Wien, 14 Edition (2006) 35, 36
- [Kit10] A. KITANOVSKI, P. W. EGOLF. *Innovative ideas for future research on magnetocaloric technologies*. Int. J. Ref. Vol. 33, pp. 449 (2010), DOI: [10.1016/j.ijrefrig.2009.11.005](https://doi.org/10.1016/j.ijrefrig.2009.11.005) 2
- [Koy04] K. KOYAMA, T. KANOMATA, T. WATANABE, T. SUZUKI, H. NISHIHARA, K. WATANABE. *Magnetic transitions in  $Mn_3Ga_{1-x}Al_xC$  ( $0 \leq x \leq 0.1$ )*. J. Magn. Mater. Vol. 272-276, pp. E615 (2004), DOI: [10.1016/j.jmmm.2003.11.312](https://doi.org/10.1016/j.jmmm.2003.11.312) 23

- 
- [Kra14] M. KRAUTZ, K. SKOKOV, T. GOTTSCHALL, C. S. TEIXEIRA, A. WASKE, J. LIU, L. SCHULTZ, O. GUTFLEISCH. *Systematic investigation of Mn substituted  $\text{La}(\text{Fe},\text{Si})_{13}$  alloys and their hydrides for room-temperature magnetocaloric application.* J. Alloys Compd. Vol. 598:pp. 27 (2014), DOI: [10.1016/j.jallcom.2014.02.015](https://doi.org/10.1016/j.jallcom.2014.02.015) 2
- [Kre05a] T. KRENKE, M. ACET, E. F. WASSERMANN, X. MOYA, L. MAÑOSA, A. PLANES. *Martensitic transitions and the nature of ferromagnetism in the austenitic and martensitic states of Ni-Mn-Sn alloys.* Phys. Rev. B Vol. 72, 014412, (2005), URL <https://link.aps.org/doi/10.1103/PhysRevB.72.014412> 15, 16
- [Kre05b] T. KRENKE, E. DUMAN, M. ACET, E. F. WASSERMANN, X. MOYA, L. MAÑOSA, A. PLANES. *Inverse magnetocaloric effect in ferromagnetic Ni-Mn-Sn alloys.* Nat. Mater. Vol. 4:pp. 450 (2005), DOI: [10.1038/nmat1395](https://doi.org/10.1038/nmat1395) 3, 15, 18, 80
- [Kre06a] T. KRENKE, M. ACET, E. F. WASSERMANN, X. MOYA, L. MAÑOSA, A. PLANES. *Ferromagnetism in the austenitic and martensitic states of Ni-Mn-In alloys.* Phys. Rev. B Vol. 73, 17, (2006), DOI: [10.1103/PhysRevB.73.174413](https://doi.org/10.1103/PhysRevB.73.174413) 15, 92, 96
- [Kre06b] T. KRENKE, M. ACET, E. F. WASSERMANN, X. MOYA, L. MAÑOSA, A. PLANES. *Ferromagnetism in the austenitic and martensitic states of Ni-Mn-In alloys.* Phys. Rev. B Vol. 73, 17, (2006), DOI: [10.1103/PhysRevB.73.174413](https://doi.org/10.1103/PhysRevB.73.174413) 16
- [Kre07a] T. KRENKE, E. DUMAN, M. ACET, X. MOYA, L. MAÑOSA, A. PLANES. *Effect of Co and Fe on the inverse magnetocaloric properties of Ni-Mn-Sn.* J. Appl. Phys. Vol. 102, 033903, (2007), DOI: [10.1063/1.2761853](https://doi.org/10.1063/1.2761853) 3, 18
- [Kre07b] T. KRENKE, E. DUMAN, M. ACET, E. F. WASSERMANN, X. MOYA, L. MAÑOSA, A. PLANES, E. SUARD, B. OULADDIAF. *Magnetic superelasticity and inverse magnetocaloric effect in Ni-Mn-In.* Phys. Rev. B Vol. 75, 10, (2007), DOI: [10.1103/PhysRevB.75.104414](https://doi.org/10.1103/PhysRevB.75.104414) 3, 15, 18
- [Kre07c] T. KRENKE, X. MOYA, S. AKSOY, M. ACET, P. ENTEL, L. MAÑOSA, A. PLANES, Y. ELERMAN, A. YÜCEL, E. F. WASSERMANN. *Electronic aspects of the martensitic transition in Ni-Mn based Heusler alloys.* J. Magn. Mater. Vol. 310:pp. 2788 (2007), DOI: <https://doi.org/10.1016/j.jmmm.2006.10.1139> 16

- [Kre16] T. KRENKE, A. ÇAKIR, F. SCHEIBEL, M. ACET, M. FARLE. *Magnetic proximity effect and shell-ferromagnetism in metastable  $Ni_{50}Mn_{45}Ga_5$* . J. Appl. Phys. Vol. 120, 243904, (2016), DOI: [10.1063/1.4972480](https://doi.org/10.1063/1.4972480) 19, 100
- [Lan35] L. LANDAU, E. LIFSHITS. *On the Theory of the Dispersion of Magnetic Permeability in Ferromagnetic Bodies*. Phys. Zeitsch. der Sow. Vol. 8:pp. 153 (1935) 36
- [Lar11] R. LARA, A. FRANCA, F. SIMONE, P. ANTONIO. *Crystal Structures of Modulated Martensitic Phases of FSM Heusler Alloys*. Mater. Sci. Forum Vol. 684:pp. 105 (2011), DOI: [10.4028/www.scientific.net/MSF.684.105](https://doi.org/10.4028/www.scientific.net/MSF.684.105) 15
- [Lew06] L. H. LEWIS, D. YODER, A. R. MOODENBAUGH, D. A. FISCHER, M. H. YU. *Magnetism and the defect state in the magnetocaloric antiperovskite  $Mn_3GaC_{1-\delta}$* . J. Phys. Condens. Matter Vol. 18:pp. 1677 (2006), DOI: [10.1088/0953-8984/18/5/020](https://doi.org/10.1088/0953-8984/18/5/020) 24, 68
- [l'H79a] P. L'HÉRITIER, D. FRUCHART, R. MADAR, R. FRUCHART. *Instabilités électroniques dans les composés du manganèse de type perovskite métallique. Relation avec les changements de valence dans les composés de terres rares*. Mat. Res. Bull. Vol. 14:pp. 1089 (1979) 23
- [l'H79b] P. L'HÉRITIER, D. FRUCHART, R. MADAR, R. FRUCHART. *Structures magnétiques et transitions du premier ordre dans les perovskites métalliques  $GaMn_3(C_{1-x}N_x)$ . Relation avec les composés de terres rares à changement de valence*. Mat. Res. Bull. Vol. 4:pp. 1203 (1979) 23
- [Lin08] J. LINDNER, M. FARLE. *Magnetic Anisotropy of Heterostructures*, Vol. 227 von *Springer Tracts in Modern Physics*. Springer-Verlag, Berlin (2008) 36
- [Liu12a] J. LIU, T. GOTTSCHALL, K. P. SKOKOV, J. D. MOORE, O. GUTFLEISCH. *Giant magnetocaloric effect driven by structural transitions*. Nat. Mater. Vol. 11:pp. 620 (2012), DOI: [10.1038/nmat3334](https://doi.org/10.1038/nmat3334) 1, 3, 10, 15, 18
- [Liu12b] J. LIU, J. D. MOORE, K. P. SKOKOV, M. KRAUTZ, K. LÖWE, A. BARCZA, M. KATTER, O. GUTFLEISCH. *Exploring  $La(Fe,Si)_{13}$ -based magnetic refrigerants towards application*. Scr. Mater. Vol. 67:pp. 584 (2012), DOI: <https://doi.org/10.1016/j.scriptamat.2012.05.039> 2
- [Lov15] E. LOVELL, A. M. PEREIRA, A. D. CAPLIN, J. LYUBINA, L. F. COHEN. *Dynamics of the First-Order Metamagnetic Transition in Magnetocaloric  $La(Fe,Si)_{13}$ : Reducing Hysteresis*. Ad. Energy Mater. Vol. 5, 1401639, (2015), DOI: [10.1002/aenm.201401639](https://doi.org/10.1002/aenm.201401639) 51

- [Loz14] J. A. LOZANO, K. ENGELBRECHT, C. R. H. BAHL, K. K. NIELSEN, J. R. BARBOSA, A. T. PRATA, N. PRYDS. *Experimental and numerical results of a high frequency rotating active magnetic refrigerator*. Int. J. Ref. Vol. 37:pp. 92 (2014), DOI: [10.1016/j.ijrefrig.2013.09.002](https://doi.org/10.1016/j.ijrefrig.2013.09.002) 2, 47
- [May17] A. F. MAY, Y. LIU, S. CALDER, D. S. PARKER, T. PANDEY, E. CAKMAK, H. CAO, J. YAN, M. A. MCGUIRE. *Magnetic order and interactions in ferrimagnetic  $Mn_3Si_2Te_6$* . Phys. Rev. B Vol. 95, 174440, (2017), DOI: [10.1103/PhysRevB.95.174440](https://doi.org/10.1103/PhysRevB.95.174440) 33
- [McM06] R. D. MCMICHAEL, B. B. MARANVILLE. *Edge saturation fields and dynamic edge modes in ideal and nonideal magnetic film edges*. Phys. Rev. B Vol. 74, 024424, (2006), DOI: [10.1103/PhysRevB.74.024424](https://doi.org/10.1103/PhysRevB.74.024424) 74
- [Mec97] R. MECKENSTOCK. *Untersuchung der magnetischen Eigenschaften von Fe/Ag-Schichtsystemen mit der konventionellen und der oft aufgelösten ferromagnetischen Resonanz*. Thesis (1997) 35, 37, 38
- [Mec08] R. MECKENSTOCK. *Invited Review Article: Microwave spectroscopy based on scanning thermal microscopy: resolution in the nanometer range*. Rev Sci Instrum Vol. 79, 041101, (2008), DOI: [10.1063/1.2908445](https://doi.org/10.1063/1.2908445) 74
- [Mey73] G. MEYRICK, G. W. POWELL. *Phase Transformations in Metals and Alloys*. Annu. Rev. Mater. Sci. Vol. 3:pp. 327 (1973), DOI: [10.1146/annurev.ms.03.080173.001551](https://doi.org/10.1146/annurev.ms.03.080173.001551) 11
- [Miy11] T. MIYAMOTO, W. ITO, R. Y. UMETSU, T. KANOMATA, K. ISHIDA, R. KAINUMA. *Influence of Annealing Conditions on Magnetic Properties of  $Ni_{50}Mn_{50-x}In_x$  Heusler-Type Alloys*. Materials Transactions Vol. 52, 9, pp. 1836 (2011), DOI: [10.2320/matertrans.M2011125](https://doi.org/10.2320/matertrans.M2011125) 18
- [Mn10] L. MAÑOSA, D. GONZÁLEZ-ALONSO, A. PLANES, E. BONNOT, M. BARRIO, J. L. TAMARIT, S. AKSOY, M. ACET. *Giant solid-state barocaloric effect in the Ni-Mn-In magnetic shape-memory alloy*. Nat Mater Vol. 9:pp. 478 (2010), DOI: [10.1038/nmat2731](https://doi.org/10.1038/nmat2731) 3, 15
- [Mn13] L. MAÑOSA, A. PLANES, M. ACET. *Advanced materials for solid-state refrigeration*. J. Mater. Chem. A Vol. 1, 4925, (2013), DOI: [10.1039/c3ta01289a](https://doi.org/10.1039/c3ta01289a) 1
- [Mot88] K. MOTIZUKI, H. NAGAI. *Electronic band structures and magnetism of the cubic perovskite-type manganese compounds  $Mn_3MC$* . J. Phys. C: Solid State Phys. Vol. 21:pp. 5251 (1988) 22, 24



- [Moy06] X. MOYA, L. MAÑOSA, A. PLANES, T. KRENKE, M. ACET, E. F. WASSERMANN. *Martensitic transition and magnetic properties in Ni-Mn-X alloys*. Mater. Sci. Eng. A Vol. 438-440:pp. 911 (2006), DOI: <https://doi.org/10.1016/j.msea.2006.02.053> 15
- [Nie12] R. NIEMANN, U. K. RÖSSLER, M. E. GRUNER, O. HECZKO, L. SCHULTZ, S. FÄHLER. *The Role of Adaptive Martensite in Magnetic Shape Memory Alloys*. Adv. Eng. Mater Vol. 14, 8, (2012), DOI: [10.1002/adem.201200058](https://doi.org/10.1002/adem.201200058) 15
- [Nie16] R. NIEMANN, S. HAHN, A. DIESTEL, A. BACKEN, L. SCHULTZ, K. NIELSCH, M. F. X. WAGNER, S. FÄHLER. *Reducing the nucleation barrier in magnetocaloric Heusler alloys by nanoindentation*. APL Materials Vol. 4, 064101, (2016), DOI: [10.1063/1.4943289](https://doi.org/10.1063/1.4943289) 19, 102, 104
- [Nie17] R. NIEMANN, A. BACKEN, S. KAUFFMANN-WEISS, C. BEHLER, U. K. RÖSSLER, H. SEINER, O. HECZKO, K. NIELSCH, L. SCHULTZ, S. FÄHLER. *Nucleation and growth of hierarchical martensite in epitaxial shape memory films*. Acta Mater. Vol. 132:pp. 327 (2017), DOI: <https://doi.org/10.1016/j.actamat.2017.04.032> 16
- [Nol15] G. NOLZE. *Euler angles and crystal symmetry*. Cryst. Res. Technol. Vol. 50:pp. 188 (2015), DOI: [10.1002/crat.201400427](https://doi.org/10.1002/crat.201400427) 68, 69
- [O'C15] K. O'CONNELL, J. R. REGALBUTO. *High Sensitivity Silicon Slit Detectors for 1nm Powder XRD Size Detection Limit*. Catal. Lett. Vol. 145, 3:pp. 777 (2015), DOI: [10.1007/s10562-015-1479-6](https://doi.org/10.1007/s10562-015-1479-6) 100
- [Oki68] T. OKITA, Y. MAKINO. *Crystal Magnetic Anisotropy and Magnetization of MnSb*. J. Phys. Soc. Jpn. Vol. 25, 1, (1968) 27
- [Ove99] R. W. OVERHOLSER, M. WUTTIG, D. A. NEUMANN. *Chemical ordering in Ni-Mn-Ga Heusler alloys*. Scr. Mater Vol. 40, 10:pp. 1095 (1999), DOI: [https://doi.org/10.1016/S1359-6462\(99\)00080-9](https://doi.org/10.1016/S1359-6462(99)00080-9) 15
- [Pec97] V. K. PECHARSKY, K. A. GSCHNEIDNER. *Giant Magnetocaloric Effect in  $Gd_5(Si_2Ge_2)$* . Phys. Rev. Lett. Vol. 78, 23, (1997) 1, 2
- [Pec99] V. K. PECHARSKY, K. A. GSCHNEIDNER. *Magnetocaloric effect and magnetic refrigeration*. J. Magn. Magn. Mater. Vol. 200:pp. 44 (1999) 2
- [Pep01] W. PEPPERHOFF, M. ACET. *Constitution and Magnetism of Iron and its Alloys*. Springer-Verlag, Berlin (2001), DOI: [10.1007/978-3-662-04345-5](https://doi.org/10.1007/978-3-662-04345-5) 11, 16
- [Pla07] A. PLANES, L. MAÑOSA, X. MOYA, T. KRENKE, M. ACET, E. F. WASSERMANN. *Magnetocaloric effect in Heusler shape-memory alloys*. J. Magn. Magn. Mater. Vol. 310:pp. 2767 (2007), DOI: [10.1016/j.jmmm.2006.10.1041](https://doi.org/10.1016/j.jmmm.2006.10.1041) 3



- 
- [Pla09] A. PLANES, L. MAÑOSA, M. ACET. *Magnetocaloric effect and its relation to shape-memory properties in ferromagnetic Heusler alloys*. J. Phys. Condens. Matter. Vol. 21, 233201, (2009), DOI: [10.1088/0953-8984/21/23/233201](https://doi.org/10.1088/0953-8984/21/23/233201) 15, 16, 17
- [Poo83] C. P. J. POOLE. *Electron Spin Resonance*. Dover Publications, Inc., Mineola, New York, 2. Edition (1983) 35, 74
- [Por13] G. PORCARI, M. BUZZI, F. CUGINI, R. PELLICELLI, C. PERNECHELE, L. CARON, E. BRÜCK, M. SOLZI. *Direct magnetocaloric characterization and simulation of thermomagnetic cycles*. Rev. Sci. Instrum. Vol. 84, 073907, (2013), DOI: [10.1063/1.4815825](https://doi.org/10.1063/1.4815825) 44
- [Pri82] G. A. PRINZ, G. T. RADO, J. J. KREBS. *Magnetic properties of single-crystal {110} iron films grown on GaAs by molecular beam epitaxy (invited)*. J. Appl. Phys. Vol. 53, 3, (1982), DOI: [10.1063/1.330707](https://doi.org/10.1063/1.330707) 36
- [Roe12] F. M. RÖMER, M. MÖLLER, K. WAGNER, L. GATHMANN, R. NARKOWICZ, H. ZÄHRES, B. R. SALLES, P. TORELLI, R. MECKENSTOCK, J. LINDNER, M. FARLE. *In situ multifrequency ferromagnetic resonance and x-ray magnetic circular dichroism investigations on Fe/GaAs(110): Enhanced g-factor*. Appl. Phys. Lett. Vol. 100, 092402, (2012), DOI: [10.1063/1.3687726](https://doi.org/10.1063/1.3687726) 39
- [RC93] J. RODRÍGUEZ-CARVAJAL. *Recent advances in magnetic structure determination by neutron powder diffraction*. Physica B Vol. 192:pp. 55 (1993) 31
- [RG13] J. ROMERO GÓMEZ, R. FERREIRO GARCIA, A. DE MIGUEL CATOIRA, M. ROMERO GÓMEZ. *Magnetocaloric effect: A review of the thermodynamic cycles in magnetic refrigeration*. Renew. Sustainable Energy Rev. Vol. 17:pp. 74 (2013), DOI: [10.1016/j.rser.2012.09.027](https://doi.org/10.1016/j.rser.2012.09.027) 1
- [Rie14] M. RIEBISCH. *Hochfeld-Ferromagnetische Resonanz zur Untersuchung antiferromagnetischer Wechselwirkungen*. Master thesis (2014) 40
- [Sca15] F. SCARPA, G. TAGLIAFICO, L. A. TAGLIAFICO. *A classification methodology applied to existing room temperature magnetic refrigerators up to the year 2014*. Renew. Sust. Energy Rev. Vol. 50:pp. 497 (2015), DOI: <https://doi.org/10.1016/j.rser.2015.05.029> 2
- [Sch08] D. L. SCHLAGEL, R. W. MCCALLUM, T. A. LOGRASSO. *Influence of solidification microstructure on the magnetic properties of Ni-Mn-Sn Heusler alloys*. J. Alloys Compd. Vol. 463:pp. 38 (2008), DOI: [10.1016/j.jallcom.2007.09.049](https://doi.org/10.1016/j.jallcom.2007.09.049) 18, 19

- [Sch15] F. SCHEIBEL, T. GOTTSCHALL, K. SKOKOV, O. GUTFLEISCH, M. GHORBANI-ZAVAREH, Y. SKOURSKI, J. WOSNITZA, Ö. ÇAKIR, M. FARLE, M. ACET. *Dependence of the inverse magnetocaloric effect on the field-change rate in  $Mn_3GaC$  and its relationship to the kinetics of the phase transition*. J. Appl. Phys. Vol. 117, 233902, (2015), DOI: [10.1063/1.4922722](https://doi.org/10.1063/1.4922722) 3, 13, 21, 22, 45, 47, 48, 49, 55, 57, 59, 62, 64, 70
- [Sch17a] F. SCHEIBEL, D. SPODDIG, R. MECKENSTOCK, A. ÇAKIR, M. FARLE, M. ACET. *Shell-ferromagnetism in a Ni-Mn-In off-stoichiometric Heusler studied by ferromagnetic resonance*. AIP Advances Vol. 7, 056425, (2017), DOI: [10.1063/1.4976335](https://doi.org/10.1063/1.4976335) 91, 92, 96
- [Sch17b] F. SCHEIBEL, D. SPODDIG, R. MECKENSTOCK, T. GOTTSCHALL, A. ÇAKIR, T. KRENKE, M. FARLE, O. GUTFLEISCH, M. ACET. *Room-temperature five-tesla coercivity of a rare-earth-free shell-ferromagnet*. Appl. Phys. Lett. Vol. 110, 192406, (2017), DOI: [10.1063/1.4983199](https://doi.org/10.1063/1.4983199) 94, 95, 97, 99
- [Set16] (2016). URL <https://www.hzdr.de/db/Cms?pOid=46297&pNid=2687> 45
- [Shi02] J. H. SHIM, S. K. KWON, B. I. MIN. *Electronic structure of metallic antiperovskite compound  $GaCMn_3$* . Phys. Rev. B Vol. 66, 020406, (2002), URL <https://link.aps.org/doi/10.1103/PhysRevB.66.020406> 22
- [Sko11] Y. SKOURSKI, M. D. KUZ'MIN, K. P. SKOKOV, A. V. ANDREEV, J. WOSNITZA. *High-field magnetization of  $Ho_2Fe_{17}$* . Phys. Rev. B Vol. 83, 214420, (2011), DOI: [10.1103/PhysRevB.83.214420](https://doi.org/10.1103/PhysRevB.83.214420) 34, 35
- [Sko13] K. P. SKOKOV, K. H. MÜLLER, J. D. MOORE, J. LIU, A. Y. KARPENKOV, M. KRAUTZ, O. GUTFLEISCH. *Influence of thermal hysteresis and field cycling on the magnetocaloric effect in  $LaFe_{11.6}Si_{1.4}$* . J. Alloys Compd. Vol. 552:pp. 310 (2013), DOI: <https://doi.org/10.1016/j.jallcom.2012.10.008> 1, 12
- [Sko16] K. P. SKOKOV, Y. G. PASTUSHENKOV, S. A. NIKITIN, M. FRIES, O. GUTFLEISCH. *Rotational Magnetocaloric Effect in the  $Er_2Fe_{14}B$  Single Crystal*. IEEE Trans. Magn. Vol. 52, 5, (2016), DOI: [10.1109/tmag.2016.2530138](https://doi.org/10.1109/tmag.2016.2530138) 71
- [Skr66] G. V. SKROTSKII, L. V. KURBATOV. *Phenomenological Theory of Ferromagnetic Resonance*, book section II. Pergamon Press, Oxford (1966) 36
- [Smi55] J. SMIT, H. G. BELJERS. *Ferromagnetic Resonance Absorption in  $BaFe_{12}O_{10}$ , a Highly Anisotropic Crystal*. Philips Res. Rep. Vol. 10:pp. 113 (1955) 36
- [Smi13] A. SMITH. *Who discovered the magnetocaloric effect?* Eur. Phys. J. H Vol. 38, 4:pp. 507 (2013), DOI: [10.1140/epjh/e2013-40001-9](https://doi.org/10.1140/epjh/e2013-40001-9) 1

- 
- [Sot08] D. SOTO, F. A. HERNÁNDEZ, H. FLORES-ZÚÑIGA, X. MOYA, L. MAÑOSA, A. PLANES, S. AKSOY, M. ACET, T. KRENKE. *Phase diagram of Fe-doped Ni-Mn-Ga ferromagnetic shape-memory alloys*. Phys. Rev. B Vol. 77, 18, (2008), DOI: [10.1103/PhysRevB.77.184103](https://doi.org/10.1103/PhysRevB.77.184103) 3
- [Sto06] J. STÖHR, H. SIEGMANN. *Magnetism From Fundamentals to Nanoscale Dynamics*. Solid-State Sciences. Springer-Verlag, Berlin (2006) 7, 35
- [Sut04] Y. SUTOU, Y. IMANO, N. KOEDA, T. OMORI, R. KAINUMA, K. ISHIDA, K. OIKAWA. *Magnetic and martensitic transformations of NiMnX (X=In,Sn,Sb) ferromagnetic shape memory alloys*. Appl. Phys. Lett. Vol. 85, 19, (2004), DOI: [10.1063/1.1808879](https://doi.org/10.1063/1.1808879) 15, 16
- [Swo60] T. J. SWOBODA, W. H. CLOUD, T. A. BITHER, M. S. SADLER, H. S. JARRETT. *Evidence for an Antiferromagnetic-Ferrimagnetic Transition in Cr-Modified Mn<sub>2</sub>Sb*. Phys. Rev. Lett. Vol. 4, 10, (1960), DOI: [10.1103/PhysRevLett.4.509](https://doi.org/10.1103/PhysRevLett.4.509) 3, 26
- [Tag06] L. A. TAGLIAFICO, F. SCARPA, F. CANEPA, S. CIRAFICI. *Performance analysis of a room temperature rotary magnetic refrigerator for two different gadolinium compounds*. Int. J. Ref. Vol. 29:pp. 1307 (2006), DOI: [10.1016/j.ijrefrig.2006.07.017](https://doi.org/10.1016/j.ijrefrig.2006.07.017) 2
- [Teg02] O. TEGUS, E. BRÜCK, K. H. J. BUSCHOW, F. R. DE BOER. *Transition-metal-based magnetic refrigerants for room-temperature applications*. Nature Vol. 415:pp. 150 (2002) 1, 2
- [Tek15] A. TEKGÜL, Ö. ÇAKIR, M. ACET, M. FARLE, N. ÜNAL. *The structural, magnetic, and magnetocaloric properties of In-doped Mn<sub>2-x</sub>Cr<sub>x</sub>Sb*. J. Appl. Phys. Vol. 118, 153903, (2015), DOI: [10.1063/1.4934253](https://doi.org/10.1063/1.4934253) 26, 27
- [Tek17a] A. TEKGÜL, M. ACET, M. FARLE, N. ÜNAL. *Kinetic arrest of the ferrimagnetic state in indium-doped Mn<sub>1.82</sub>Co<sub>0.18</sub>Sb*. J. Alloys Compd. Vol. 695:pp. 418 (2017), DOI: <https://doi.org/10.1016/j.jallcom.2016.11.093> 27
- [Tek17b] A. TEKGÜL, M. ACET, F. SCHEIBEL, M. FARLE, N. ÜNAL. *The reversibility of the inverse magnetocaloric effect in Mn<sub>2-x</sub>Cr<sub>x</sub>Sb<sub>0.95</sub>Ga<sub>0.05</sub>*. Acta Mater. Vol. 124:pp. 93 (2017), DOI: [10.1016/j.actamat.2016.10.072](https://doi.org/10.1016/j.actamat.2016.10.072) 3, 27
- [Tis03] A. M. TISHIN, Y. I. SPICHKIN. *The magnetocaloric effect and its applications*. Condensed Matter Physics. Institute of Physics Publishing, Bristol and Philadelphia (2003) 5

- [Tis14] A. M. TISHIN, Y. I. SPICHKIN. *Recent progress in magnetocaloric effect: Mechanisms and potential applications*. Int. J. Ref. Vol. 37:pp. 223 (2014), DOI: <https://doi.org/10.1016/j.ijrefrig.2013.09.012> 2
- [Tit12] I. TITOV, M. ACET, M. FARLE, D. GONZÁLEZ-ALONSO, L. MAÑOSA, A. PLANES, T. KRENKE. *Hysteresis effects in the inverse magnetocaloric effect in martensitic Ni-Mn-In and Ni-Mn-Sn*. J. Appl. Phys. Vol. 112, 073914, (2012), DOI: [10.1063/1.4757425](https://doi.org/10.1063/1.4757425) 1, 3, 12, 18, 41
- [Toh03] T. TOHEI, H. WADA, T. KANOMATA. *Negative magnetocaloric effect at the antiferromagnetic to ferromagnetic transition of  $Mn_3GaC$* . J. Appl. Phys. Vol. 94, 3, (2003), DOI: [10.1063/1.1587265](https://doi.org/10.1063/1.1587265) 21, 22, 47, 49, 51, 53, 59, 65, 70, 71, 78, 80, 101, 104
- [Toh04] T. TOHEI, H. WADA, T. KANOMATA. *Large magnetocaloric effect of  $Mn_{3-x}Co_xGaC$* . J. Magn. Magn. Mater. Vol. 272-276:pp. E585 (2004), DOI: [10.1016/j.jmmm.2003.12.1035](https://doi.org/10.1016/j.jmmm.2003.12.1035) 22
- [Tun82] C. J. TUNG, I. SAID, G. E. EVERETT. *Magnetic anisotropy constants of Fe and Ni at 77, 4.2, and 1.09 K: Interdomain configuration transitions in Ni*. J. Appl. Phys. Vol. 53:pp. 2044 (1982), DOI: [10.1063/1.330737](https://doi.org/10.1063/1.330737) 78
- [Von66] S. VONSOVSKII. *Ferromagnetic Resonance*. Pergamon Press, Oxford (1966) 35
- [Wac83] E. WACHTEL, F. HENNINGER, B. PRAEDEL. *Constitution and Magnetic Properties of Ni-Mn-Sn Alloys - Solid and Liquid State*. J. Magn. Magn. Mater. Vol. 38:pp. 305 (1983) 33
- [Wan09] B. S. WANG, P. TONG, Y. P. SUN, X. LUO, X. B. ZHU, G. LI, X. D. ZHU, S. B. ZHANG, Z. R. YANG, W. H. SONG, J. M. DAI. *Large magnetic entropy change near room temperature in antiperovskite  $SnCMn_3$* . EPL Vol. 85, 47004, (2009), DOI: [10.1209/0295-5075/85/47004](https://doi.org/10.1209/0295-5075/85/47004) 23
- [Wan10] B. S. WANG, P. TONG, Y. P. SUN, W. TANG, L. J. LI, X. B. ZHU, Z. R. YANG, W. H. SONG. *Structural, magnetic properties and magnetocaloric effect in Ni-doped antiperovskite compounds  $GaCMn_{3-x}Ni_x$  ( $0 \leq x \leq 0.10$ )*. Physica B: Condensed Matter Vol. 405:pp. 2427 (2010), DOI: [10.1016/j.physb.2010.03.001](https://doi.org/10.1016/j.physb.2010.03.001) 22
- [Wan11] B. S. WANG, C. C. LI, S. LIN, J. C. LIN, L. J. LI, P. TONG, W. J. LU, X. B. ZHU, Z. R. YANG, W. H. SONG, J. M. DAI, Y. P. SUN. *Magnetic properties and room-temperature magnetocaloric effect in the doped antiperovskite compounds  $Ga_{1-x}Al_xCMn_3$  ( $0 \leq x \leq 0.15$ )*. J. Magn. Magn. Mater. Vol. 323:pp. 2017 (2011), DOI: [10.1016/j.jmmm.2011.02.046](https://doi.org/10.1016/j.jmmm.2011.02.046) 23

- 
- [War81] E. WARBURG. *Magnetische Untersuchungen*. Ann. Phys. Vol. 249:pp. 141 (1881), DOI: [10.1002/andp.18812490510](https://doi.org/10.1002/andp.18812490510) 1
- [Was15] A. WASKE, L. GIEBELER, B. WEISE, A. FUNK, M. HINTERSTEIN, M. HERKLOTZ, K. SKOKOV, S. FÄHLER, O. GUTFLEISCH, J. ECKERT. *Asymmetric first-order transition and interlocked particle state in magnetocaloric La(Fe,Si)<sub>13</sub>*. Phys. Status Solidi (RRL) Vol. 9:pp. 136 (2015), DOI: [10.1002/pssr.201409484](https://doi.org/10.1002/pssr.201409484) 51
- [Web67] P. J. WEBSTER, R. S. TEBBLE. *The magnetic and chemical ordering of the heusler alloys Pd<sub>2</sub>MnIn, Pd<sub>2</sub>MnSn and Pd<sub>2</sub>MnSb*. Philos. Mag. Vol. 16:pp. 347 (1967), DOI: [10.1080/14786436708229747](https://doi.org/10.1080/14786436708229747) 16
- [Web69] P. J. WEBSTER. *Heusler alloys*. Contemporary Physics Vol. 10, 6,:pp. 559 (1969), DOI: [10.1080/00107516908204800](https://doi.org/10.1080/00107516908204800) 15, 16
- [Wei17] A. WEISS, P. PICCARD. J. Phys. (Paris) Vol. 5, 103, (1917) 1
- [Wil57] M. K. WILKINSON, N. S. GINGRICH, C. G. SHULL. *The Magnetic Structure of Mn<sub>2</sub>Sb*. J. Phys. Chem. Solids. Vol. 2:pp. 289 (1957) 25, 26
- [Wol16] M. WOLLOCH, M. E. GRUNER, W. KEUNE, P. MOHN, J. REDINGER, F. HOFER, D. SUESS, R. PODLOUCKY, J. LANDERS, S. SALAMON, F. SCHEIBEL, D. SPODDIG, R. WITTE, B. ROLDAN CUENYA, O. GUTFLEISCH, M. Y. HU, J. ZHAO, T. TOELLNER, E. E. ALP, M. SIEWERT, P. ENTEL, R. PENTCHEVA, H. WENDE. *Impact of lattice dynamics on the phase stability of metamagnetic FeRh: Bulk and thin films*. Phys. Rev. B Vol. 94, 174435, (2016), DOI: [10.1103/PhysRevB.94.174435](https://doi.org/10.1103/PhysRevB.94.174435) 10
- [Wos07] J. WOSNITZA, A. D. BIANCHI, J. FREUDENBERGER, J. HAASE, T. HERMANNSDÖRFER, N. KOZLOVA, L. SCHULTZ, Y. SKOURSKI, S. ZHERLITSYN, S. A. ZVYAGIN. *Dresden pulsed magnetic field facility*. J. Magn. Magn. Mater. Vol. 310:pp. 2728 (2007), DOI: [10.1016/j.jmmm.2006.10.1115](https://doi.org/10.1016/j.jmmm.2006.10.1115) 34
- [WWW13] (2013). URL <http://www.metco.npl.co.uk/?p=43> 2
- [Xu16] X. XU, Y. YOSHIDA, T. OMORI, T. KANOMATA, R. KAINUMA. *Magnetic Properties and Phase Diagram of Ni<sub>50</sub>Mn<sub>50-x</sub>Ga<sub>x/2</sub>In<sub>x/2</sub> Magnetic Shape Memory Alloys*. Shap. Mem. Superelasticity Vol. 2:pp. 371 (2016), DOI: [10.1007/s40830-016-0084-x](https://doi.org/10.1007/s40830-016-0084-x) 15
- [You16] (2016). URL <https://www.youtube.com/watch?v=9LKzcODcQzc> 19, 91
- [Yu10] B. YU, M. LIU, P. W. EGOLF, A. KITANOVSKI. *A review of magnetic refrigerator and heat pump prototypes built before the year 2010*. Int. J. Refrig. Vol. 33:pp. 1029 (2010), DOI: [10.1016/j.ijrefrig.2010.04.002](https://doi.org/10.1016/j.ijrefrig.2010.04.002) 2, 47, 66

- [Yuh09] W. M. YUHASZ, D. L. SCHLAGEL, Q. XING, K. W. DENNIS, R. W. MCCALLUM, T. A. LOGRASSO. *Influence of annealing and phase decomposition on the magnetostructural transitions in  $Ni_{50}Mn_{39}Sn_{11}$* . J. Appl. Phys. Vol. 105, 07A921, (2009), DOI: [10.1063/1.3067855](https://doi.org/10.1063/1.3067855) 19
- [Yuh10] W. M. YUHASZ, D. L. SCHLAGEL, Q. XING, R. W. MCCALLUM, T. A. LOGRASSO. *Metastability of ferromagnetic Ni-Mn-Sn Heusler alloys*. J. Alloys Compd. Vol. 492:pp. 681 (2010), DOI: [10.1016/j.jallcom.2009.12.016](https://doi.org/10.1016/j.jallcom.2009.12.016) 19
- [Zha12] H. ZHANG, B. G. SHEN, Z. Y. XU, X. Q. ZHENG, J. SHEN, F. X. HU, J. R. SUN, Y. LONG. *Reduction of hysteresis loss and large magnetocaloric effect in the C- and H-doped  $La(Fe, Si)_{13}$  compounds around room temperature*. J. Appl. Phys. Vol. 111, 07A909, (2012), DOI: [10.1063/1.3670608](https://doi.org/10.1063/1.3670608) 2
- [Zhe06] S. ZHERLITSYN, A. D. BIANCHI, T. HERRMANNSDOERFER, F. POBELL, Y. SKOURSKI, A. SYTCHEVA, S. ZVYAGIN, J. WOSNITZA. *Coil Design for Non-Destructive Pulsed-Field Magnets Targeting 100 T*. IEEE Transactions on Applied Superconductivity Vol. 16, 2, (2006), DOI: [10.1109/tasc.2005.864297](https://doi.org/10.1109/tasc.2005.864297) 34
- [Zie75] K. R. A. ZIEBECK, P. J. WEBSTER. *Helical magnetic order in  $Ni_2MnAl$* . J. Phys. F. Metal Phys. Vol. 5:pp. 1756 (1975) 33
- [Zin16] B. W. ZINGSEM. *A Theory of the Magnetodynamic Response Function*. Master thesis (2016) 36, 40, 76
- [Zin17] B. W. ZINGSEM, M. WINKLHOFFER, R. MECKENSTOCK, M. FARLE. *Unified description of collective magnetic excitations*. Phys. Rev. B Vol. 96, 224407, (2017), URL <https://link.aps.org/doi/10.1103/PhysRevB.96.224407> 40, 76
- Number of citations:.....181

# Acknowledgment

At this place I would like to thank the following people who significantly contributed to the outcome of this work.

First of all, I would like to thank Prof. Dr. Michael Farle, who has given me the opportunity to do my doctoral dissertation in his research group, and to give thanks for beneficial discussions.

Specially I want to thank Prof. Dr. Mehmet Acet for the great support during my thesis and for the opportunity to research in this very interesting topic. I appreciate his broad expertise and the constructive discussions, feedback and review at each time.

In particular I would also thank Dr. Ralf Meckenstock for his patience and readiness for discussing and sharing his expertise on magnetic resonances. His enthusiasm for this topic really motivates me for my own studies.

Furthermore, I want to thank Dr. Tino Gottschall, Dr. Maximilian Fies, Dr. Konstantin Skokov and Prof. Dr. Oliver Gutfleisch from Technical University of Darmstadt for the productive discussion and successful cooperation.

I would like to thank Dr. Öznur Çakır for the nice cooperation and fruitful discussions about antiperovskite materials.

Furthermore I would like to thank Dr. Atakan Tekül for the successful cooperation and fruitful discussions about MnSb-based materials. It was a pleasure to work with you in the laboratory.

I would like to thank Dr. Yuri Skourski, Dr. Mahdiyeh Ghorbani Zavareh, Dr. Catalina Salazar Mejia and Prof. Dr. Jochen Wosnitza from Helmholtz-Zentrum Dresden-Rossendorf for the opportunity and the support during the pulsed-field measurements.

Furthermore I would like to thank Dr. Francesco Cugini and Prof. Dr. Massimo Solzi from Parma University for our joint  $\Delta T_{\text{ad}}$  measurements and fruitful discussions.

I would also like to thank Dr. Markus E. Gruner, Dr. Anna Grünebohm and Prof. Dr. Michael Winklhofer for their helpful discussions.

My thanks go also to Dr. Thorsten Krenke and Dr. Asli Çakır for the nice cooperation and their expertise about Heusler alloys and the helpful discussions.

In particular I want to thank Dr. Detlef Spoddig and Horst Zähres for the support and the suggestions specially in technical aspects.

I would like to thank Benjamin Zingsem FMR simulations and Thomas Feggeler for micro-magnetic simulation.

## *Acknowledgment*

---

Also I would like to thank all current and former members of the work group Farle, who are not listed namely, for the nice working atmosphere. It was a pleasure to work together with all of you.

I thank the Deutsche Forschungsgemeinschaft priority program SPP 1599 - Ferroic cooling for the funding of my thesis. Additionally, I thank all project members for fruitful discussions and successful and nice cooperation.

Last but not least, I particularly thank my family and all friends who motivated and supported me during the entire time.



# List of Figures

1.1	Schematic of a magnetocaloric cooling cycle. . . . .	2
1.2	Origin of hysteresis . . . . .	4
2.1	Schematic of the MCE at the second-order transition . . . . .	7
2.2	Schematic of the conventional MCE at the first-order transition . . . .	8
2.3	Schematic of the inverse MCE at first-order transition . . . . .	9
2.4	Overview of $ \Delta T_{\text{ad}} $ of different magnetocaloric materials . . . . .	10
2.5	Schematic of the temperature-dependent Gibbs free energy and magnetization at first-order transition . . . . .	12
2.6	Schematic of the effect of hysteresis on the inverse MCE at first-order transition . . . . .	13
2.7	$L2_1$ and $B2$ structure of $\text{Ni}_2\text{Mn}_1\text{X}_1$ full Heusler alloy . . . . .	16
2.8	Magnetic and structural phase diagram of Ni-Mn-based Heusler alloys	17
2.9	Crystallographic and magnetic structure of $\text{Mn}_3\text{GaC}$ . . . . .	21
2.10	Crystallographic and magnetic structure of $\text{Mn}_2\text{Sb}$ and $\text{Mn}_{2-y}\text{X}_y\text{Sb}$ . .	25
3.1	Formation of $\text{Mn}_3\text{GaC}$ single crystals . . . . .	30
3.2	Indexing of EBSD diffraction patterns and calculation of the crystal orientation . . . . .	32
3.3	Pulsed-field magnetometer at HLD-EMFL . . . . .	35
3.4	Schematic of FMR in a microwave cavity . . . . .	38
3.5	Schematic of FMR setup implemented in a temperature controlled cryostat which contains a superconducting magnet (12 T) . . . . .	39
3.6	Schematic drawing of the adiabatic magneto-calorimeter for $\Delta T_{\text{ad}}$ measurements with slow field-sweep rate $11 \text{ mTs}^{-1}$ . . . . .	42
3.7	Determination of $\Delta T_{\text{ad}}$ . . . . .	43
3.8	Schematic of the sample holder of the $\Delta T_{\text{ad}}$ -measurement setup with medium field-sweep rate ( $700 \text{ mTs}^{-1}$ ) . . . . .	43
3.9	Schematic of the measurements probe of the $\Delta T_{\text{ad}}$ -measurement setup with fast field-sweep rate ( $20 \text{ Ts}^{-1}$ ) . . . . .	44
3.10	Profile of pulsed magnetic fields and corresponding field-sweep rates for $\Delta T_{\text{ad}}$ with rates up to $1.5 \text{ kTs}^{-1}$ . . . . .	45
3.11	Schematic of the sample holder of the $\Delta T_{\text{ad}}$ measurements with very fast field-sweep rate (up to $1.5 \text{ kTs}^{-1}$ ) . . . . .	46

4.1	Temperature-dependent magnetization of $\text{Mn}_3\text{GaC}$ powder in 5 mT and 5 T . . . . .	48
4.2	Field-dependent magnetization of $\text{Mn}_3\text{GaC}$ compact sample at 145 K, 150 K and 160 K measured in increasing and decreasing field . . . . .	49
4.3	Field-dependent magnetization of $\text{Mn}_3\text{GaC}$ powder in the range $137 \leq T \leq 164$ K and $\Delta S_T$ of powder and compact samples . . . . .	50
4.4	Time $M(T)$ and field-dependent magnetization $M(B)$ of compact sample $\text{Mn}_3\text{GaC}$ 1 in pulsed magnetic field of 10 T . . . . .	52
4.5	Critical field values $B_{S/Fj}^{i/a}$ ( $j = 1, 2$ ) of the first-order transition of compact $\text{Mn}_3\text{GaC}$ 1 for isothermal and adiabatic $M(B)$ -curves as a function of temperature . . . . .	54
4.6	Direct $\Delta T_{ad}$ measurements of compact $\text{Mn}_3\text{GaC}$ 1 performed in 5 T magnetic field with field-sweep rate of $11 \text{ mTs}^{-1}$ . . . . .	55
4.7	Direct $\Delta T_{ad}$ measurements of compact $\text{Mn}_3\text{GaC}$ 1 performed in 2 T magnetic field with a field-sweep rate of $700 \text{ mTs}^{-1}$ . . . . .	57
4.8	Direct $\Delta T_{ad}$ measurements of compact $\text{Mn}_3\text{GaC}$ 2 performed in 2 T magnetic field with a field-sweep rate of $20 \text{ Ts}^{-1}$ . . . . .	60
4.9	Direct $\Delta T_{ad}$ measurements of $\text{Mn}_3\text{GaC}$ 1 performed in 10 T pulsed magnetic fields with field-sweep rate of about $1 \text{ kTs}^{-1}$ . . . . .	62
4.10	Entropy change $\Delta S_T$ of $\text{Mn}_3\text{GaC}$ for 2 T and 5 T field change and $\Delta T_{ad}$ for different field-sweep rates as a function of target temperature . . . . .	64
4.11	SEM image and EDX mapping of the $\text{Mn}_3\text{GaC}$ crystal . . . . .	67
4.12	EBSD of $\text{Mn}_3\text{GaC}$ crystal, phase identification and crystal orientation directions analysis . . . . .	68
4.13	Temperature-dependent magnetization of $\text{Mn}_3\text{GaC}$ single crystal for an applied field of 50 mT and 2 T . . . . .	71
4.14	FMR quartz-tube sample-holder with $\text{Mn}_3\text{GaC}$ single crystal . . . . .	72
4.15	Field-dependent FMR absorption derivative spectra of $\text{Mn}_3\text{GaC}$ single crystal in the temperature range $150 \leq T \leq 270$ K . . . . .	73
4.16	Angular-dependent FMR spectra of $\text{Mn}_3\text{GaC}$ crystal . . . . .	75
4.17	Simulated field and angular-dependent FMR spectra of $\text{Mn}_3\text{GaC}$ crystal . . . . .	77
4.18	Temperature-dependent magnetization of $\text{Mn}_{1.82}\text{Cr}_{0.07}\text{Co}_{0.04}\text{Sb}_{1.07}$ for an applied field of 50 mT and 2 T . . . . .	80
4.19	Field-dependent magnetization $M(B)$ and entropy change $\Delta S$ of $\text{Mn}_{1.82}\text{Cr}_{0.07}\text{Co}_{0.04}\text{Sb}_{1.07}$ in the temperature range $275 \leq T \leq 315$ K . . . . .	81
4.20	Direct $\Delta T_{ad}$ measurements of $\text{Mn}_{1.82}\text{Cr}_{0.07}\text{Co}_{0.04}\text{Sb}_{1.07}$ at 287 K done in a oscillated magnetic field of 5 T with a field-sweep rate of $11 \text{ mTs}^{-1}$ . . . . .	82
4.21	Field dependence of $\Delta T_{ad}$ of $\text{Mn}_{1.82}\text{Cr}_{0.07}\text{Co}_{0.04}\text{Sb}_{1.07}$ for different temperatures . . . . .	83

---

4.22 $\Delta T_{\text{ad}}$ measurements of $\text{Mn}_{1.82}\text{Cr}_{0.07}\text{Co}_{0.04}\text{Sb}_{1.07}$ in pulsed magnetic field with a field-sweep rate up to $1 \text{ kTs}^{-1}$ . . . . .	85
4.23 Direct $\Delta T_{\text{ad}}$ measurements at 290 K in pulsed magnetic field with different maximum field values. . . . .	87
4.24 Comparison of $\Delta T_{\text{ad}}$ measurements with field-sweep rates of $11 \text{ mTs}^{-1}$ and $1 \text{ kTs}^{-1}$ . . . . .	89
4.25 Field-dependent magnetization of $\text{Ni}_{49.6}\text{Mn}_{45.5}\text{In}_{4.9}$ at 300 K for the initial state and decomposed state . . . . .	92
4.26 Field-dependent magnetization and derivative of the magnetization $dM(B)/dB$ of decomposed $\text{Ni}_{49.6}\text{Mn}_{45.5}\text{In}_{4.9}$ at 300 K in the field-range $-14 \leq B \leq 14 \text{ T}$ . . . . .	94
4.27 Field-dependent magnetization of the FM precipitates in decomposed $\text{Ni}_{49.6}\text{Mn}_{45.5}\text{In}_{4.9}$ at 300 K, the AF matrix is subtracted . . . . .	95
4.28 Bidirectional field-dependent FMR absorption derivative of decomposed $\text{Ni}_{49.6}\text{Mn}_{45.5}\text{In}_{4.9}$ at 300 K in the field range $-11.5 \leq B \leq 11.5 \text{ T}$ . . .	97
4.29 Bidirectional field-dependent FMR absorption derivative of decomposed $\text{Ni}_{49.6}\text{Mn}_{45.5}\text{In}_{4.9}$ at 300 K in the field range $-2 \leq B \leq 2 \text{ T}$ . . . . .	99

## List of Publications

12. M. Fries, T. Gottschall, **F. Scheibel**, L. Pfeuffer, K. P. Skokov, Y. Skourski, M. Acet, M. Farle, J. Wosnitzer, and O. Gutfleisch,  
*Dynamics of the magnetoelastic phase transition and adiabatic temperature change in  $Mn_{1.3}Fe_{0.7}P_{0.5}Si_{0.55}$* , submitted (2018)
11. **F. Scheibel**, B. Zingsem, T. Feggeler, R. Meckenstock, D. Spoddig, M. Farle, and M. Acet  
*Magnetic anisotropy of single crystal antiperovskite  $Mn_3GaC$  studied by ferromagnetic resonance and dynamic magnetic-response simulations*, in preparation
10. L. Dincklage, **F. Scheibel**, A. Çakır, M. Farle, and M. Acet,  
*Annealing-time and annealing-temperature dependencies of the size of Ni-Mn-In shell-ferromagnetic nano-precipitates by Scherrer analysis*, AIP Adv. **8**, 025012 (2018), DOI:10.1016/j.jmmm.2008.11.043
9. **F. Scheibel**, D. Spoddig, R. Meckenstock, T. Gottschall, A. Çakır, T. Krenke, M. Farle, O. Gutfleisch, and M. Acet,  
*Room-temperature five-tesla coercivity of a rare-earth-free shell-ferromagnet*, Appl. Phys. Lett. **110**, 192406 (2017), DOI: 10.1063/1.4983199
8. **F. Scheibel**, D. Spoddig, R. Meckenstock, A. Çakır, M. Farle, and M. Acet,  
*Shell-ferromagnetism in a Ni-Mn-In off-stoichiometric Heusler studied by ferromagnetic resonance*, AIP Adv. **7**, 056425 (2017), DOI: 10.1063/1.4976335
7. A. Tekgül, M. Acet, **F. Scheibel**, M. Farle, and N. Ünal,  
*The reversibility of the inverse magnetocaloric effect in  $Mn_{2-x}Cr_xSb_{0.95}Ga_{0.05}$* , Acta Mater. **124**, 93 (2017), DOI: 10.1016/j.actamat.2016.10.072

6. T. Krenke, A. Çakır, **F. Scheibel**, M. Acet, and M. Farle,  
*Magnetic proximity effect and shell-ferromagnetism in metastable  $Ni_{50}Mn_{45}Ga_5$* ,  
J. Appl. Phys. **120**, 243904 (2016), DOI: [10.1063/1.4972480](https://doi.org/10.1063/1.4972480)
  
5. M. Wolloch, M. E. Gruner, W. Keune, P. Mohn, J. Redinger, F. Hofer, D. Suess,  
R. Podloucky, J. Landers, S. Salamon, **F. Scheibel**, D. Spoddig, R. Witte, B.  
Roldan Cuenya, O. Gutfleisch, M. Y. Hu, J. Zhao, T. Toellner, E. E. Alp, M.  
Siewert, P. Entel, R. Pentcheva, and H. Wende,  
*Impact of lattice dynamics on the phase stability of metamagnetic FeRh: Bulk and  
thin films*, Phys. Rev. B **94**, 174435 (2016), DOI: [10.1103/PhysRevB.94.174435](https://doi.org/10.1103/PhysRevB.94.174435)
  
4. T. Gottschall, K. P. Skokov, **F. Scheibel**, M. Acet, M. Ghorbani Zavareh,  
Y. Skourski, J. Wosnitza, M. Farle, and O. Gutfleisch,  
*Dynamical Effects of the Martensitic Transition in Magnetocaloric Heusler Alloys  
from Direct  $\Delta T_{ad}$  Measurements under Different Magnetic-Field-Sweep Rates*,  
Phys. Rev. Applied **5**, 0240013 (2016), DOI: [10.1103/PhysRevApplied.5.024013](https://doi.org/10.1103/PhysRevApplied.5.024013)
  
3. **F. Scheibel**, T. Gottschall, K. Skokov, O. Gutfleisch, M. Ghorbani-Zavareh,  
Y. Skourski, J. Wosnitza, Ö. Çakır, M. Farle, and M. Acet,  
*Dependence of the inverse magnetocaloric effect on the field-change rate in  
 $Mn_3GaC$  and its relationship to the kinetics of the phase transition*, J. Appl.  
Phys. **117**, 233902 (2015), DOI: [10.1063/1.4922722](https://doi.org/10.1063/1.4922722)
  
2. S. Singh, P. Kushwaha, **F. Scheibel**, H. Liermann, S. R. Barman, M. Acet,  
C. Felser, and D. Pandey,  
*Residual stress induced stabilization of martensite phase and its effect on the  
magnetostructural transition in Mn-rich Ni-Mn-In/Ga magnetic shape-memory  
alloys*, Phys. Rev. B **92**, 020105(R) (2015), DOI: [10.1103/PhysRevB.92.020105](https://doi.org/10.1103/PhysRevB.92.020105)
  
1. **F. Scheibel**, F. Haering, P. Ziemann, and U. Wiedwald,  
*Role of developing  $L1_0$  chemical order on the (001)-texture formation of  
( $Fe_{1-x}Cu_x$ )Pt films grown on amorphous substrates*, J. Phys. D: Appl. Phys.  
**48**, 085001 (2015), DOI: [10.1088/0022-3727/48/8/085001](https://doi.org/10.1088/0022-3727/48/8/085001)

# Conference Contributions

## Participation at national conferences

1. F. Scheibel, Ö. Çakır, A. Tekgül, M. Acet and M. Farle, *Conventional and inverse magnetocaloric effects at magnetostructural transitions in Mn-based compounds*, DPG Spring Meeting Dresden Germany 2014 (Poster)
2. F. Scheibel, Ö. Çakır, I. Titov, M. Acet and M. Farle, *Conventional and Inverse magnetocaloric effects in systems with narrow thermal hysteresis*, Edgar-Lüscher-Seminar Klosters Swiss 2014 (Poster)
3. F. Scheibel, T. Gottschall, M. Ghorbani Zavareh, M. Riebisch, Ö. Çakır, M. Farle and M. Acet, *Thermodynamics and magnetism at the first-order magnetostructural transition in  $Mn_3GaC$  powder and single crystal samples*, DPG Spring Meeting Berlin Germany 2015 (Poster)
4. F. Scheibel, T. Gottschall, M. Farle and M. Acet, *Reversible processes in minor loop hysteresis at the first-order magnetostructural transition in  $NiMnX$  ( $X=In, Sn$ )*, DPG Spring Meeting Berlin Germany 2015 (Oral talk)
5. F. Scheibel, *Response of the magneto-caloric effect (MCE) to different magnetic field-change rates*, Edgar-Lüscher-Seminar Klosters Swiss 2015 (Invited talk)
6. F. Scheibel, D. Spoddig, R. Meckenstock, M. E. Gruner, B. Zingsem, M. Farle and M. Acet, *Structure and magnetism of single crystal  $Mn_3GaC$* , DPG Spring Meeting Regensburg Germany 2016 (Oral talk)
7. F. Scheibel, T. Gottschall, O. Gutfleisch, Ö. Çakır, A. Tekgül, Y. Skurski, M. Farle and M. Acet, *Basic mechanism and mastering of hysteresis at first-order magnetostructural transition*, Edgar-Lüscher-Seminar Klosters Swiss 2016 (Poster)
8. F. Scheibel, Ö. Çakır, T. Gottschall, M. Ghorbani Zavareh, C. Salazar Mejia, Y. Skourski, F. Cugini, A. Tekgül, O. Gutfleisch, J. Wosnitza, M. Solzi, M. Farle and M. Acet, *Towards an understanding of the basic mechanism of hysteresis at a first-order magneto-structural transition*, DPG Spring Meeting Dresden 2017 (Poster)

9. F. Scheibel, D. Spoddig, R. Meckenstock, A. Çakır, M. Farle and M. Acet, *Shell-ferromagnetism of nano-precipitate in a Ni-Mn-In offstoichiometric Heusler alloy by ferromagnetic resonance*, DPG Spring Meeting Dresden 2017 (Oral talk)

## Participation at international conferences

1. F. Scheibel, F. Häring, P. Ziemann, U. Wiedwald, *Growth of (001)-textured  $L1_0$  FePtCu thin films on  $SiO_2$  by pulsed laser deposition and rapid thermal annealing*, MiFuN Duisburg Germany 2014 (Poster)
2. F. Scheibel, Ö. Çakır, T. Gottschall, M. Ghorbani Zavareh, M. Riebisch, B. Zingsem, M. Farle and M. Acet, *Thermodynamics and magnetism at the first-order magnetostructural transition in  $Mn_3GaC$  powder and single crystal samples*, GRC Nanomaterials for Applications in Energy Technology Ventura United States 2015 (Poster)
3. F. Scheibel, T. Gottschall, O. Gutfleisch, Ö. Çakır, A. Tekgül, Y. Skurski, M. Farle and M. Acet, *Basic mechanism and mastering of hysteresis at first-order magnetostructural transitions*, DDMC Delft Netherlands 2015 (Poster)
4. F. Scheibel, T. Gottschall, M. Ghorbani Zavareh, Y. Skurski, Ö. Çakır, F. Cugini, R. Meckenstock, O. Gutfleisch, J. Wosnitza, M. Solzi, M. Farle and M. Acet, *Thermodynamics and magnetism at the first-order magnetostructural transition in  $Mn_3GaC$  powder and single crystal samples*, MMM New Orleans United States 2016 (Poster)
5. F. Scheibel, D. Spoddig, R. Meckenstock, A. Çakır, M. Farle and M. Acet, *Shell-ferromagnetism in a Ni-Mn-based Off-stoichiometric Heusler Studied by Ferromagnetic Resonance*, MMM New Orleans United States 2016 (Oral talk)
6. F. Scheibel, T. Gottschall, M. Ghorbani Zavareh, C. Salazar Mejia, Y. Skurski, Ö. Çakır, F. Cugini, A. Tekgül, O. Gutfleisch, J. Wosnitza, M. Solzi, M. Farle and M. Acet, *Basic mechanism and mastering of hysteresis at first-order magnetostructural transitions*, International Workshop on Hysteresis in Magnetocaloric, Electrocaloric and Elastocaloric Refrigeration Dresden Germany 2017 (Poster)

## Further participations

1. FullProf School, Institute Laue-Langevin Grenoble France 2015

## **Curriculum Vitae**

The curriculum vitae is not included in the online version, for reasons of data protection.





# Declaration of Authenticity

I hereby declare that this thesis is the result of my own work, and is prepared by the specified sources and resources. The corresponding sources are cited.

Duisburg, the February 15, 2018

---

(Franziska Scheibel)

## Erklärung

Ich beantrage die Zulassung zur Promotionsprüfung zur Erlangung des Titels “Dr. rer. nat.”. Beigefügt sind fünf gebundene Ausfertigungen meiner Dissertation “Influence of hysteresis at magnetostructural transitions on the magnetocaloric properties of Heuslers, Antiperovskites, and Pnictides” inklusive der Veröffentlichungen, die im Zusammenhang mit der Dissertation entstanden sind. Hiermit erkläre ich, dass ich vorliegende Dissertation ohne Hilfe Dritter und nur mit den angegebenen Quellen und Hilfsmitteln verfasst habe. Die aus Quellen entnommenen Stellen sind als solche gekennzeichnet. Ich versichere, dass ich die Dissertation nur in diesem Promotionsverfahren eingereicht habe.

Duisburg, den 15.02.2018

---

(Franziska Scheibel)

## List of Relevant Publications

**F. Scheibel**, D. Spoddig, R. Meckenstock, T. Gottschall, A. Çakır, T. Krenke, M. Farle, O. Gutfleisch, and M. Acet,  
*Room-temperature five-tesla coercivity of a rare-earth-free shell-ferromagnet*, Appl. Phys. Lett. **110**, 192406 (2017), DOI: [10.1063/1.4983199](https://doi.org/10.1063/1.4983199)

**F. Scheibel**, D. Spoddig, R. Meckenstock, A. Çakır, M. Farle, and M. Acet,  
*Shell-ferromagnetism in a Ni-Mn-In off-stoichiometric Heusler studied by ferromagnetic resonance*, AIP Advances **7**, 056425 (2017), DOI: [10.1063/1.4976335](https://doi.org/10.1063/1.4976335)

T. Krenke, A. Çakır, **F. Scheibel**, M. Acet, and M. Farle,  
*Magnetic proximity effect and shell-ferromagnetism in metastable  $Ni_{50}Mn_{45}Ga_5$* , J. Appl. Phys. **120**, 243904 (2016), DOI: [10.1063/1.4972480](https://doi.org/10.1063/1.4972480)

T. Gottschall, K. P. Skokov, **F. Scheibel**, M. Acet, M. Ghorbani Zavareh, Y. Skourski, J. Wosnitza, M. Farle, and O. Gutfleisch,  
*Dynamical Effects of the Martensitic Transition in Magnetocaloric Heusler Alloys from Direct  $\Delta T_{ad}$  Measurements under Different Magnetic-Field-Sweep Rates*, Phys. Rev. Applied **5**, 0240013 (2016), DOI: [10.1103/PhysRevApplied.5.024013](https://doi.org/10.1103/PhysRevApplied.5.024013)

**F. Scheibel**, T. Gottschall, K. Skokov, O. Gutfleisch, M. Ghorbani-Zavareh, Y. Skourski, J. Wosnitza, Ö. Çakır, M. Farle, and M. Acet,  
*Dependence of the inverse magnetocaloric effect on the field-change rate in  $Mn_3GaC$  and its relationship to the kinetics of the phase transition*, J. Appl. Phys. **117**, 233902 (2015), DOI: [10.1063/1.4922722](https://doi.org/10.1063/1.4922722)

